Nonlinear Ion Concentration Polarization: Fundamentals and Applications

ARCHIVES
MASSACHUSETTS INSTITUTE OF TECHNOLOGY
NOV 12 2013
LIBRARIES

by
Rhokyun Kwak

M.S. Mechanical and Aerospace Engineering, 2009
B.S. Mechanical and Aerospace Engineering, 2007
Seoul National University, Republic of Korea

SUBMITTED TO THE DEPARTMENT OF MECHANICAL ENGINEERING IN PARTIAL FULFILLMENT OF THE REQUIREMENTS FOR THE DEGREE OF

DOCTOR OF PHILOSOPHY IN MECHANICAL ENGINEERING
AT THE
MASSACHUSETTS INSTITUTE OF TECHNOLOGY

SEPTEMBER 2013

©2013 Massachusetts Institute of Technology. All rights reserved.

Signature of Author: _____
Department of Mechanical Engineering
July 27, 2013

Certified by: _____
Jongyoon Han
Professor of Electrical Engineering and Computer Science
Professor of Biological Engineering
Thesis Supervisor

Certified by: _____
John H. Lienhard V
Professor of Mechanical Engineering
Committee Chair

Accepted by: _____
David E. Hardt
Chairman, Department Committee on Graduate Students

Nonlinear Ion Concentration Polarization: Fundamentals and Applications

by

Rhokyun Kwak

Submitted to the Department of Mechanical Engineering
on July 27, 2013 in Partial Fulfillment of the Requirements
for the Degree of Doctor of Philosophy in Mechanical Engineering

Abstract

Ion exchange membrane (IEM) is a functional material that has a permselectivity of ions. Two types of IEMs - anion exchange membrane (AEM) and cation exchange membrane (CEM) – are used in a variety of electrochemical systems. Ion concentration polarization (ICP) is an ion transport phenomenon that occurs when ions selectively pass through IEMs. Recently, ICP has drawn renewed attention from physicists and engineers, due to its importance in understanding various electrochemical processes for biosensing, desalination, and energy devices. One of the significant scientific issues in ICP is the source of overlimiting conductance (OLC); even after the diffusion-limited current is achieved and nearly all ions are rejected from the IEM (reaching the so-called 'limiting current'), the current starts to increase again at a sufficiently high bias voltage. This nonlinearity of ICP has been extensively studied, but the complexity of this multiscale, multiphysic phenomenon makes it challenging to a fully-detailed picture. My Ph.D thesis is focused at the fundamental understanding and new engineering applications of nonlinear ICP. In this thesis, we consider four subjects: **i)** visualization of nonlinear ICP and its effects in electrodialysis (ED), **ii)** electroconvection (EC) as a source of OLC and its behaviors under shear flow, **iii)** study of water desalination process by ICP and its performance compared with ED, and **iv)** development of high-throughput, continuous-flow bio-agent preconcentrator by ICP. First, we describe the microscale ED model system for studying nonlinear ICP, which is used for visualizing *in situ* fluid flows and concentration profiles near IEMs. We verify that the nonlinear ICP largely determines ion transport in ED system. Interesting trends and insights are revealed, which will help in clarifying scientific issues regarding ED operation and improving the efficiency. Second, with this ability to visualize ICP, we firmly establish EC as the mechanism for OLC in the realistic ED system; EC exists near the both IEMs of standard ED systems, and it enhances ion flux through the membranes. We also characterize EC under shear flow by both experiments and numerical modeling. To the best of our knowledge, this characterization is the first to show the unique behaviors of sheared EC: unidirectional vortex structure, its height selection, and vortex advection. Next, based on understandings on sheared EC, we develop robust ICP desalination platform for more scalable (portable) and efficient device to remove salt ions. Utilizing nonlinear ICP between two identical IEMs, we can relocate salt ions along a specific portion of fluidic channels, generating brine and desalted flows in one channel. The salt removal ratio in this ICP desalination platform can be predicted by calculating the sheared EC's height. Also, we reveal the additional effects of nonlinear ICP on desalination process, which is quantified here for the first time, by comparison of salt removal ratio, energy consumption, and current efficiency between ICP platform with CEMs, AEMs, and ED system. In overlimiting regime, one achieves higher (lower) current efficiency compared with ED, when the mobility of relocating ions (*e.g.* anion at CEMs) is higher (lower) than that of conducting ions (*e.g.* cation at CEMs). Last, we present a new application utilizing nonlinear ICP, *i.e.* continuous-flow bio-agent preconcentrator. By controlling the nonlinear ICP region with a pressure gradient against the electric field, we concentrate variously charged bio-agents (*e.g.*, positively / negatively-charged proteins, bacteria, and cells) on the ICP boundary, and collect these pre-concentrated targets in a continuous-flow manner.

Thesis Supervisor: Jongyoon Han
Title: Professor of Electrical Engineering and Professor of Biological Engineering

Acknowledgement

I would hereby like to appreciate my mentors, colleagues, friends, and family over the course of my studies. This doctoral thesis is and will be a milestone in my life that would not have been completed without their support.

First, I would like to thank my advisor, Professor Jongyoon Jay Han, who led me into this interesting research area of physicochemical hydrodynamics and desalination. He always encouraged me to try new ideas, and helped me, with his insightful thoughts, overcome difficulties in research. In addition, I learned a lot from him outside of research as well; the ways to develop language skills as a non-native speaker in the USA, and the qualifications and ways to become an independent researcher.

Next, I would like to thank my thesis committee members, Professor John H. Lienhard and Professor Rohit Karnik, for their constructive inputs and ideas. I also appreciate faculty audiences in my defense meeting, Professor Sang-Gook Kim, Professor Nicolas hadjiconstantinou, Professor Cullen R. Buie, and Professor Alan J. Grodzinsky, for their valuable time and comments. I also thank Professor Isaak Rubinstein and Professor Boris Zaltzman for their valuable lectures about mathematical basics of electroconvection.

Also, I am indebted to current and past Han's group members: Yong-Ak Song, Sung Jae Kim, Hiong Yap Gan, Chia-Hung Chen, Aniruddh Sarkar, Hansen Bow, Rohat Melik, Leon Li, Sha Huang, Lidan Wu, Ragheb El Khaja, Zirui Li, Han Wei Hou, Sunghee Ko, and Bumjoo Kim for their help and friendship. I would also like to thank Van Sang Pham, Weng Kung Peng, Guofeng Guan, and Chen Lan, who are my collaborators in this thesis work.

I would like to thank Kwanjeong Educational Foundation in Korea for scholarship support during four years. I also thank the funding agencies that supported my research, including Advanced Research Projects Agency-Energy (ARPA-E), Singapore-MIT Alliance, Defense Advanced Research Project Agency (DARPA), and Nation Science Foundation (CBET-0854026).

Especially, I would like to express my gratitude to my previous advisor for master's degree, Professor Kaph-Yang Suh in Seoul National University, who passed away on June 29th, 2013. With his talented research ability, he taught me various experimental skills and led me to have a strong publication record when I finished the master's degree. Without his guidance and support, I could not have joined MIT as a Ph.D. candidate.

Lastly, I owe my large debt of gratitude to my family and my fiancé, Jeong Yun Kim. I deeply appreciate that they always give me unconditional love and support. My father passed down his way of studying scientific problems with sharp insight and patience to me. I would like to dedicate this thesis to my parents who have devoted themselves to me.

Table of contents

List of Figures

Figure 5.7: 20 fold continuous-flow concentrator for RBCs

Figure 5.8: 20 fold continuous-flow concentrator for RBCs and *E. coli*

List of Major Symbols

Symbol	Description	Unit
μ_i:	chemical potential of the species *i*	[J mol^{-1}]
μ^0_i:	reference chemical potential of the species *i*	[J mol^{-1}]
$\bar{\mu}_i$:	electrochemical potential of the species *i*	[J mol^{-1}]
R:	gas constant	[J $mol^{-1}K^{-1}$]
T:	temperature	[K]
a_i:	activity of the species *i*	[mol m^{-3}]
γ_i:	activity coefficient of the species *i*	[1]
c_i:	molar concentration of the species *i*	[mol m^{-3}]
k_B:	Boltzmann constant (=1.38 x 10^{-23})	[m^2kg $s^{-2}K^{-1}$]
$\vec{F}_i$:	molar flux of the species *i*	[mol $m^{-1}s^{-1}$]
D_i:	diffusivity of the species *i*	[m^2/s]
M_i:	mobility of the species *i*	[mol s kg^{-1}]
F:	Faraday's constant (= 9.65 x 10^4)	[C mol^{-1}]
N_A:	Avogadro's number (= 6.022 x 10^{23})	[mol^{-1}]
e:	elementary charge (e = 1.602 x 10^{-19})	[C]
t:	time	[sec]
$\vec{E}$:	electric field	[V/m]
φ:	electrostatic potential	[V]
z_i:	charge number of the species *i*	[1]
μ_e:	electrical mobility	[m^2 V^{-1} s^{-1}]
$\vec{u}$:	fluid velocity	[m/s]
$\vec{j}$:	current density	[A m^{-2}]
σ:	electrical conductivity	[S m^{-1}]
Λ_i:	molar conductivity	[S m^2 mol^{-1}]
ρ_e:	free charge density	[C m^{-3}]
$\vec{D}$:	electric displacement field	[C m^{-2}]
ε:	permittivity	[C V^{-1} m^{-1}]
ε_0:	permittivity of vacuum (= 8.854 x 10^{-12})	[C V^{-1} m^{-1}]
ε_r:	relative permittivity	[1]
λ_D:	Debye screening length	[m]
ρ:	fluid density	[kg m^{-3}]
f_{body}:	body force	[kg m^{-2} s^{-2}]
$f_{surface}$:	surface force	[kg m^{-2} s^{-2}]
f_e:	electrostatic body force	[kg m^{-2} s^{-2}]
τ:	shear stress	[kg m^{-1} s^{-2}]
η:	fluid viscosity	[kg m^{-1} s^{-1}]
P:	pressure	[kg m^{-1} s^{-2}]

Chapter 1

Introduction

1.1. Ion Exchange Membrane (IEM)

Ion exchange membrane (IEM) is a functional membrane which has a permselectivity of ions. According to the sign of selectivity, there are two types of IEMs: anion exchange membrane (AEM) and cation exchange membrane (CEM). Ideally, AEMs conduct negative ions (anions) only, while CEMs conduct positive ions (cations) only. This ion selectivity of the two types of IEMs is due to positively and negatively charged groups fixed to the polymer matrix of AEMs and CEMs, respectively (Fig. 1.1)[2]; for example, CEMs contain SO^{3-}, COO^{-}, PO_3^{2-}, PO_3H^{-}, $C_6H_4O^{-}$, *etc.*, and AEMs contain NH^{3+}, NRH^{2+}, NR_2H^{+}, NR^{3+}, PR^{3+}, SR^{2+}, *etc.* (R: alkyl group) (*e.g.* Nafion, which is a widely-used CEM, has SO^{3-} groups). In the nanoscale interstices of the CEM matrix, mobile cations (*i.e.* counter-ions) equilibrate fixed anions (*i.e.* negatively charged groups) electrically for satisfying electroneutrality. Simultaneously, almost all mobile anions (*i.e.* co-ions) are excluded by fixed anions from the CEM. This exclusion phenomenon (*i.e.* Donnan exclusion), which was described by F.G. Donnan in 1911 for the first time[3], allows only cations to pass through CEMs. On the same analogy, fixed cations in AEMs exclude mobile cations, so only anions can pass through AEMs.

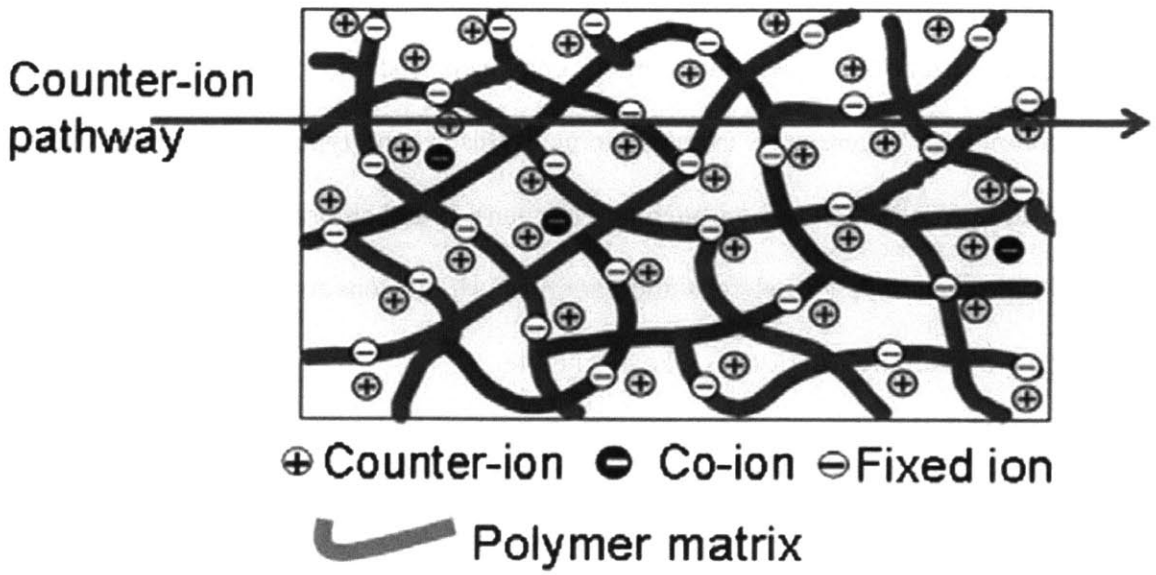

Figure 1.1. Schematic illustration of a cation exchange membrane with fixed anions on a polymer matrix (reprinted with permission from [2]).

IEMs have been widely used for various engineering applications, such as desalination, fuel cell, biosensors, and nanofluidic devices[4-6]. In such systems, IEM acts as an 'ion filter' by allowing only specific ions to pass through. Conventionally, the processes utilizing IEMs are categorized into three types:

- Mass separation process,
- Chemical synthesis process,
- Energy conversion and storage process.

The first type is to separate specific components, such as salts, acids, and bases from electrolyte solutions. Dissolved target ions in electrolytes are transferred from one phase to another under an electric potential or a concentration gradient. Electrodialysis (ED) (which was the first commercial process using IEMs)[2], Donnan dialysis [7], and diffusion dialysis [8] are classified

in this category. While the first type uses only ion transport, chemical synthesis process involves electrochemical reactions, generating certain chemicals such as acids, bases, organic, and inorganic compounds. There are various systems in this second type process; water electrolysis or water splitting (production of hydrogen and oxygen)[9] and chlorine-alkaline electrolysis[10]. In the third type process, *e.g.* fuel cells and batteries[11], the conversion of chemical energy and electric energy by Faradic reactions is a key principle.

In addition to these conventional processes, recently, the applications of IEMs extend to nanotechnologies and BioMEMS (Biomedical Micro-Electro-Mechanical Systems) fields. Advances of micro/nanofabrication technologies allow us to make nanoscale channels, and discover that the nanochannels act as IEMs with strong ion permselectivity at some conditions[4]. By manipulating ion transport precisely, researchers have developed new devices, such as nanofluidic logic gates and biomolecule preconcentrator[4, 12].

1.2. Transport of Charged Species

With the assumption of fluid continuum, the conservation of mass, charge, momentum, and energy are used to describe fluidic systems. The constitutive relations are required to uniquely define the system (*e.g.* Fick's law, Ohm's law, and Hagen-Poiseuille's law). These constitutive equations generally include the empirically determined coefficients (*e.g.* viscosity coefficient, electrical mobility, *etc.*), so the descriptions with conservation laws are called '*phenomenological models*'. All systems and processes using IEMs, including newly developed nanofluidic devices, are based on the same phenomenological model, which is the coupling of electrochemistry and physicochemical hydrodynamics. Electrochemistry describes electrochemical reactions (*i.e.* chemical reactions involving electron transfer) at the interface of an electron conductor (*e.g.* metals and semiconductors) and ionic conductor (*i.e.* electrolytes). Physicochemical hydrodynamics, which was first set as a discipline by Benjamin (Veniamin) Levich, describes hydrodynamic movements of physical, chemical, biochemical, and electrochemical components on fluid flows. Here, we focus on physicochemical hydrodynamic model in IEM-integrated systems, *i.e.* the transport of electric charges in electrolytes.

In this chapter, we build the phenomenological model to define the ion transport through IEMs and corresponding ion concentrations in bulk electrolytes. At the end, Nernst-Plank equations, Poisson's equation, and Navier-Stokes equations are derived for isothermal, incompressible, viscous Newtonian fluids and dilute electrolytes. From these equations, we also discuss electric conductivity, Ohm's law, electroneutrality, and Debye screening length. Mathematical analysis and derivations here follow the book of Physicochemical Hydrodynamics written by Prof. Ronald F. Probstein [6] and the class note of Electrochemical Energy Systems by Prof. Martin Z. Bazant [13].

1.2.1. Transport in Bulk Electrolyte

Flux and conservation of mass of charged species (Nernst-Plank equations): to describe ion transport phenomenon in electrolyte solutions, three modes of mass transport are often considered, *i.e.* diffusion, electro-migration, and convection. First, diffusion is driven by a local gradient of the chemical potential μ (which is also known as partial molar free energy). Under isothermal condition, the chemical potential from the reference potential μ^0 of the species i is given by its concentration and interactions between themselves:

$$\mu_i - \mu_i^0 = RT \ln a_i = RT \ln c_i + RT \ln \gamma_i , \tag{1.1}$$

$$a_i = \gamma_i c_i , \tag{1.2}$$

$$R = k_B N_A . \tag{1.3}$$

R is gas constant, k_B is Boltzmann constant, and T is temperature, respectively. The effective concentration, activity a_i, is the multiplication of the activity coefficient γ_i and the concentration c_i. The flux of species $\vec{F}_i$ by diffusion is then written as

$$\vec{F}_i = -M_i c_i \nabla \mu_i . \tag{1.4}$$

Here, the mobility M_i, which describes how mobile the species is. In general thermodynamics, the concept of mobility is widely acceptable, since it can be expressed for any thermodynamic forces and drift velocity:

$$\text{mobility } M_i = \frac{\text{drift velocity}}{\text{thermodyanamic force}} . \tag{1.5}$$

This mobility is directly related to diffusivity described by Einstein relation in kinetic theory (Eq. 6). We can drive the diffusional flux by substitute Eq. 1.1 into Eq. 1.4:

$$D_i = M_i RT , \tag{1.6}$$

$$\vec{F}_i = -M_i RT\left[1+\frac{\partial \ln \gamma_i}{\partial \ln c_i}\right]\nabla c_i = -D_i\left[1+\frac{\partial \ln \gamma_i}{\partial \ln c_i}\right]\nabla c_i, \tag{1.7}$$

where D_i is the diffusivity. In this thesis, we only consider the sufficiently diluted electrolytes, and neglect all interactions including electrostatic interactions between species themselves. Then, the activity coefficient becomes 1, and the flux reduces to the well-known Fick's law of diffusion:

$$\vec{F}_i = -D_i \nabla c_i. \tag{1.8}$$

Secondly, under the applied electric field, the charged species migrate in a preferred direction, *i.e.* electro-migration. The force on a species f_i is the multiplication of its charge and the electric field E, which is a negative gradient of the electrostatic potential φ:

$$f_i = -z_i F \nabla \varphi, \tag{1.9}$$

$$\vec{E} = -\nabla \varphi. \tag{1.10}$$

z_i is charge number of the species i, and F is Faraday's constant (F=$N_A e$, where e is elementary charge (=1.602x10^{23} mol^{-1})). The flux of species i by electro-migration is then

$$\vec{F}_i = -M_i z_i F c_i \nabla \varphi. \tag{1.11}$$

Here, we can define electrical mobility $\mu_{e,i}$, which is measured and used frequently:

$$\mu_{e,i} = -M_i z_i F. \tag{1.12}$$

We also can drive the flux of diffusion and migration together by substituting the electrochemical potential $\bar{\mu}_i$ instead of the chemical potential μ into Eq. 1.4. The electrochemical potential includes electrostatic term:

$$\overline{\mu_i} - \overline{\mu_i^0} = RT \ln a_i + z_i F \varphi. \tag{1.13}$$

Lastly, convection is the transport mechanism by mechanical forces, *i.e.* in general a hydrostatic pressure gradient. More precisely, we need to use the term '*advection*', which

specifically indicate the transport mechanism of species by fluid's bulk motion (in physics and fluid dynamics field, *convection* is the sum of diffusion and advection); fluid bulk motion is driven by mechanical forces. However, many major textbooks[5, 6] use the term '*convection*' to represent advection and describe diffusion separately, so we follow this custom. When the electrolyte is diluted enough, the average velocity of species *i*, u_i* is equal to fluid velocity $\vec{u}$. Then, the flux by convection can be written as

$$\vec{F}_i = c_i \vec{u} . \tag{1.14}$$

For dilute solution, we can linearly superpose the fluxes by diffusion, electro-migration, and convection:

$$\vec{F}_i = -D_i \nabla c_i - M_i z_i F c_i \nabla \varphi + c_i \vec{u} , \tag{1.15}$$

which is called as the Nernst-Plank equation. It is noted that this equation neglects any kinetic coupling between the species themselves, or individual transport mechanisms.

If we neglect any productions of species *i*, the continuity equation for species *i* becomes

$$\frac{\partial c_i}{\partial t} + \nabla \vec{F}_i = 0 . \tag{1.16}$$

Assuming incompressibility of fluid (Eq. 1.17), the continuity equation can be expressed

$$\nabla \cdot \vec{u} = 0 , \tag{1.17}$$

$$\frac{\partial C_i}{\partial t} + \vec{u} \cdot \nabla c_i = \nabla \cdot \left(D_i \nabla c_i + M_i z_i F c_i \nabla \varphi \right) . \tag{1.18}$$

Electrical current and ion fluxes: Ideally, we assume all current through IEMs is contributed by ions *i* only, thus current density $\vec{J}$ is:

$$\begin{aligned} \vec{J} &= F \sum_i z_i \vec{F}_i \\ &= -F \sum_i z_i D_i \nabla c_i - F^2 \nabla \varphi \sum_i M_i z_i^2 c_i + F \vec{u} \sum_i z_i c_i \end{aligned} \tag{1.19}$$

If there are no flows and concentration gradients, the first and third terms of Eq. 1.19 becomes zero. Then the ion flux only by electro-migration gives rise to the current:

$$\vec{J} = -F^2 \nabla\varphi \sum_i M_i z_i^2 c_i \,, \tag{1.20}$$

Here, we change Eq. 1.20 as an expression of Ohm's law by defining the electrical conductivity σ electrolyte solutions:

$$\vec{J} = \sigma\vec{E} = -\sigma\nabla\varphi \,, \tag{1.21}$$

$$\sigma = F^2 \sum_i M_i z_i^2 c_i = \sum_i \frac{D_i}{k_B T} (z_i e)^2 c_i \,. \tag{1.22}$$

The electrolyte conductivities which is normalized by the concentration, *i.e.* molar conductivity Λ_i, is often used:

$$\Lambda_i = \frac{\sigma}{c_i} = F^2 z_i^2 M_i \,. \tag{1.23}$$

1.2.2. Electrostatics

To connect the distribution of electric charge (by ions in electrolytes) and the electric field, we visit Gauss's law which is one form of Maxwell's equations in classical electrodynamics. In differential form, the total electric flux through a closed surface is proportional to the total electric charge inside:

$$\rho_e = \nabla \cdot \vec{D} \,, \tag{1.24}$$

where ρ_e is the free charge density and $\vec{D}$ is electric displacement field. In a linear dielectric material (neglecting electric polarization), the electric field separates charges (*e.g.* cation and anion) slightly, inducing a local electric dipole moment:

$$\vec{D} = \varepsilon\vec{E} \,. \tag{1.25}$$

Here, ε is permittivity, and it is equal to the multiplying of the vacuum permittivity ($\varepsilon_0 = 8.854 \times 10^{-12}$ C V^{-1} m^{-1}) by the relative permittivity ε_r. Assuming the free charge density in electrolytes is simply the sum of the ion charges (mean-field approximation), and substituting Eq. 1.25 into Eq.1.24, Poisson's equation is driven:

$$\sum_i z_i F c_i = \rho_e = \nabla \cdot (\varepsilon \nabla \varphi). \tag{1.26}$$

Poisson-Nernst-Plank Equations and Debye screening length: When flow velocity $\vec{u}$ is known and constant, the system is then fully specified with Eq. 1.18 and Eq. 1.26, *i.e.* Poisson-Nernst-Plank equations (PNP):

$$\begin{aligned} &\frac{\partial c_i}{\partial t} + \vec{u} \cdot \nabla c_i = \nabla \cdot \left(D_i \nabla c_i + M_i z_i F c_i \nabla \varphi \right) \\ &\sum_i z_i F c_i = \rho_e = \nabla \cdot (\varepsilon \nabla \varphi) \end{aligned} \tag{1.27}$$

In bulk electrolytes, the solution is electrically neutral because charged ions hold closely together, satisfying the so-called electroneutrality condition.

$$\sum_i z_i c_i = 0. \tag{1.28}$$

In addition, one can state, in electrical steady state, there is no local accumulation of charge, *i.e.* the current continuity (or conservation of charge):

$$\nabla \cdot \vec{J} = 0. \tag{1.29}$$

It is noted that the electroneutrality cannot be used with Poisson's equation, Eq. 1.26, since the system is overspecified (electroneutrality condition is an approximate solution of Poisson's equation). Appling the electroneurality into Poisson's equation, the electrostatic potential is then governed by Laplace's equation (the permeability ε is constant):

$$\nabla^2 \varphi = 0. \tag{1.30}$$

However, when we apply the current continuity (Eq. 1.29, which is more generally applicable

than the electroneutrality condition) to Nernst-Plank equations (Eq. 1.19), we get

$$F\sum_i z_i \nabla \cdot (D_i \nabla c_i) + \nabla \cdot (\sigma \nabla \varphi) = 0 . \tag{1.31}$$

The Laplace's equation (Eq.1.30) only holds when the first term of LHS of Eq. 1.31 is zero.

This paradox is often solved by matched asymptotic expansion (also known as boundary layer theory) and quasi-electroneutrality, which is used to analyze thin electric double layer (EDL) near charged walls[6]. In this concept, the regions are separated into the outer region (quasineutral bulk) and the inner region (quasi-equilibrium diffuse double layer). In the outer region located far from the wall, we can assume electroneutralitly ($\rho_e \approx 0$). All the terms in the PNP equations are O(1), except the term ρ_e=O($\varepsilon << 1$); for example, the permittivity of the water at 298K is 6.93 x 10^{-10} [C V^{-1} m^{-1}]. However, in the thin inner region near the charged wall, the systems characteristic length becomes smaller, and the free charge term in Poisson's equation (ρ_e=O($\varepsilon << 1$)) becomes dominant. Here, the characteristic length which divides the inner and outer regions is *Debye screening length* λ_D:

$$\lambda_D = \sqrt{\frac{\varepsilon k_B T}{\sum_i z_i e c_{i,bulk}}} . \tag{1.32}$$

This length is driven from the non-dimensional Poisson's equation (see Appendix, Eq. A1-A4).

1.2.3. Electrokinetics

Conservation of momentum of fluid (Navier-Stokes Equations): Again, the system is fully defined by PNP equations when the flow velocity is known and constant. PNP equations are therefore widely used to analyze electro-diffusion models in electrolytes (electrostatic models). To take the system one step further, when external body forces exist and define flow velocity profiles, we need to consider the conservation of momentum (electrokinetic models).

Before we visit the conservation of momentum, we set the equations of conservation of mass for a fluid particle. The continuity of fluid becomes

$$\frac{\partial \rho}{\partial t} + \nabla \cdot (\rho \vec{u}) = 0. \tag{1.33}$$

Here, ρ is fluid density. When this density of fluid particle is constant (*i.e.* incompressible flow), the material derivative of fluid density becomes zero:

$$\frac{D\rho}{Dt} = \frac{\partial \rho}{\partial t} + (\vec{u} \cdot \nabla)\rho = 0. \tag{1.34}$$

Then, we can drive the equation of fluid continuity for incompressible flow, $\nabla \cdot \vec{u} = 0$ (Eq. 1.17).

From Newton's second law, the equation of conservation of momentum for a fluid particle can be written as

$$\rho \frac{D\vec{u}}{Dt} = f_{body} + f_{surface}. \tag{1.35}$$

A fluid element is accelerated by applied forces on its body (body force f_{body}) and on its surface (surface force $f_{surface}$). The body forces are linearly proportional to the total volume or mass of fluid elements, such as gravity and electrostatic / electromagnetic forces. For simplicity, in this thesis, we neglect the gravity and electromagnetic forces, and focus on the effect by electrostatic body force under constant electric fields. The electrostatic body force on charged species is

$$f_e = -\rho_e \nabla \varphi. \tag{1.36}$$

For a viscous Newtonian fluid, the surface force on a fluid particle by viscous stress (*i.e.* shear stress τ) is proportional to the fluid viscosity η and the gradient of fluid velocity:

$$\tau = \eta \nabla \vec{u}, \tag{1.37}$$

$$f_{surface} = \nabla \cdot \tau = \eta \nabla^2 \vec{u}. \tag{1.38}$$

Adding the surface force term by normal stress (*i.e.* pressure) and substituting Eq. 1.36-1.38 into

Eq. 1.35, we can obtain Navier-Stokes (NS) equations for electrokineitc models:

$$\rho\left(\frac{\partial \vec{u}}{\partial t}+\vec{u}\cdot\nabla\vec{u}\right)=-\nabla P+\eta\nabla^2\vec{u}-\rho_e\nabla\varphi. \tag{1.39}$$

Here, the fluid viscosity η is treated as constant for incompressible, isothermal, and single-phase homogeneous fluid. With the continuity equation (Eq. 1.17), NS equations can fully specify the motion of fluid flows under proper boundary conditions (*e.g.* no-slip condition at fluid-solid interface).

In microscale electrokineitc systems, LHS of Eq. 1.39 is generally neglected, because the system is on low frequency, quasi- steady state and inertia-free. NS equation is then simplified to Stokes' equations:

$$\nabla P=\eta\nabla^2\vec{u}-\rho_e\nabla\varphi. \tag{1.40}$$

By substituting Poisson's equation (Eq. 1.26), we get

$$\nabla P=\eta\nabla^2\vec{u}+\varepsilon(\nabla^2\varphi)\nabla\varphi, \tag{1.41}$$

which can describe various electrokinetic phenomena, including electro-osmotic flow, electrophoresis, and streaming current / potentials[6].

Full set of PNP-NS equations: In summary, we can model complex ion transport phenomenon through IEMs using Poisson-Nernst-Plank equations (Eq. 1.27) and Navier-Stokes equations (Eq. 1.39) (PNP-NS). Non-dimensionalized forms of PNP-NS equations are also available in Appendix A (Eq. A1-A7).

1.3. Ion Concentration Polarization (ICP)

Ion Concentration Polarization (ICP) refers to the additional voltage drop (or internal resistance) across the electrolyte associated with concentration gradients of reactants or ions. Selective reaction / rejection / addition of species on permselective membranes or electrodes generate dynamic change in species' concentrations. This ICP phenomenon governs the limits of the transport of reactants (*e.g.* ions) to the reaction sites (*e.g.* IEMs or electrodes), so it determines optimal operating conditions of the system. (Fig. 1.2a)[4, 6, 12].

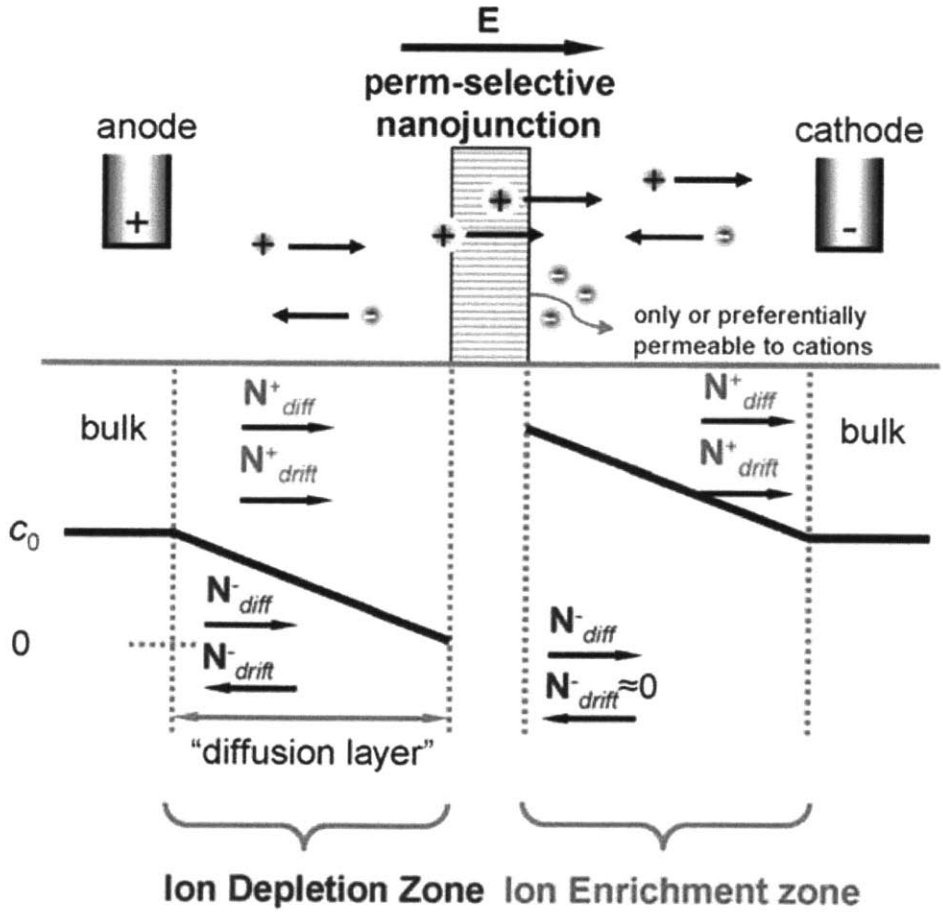

Figure 1.2. Schematic illustration of ion concentration polarization at a cation exchange membrane (adapted from [12]). C_0, N^+, N^-, and E represent the ion concentration of bulk solution, cation flux, anion flux, and electric field, respectively. The subscripts *diff* and *drift* indicate the diffusion and electric drift.

1.3.1. Linear ICP and Limiting Current

In the simplest 1-D system without convective transport ($\vec{u}=0$), when an electric field is applied across a cation exchange membrane (CEM), cations move to a cathode by electric drift through the CEM (anions cannot pass through the CEM) (Fig. 1.2). Here, the cation conductivity of the CEM is higher than that of a bulk solution, inducing the decrease (increase) of the cation concentration at the anodic (cathodic) side, *i.e.*, ion depletion zone and ion enrichment zone (Fig. 1.2). The fast, selective conduction of cations in the CEM is counteracted by diffusion, generated by concentration gradients near the CEM, leading ICP. To satisfy electroneutrality in the bulk solution, the anion concentration follows the cation concentration on both sides. The diffusion of the anion by the concentration gradient is offset by the electric drift. As a result, the electric current is transmitted only by the cation, and the anion flux across the system is zero.

This 1-D ICP system can be modeled with PNP equations (Eq. 1.27), and can be solved analytically (Fig. 1.3). For a dilute, binary, quasi-neutral electrolyte, the diffusivity of cation and anion $D_{\pm}$ and non-dimensionalized electrochemical potentials of cation and anion $\tilde{\mu}_{\pm}$ becomes:

$$D_{\pm} = \text{constant}, \tag{1.42}$$

$$\tilde{\mu}_{\pm} = \ln(z_{\pm}c_{\pm}) + z_{\pm}\tilde{\varphi},\ \tilde{\varphi} = F\varphi / RT\,. \tag{1.43}$$

Non-dimensionalized PNP equations with quasi-electroneutrality condition becomes (neglecting the inner region near the CEM):

$$\begin{aligned} &\frac{\partial c_{\pm}}{\partial t} = \nabla\cdot\vec{F}_{\pm} = D_{\pm}(\nabla^2 c_{\pm} + z_{\pm}\nabla\cdot(c_{\pm}\nabla\tilde{\varphi})) \\ &\sum z_{\pm}Fc_{\pm} = 0 \quad\Leftrightarrow\quad \nabla\cdot\vec{J} = 0 \end{aligned}\,. \tag{1.44}$$

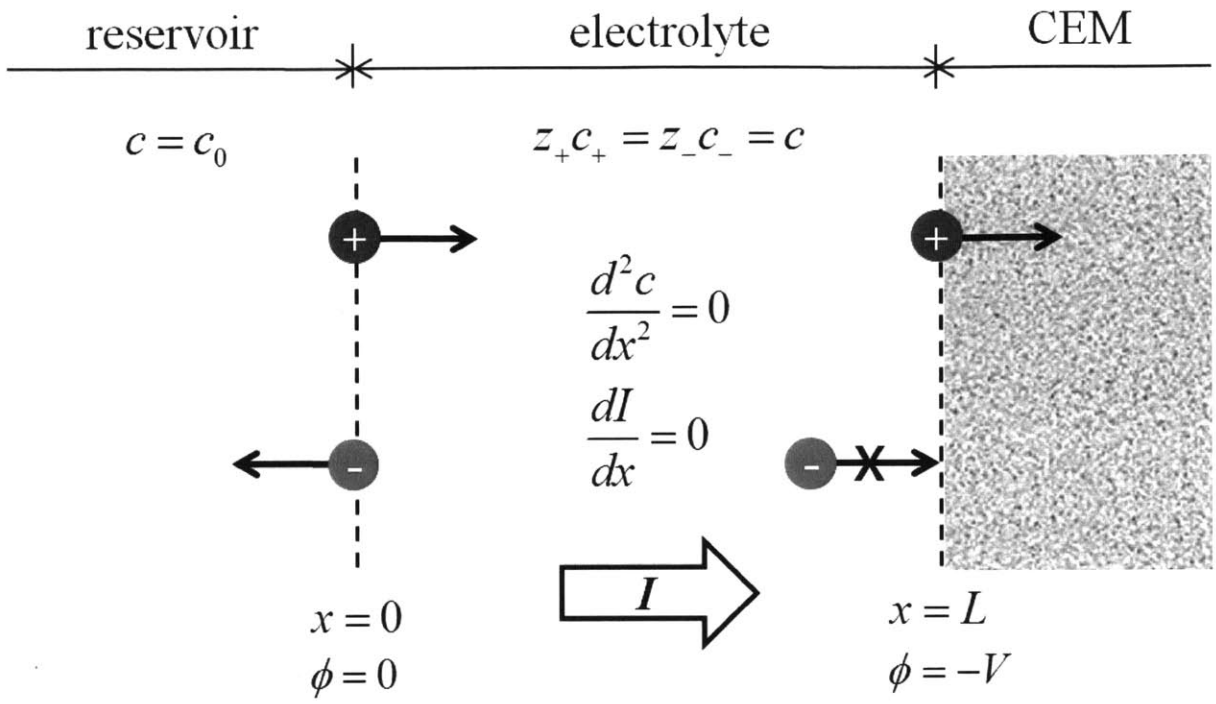

Figure 1.3 Model for analyzing linear ICP phenomenon. 1-D steady current I (or ions) flows through ideal cation-selective membrane (*e.g.* CEM) at $x=L$ in a dilute binary electrolyte. The well-mixed reservoir fix the ion concentration $c=c_0$ at $x=0$.

When we section the model system by three region (reservoir, electrolyte, and membrane), the ion concentration in the reservoir is constant as c_0 (at $x<0$)(Fig. 1.3). Also, in electrolyte, the salt concentration for binary salts c is defined as

$$z_+c_+ = z_-c_- = c\,. \tag{1.45}$$

If the system is steady ($\partial / \partial t = 0$), the gradient of the flux of cation and the flux of anion should be zero because the ideal CEM conducts only cations:

$$0 = \nabla \cdot \vec{F}_\pm\,, \tag{1.46}$$

$$\frac{dF_+}{dx} = 0,\ F_- = 0 \quad \left(\because \frac{dF_-}{dx} = 0,\ F_-(x=0) = 0 \right). \tag{1.47}$$

Then, from the constant zero flux of anion, we can induce the ion concentration c follows Boltzmann distribution. The anion flux is linearly proportional to the gradient of its

electrochemical potential, according to the general NP equations (Eq. 1.4), so the electrochemical potential should be constant when the flux is zero:

$$\tilde{\mu}_{-} = \ln(z_{-}c_{-}) - z_{-}\tilde{\varphi} = \text{constant}. \tag{1.48}$$

Then,

$$\tilde{\mu}_{-}(0 < x < L) = \tilde{\mu}_{0}(x = 0) = \ln(c_{0}), \tag{1.49}$$

$$\Rightarrow c_{-} = \frac{c_{0}}{z_{-}} \exp(z_{-}\tilde{\varphi}). \tag{1.50}$$

From the Boltzmann distribution of anions, we can drive the distribution of electric potential in this system:

$$\tilde{\varphi} = \frac{1}{z_{-}} \ln \tilde{c},\ \tilde{c} = \tilde{c}_{-} = z_{\pm}c_{\pm} / c_{0}. \tag{1.51}$$

By taking into account the constant flux of cations, we can also calculate the current I (or cation transfer) through the CEM. Setting the membrane area as A,

$$\vec{F}_{+} = \text{constant}, \tag{1.52}$$

$$I = A\vec{J} = z_{+}F\vec{F}_{+}A = -z_{+}FA\left(\frac{dc_{+}}{dx} + z_{+}c_{+}\frac{d\tilde{\varphi}}{dx}\right). \tag{1.53}$$

Substituting Eq. 1.51 into Eq. 1.53,

$$I = -\frac{AFc_{0}}{L} D_{+}\left(1 + \frac{z_{+}}{z_{-}}\right)\frac{d\tilde{c}}{d\tilde{x}},\ \tilde{x} = x / L. \tag{1.54}$$

Here, the first (second) term indicates the contribution of diffusion (electro-migration) on the current. According to the current equation Eq. 1.54, it has been revealed that the concentration profiles by ICP are simply linear at the given current I (Fig. 1.2 and Fig. 1.4a). Here, the non-dimensional concentration gradient ($-d\tilde{c}/d\tilde{x}$) cannot be larger than 1 because the sign of ion concentration at x=L becomes negative; this is physically not allowed (when $\tilde{I} > 1$ in Fig. 1.4a).

If we define the limiting current $I_{\lim}$ when $-d\tilde{c}/d\tilde{x}=0$,

$$I_{\lim} = \frac{AFc_0}{L} D_+ \left(1+\frac{z_+}{z_-}\right). \tag{1.55}$$

$$\tilde{I} = \frac{I}{I_{\lim}} = -\frac{d\tilde{c}}{d\tilde{x}}. \tag{1.56}$$

Then, the non-dimensionalized concentration and electric potential profile becomes:

$$\tilde{c} = 1-\tilde{I}\tilde{x}, \tag{1.57}$$

$$\tilde{\varphi} = \frac{1}{z_-}\ln(1-\tilde{I}\tilde{x}). \tag{1.58}$$

Now we see the limiting current $I_{\lim}$ as $\tilde{I}\to 1$, $\tilde{C}(\tilde{x}=1)\to 0$, $\tilde{\phi}(\tilde{x}=1)\to\infty$. At the diffusion-limited current $I_{\lim}$, the all ions vanish at the interface of electrolyte and the membrane (Fig. 1.4a), and the electric potential diverges (Fig. 1.4b). Accordingly, from the current-voltage curve, the current is saturated at the limiting current, and the curve shows the same I-V characteristics as an ideal diode by ICP (Fig. 1.5):

$$\tilde{\varphi}(\tilde{x}=1) = -\tilde{V} = \frac{1}{z_-}\ln(1-\tilde{I}),\ \tilde{V} = eV/k_BT, \tag{1.59}$$

$$\Rightarrow \tilde{I} = 1-e^{-z_-\tilde{V}}. \tag{1.60}$$

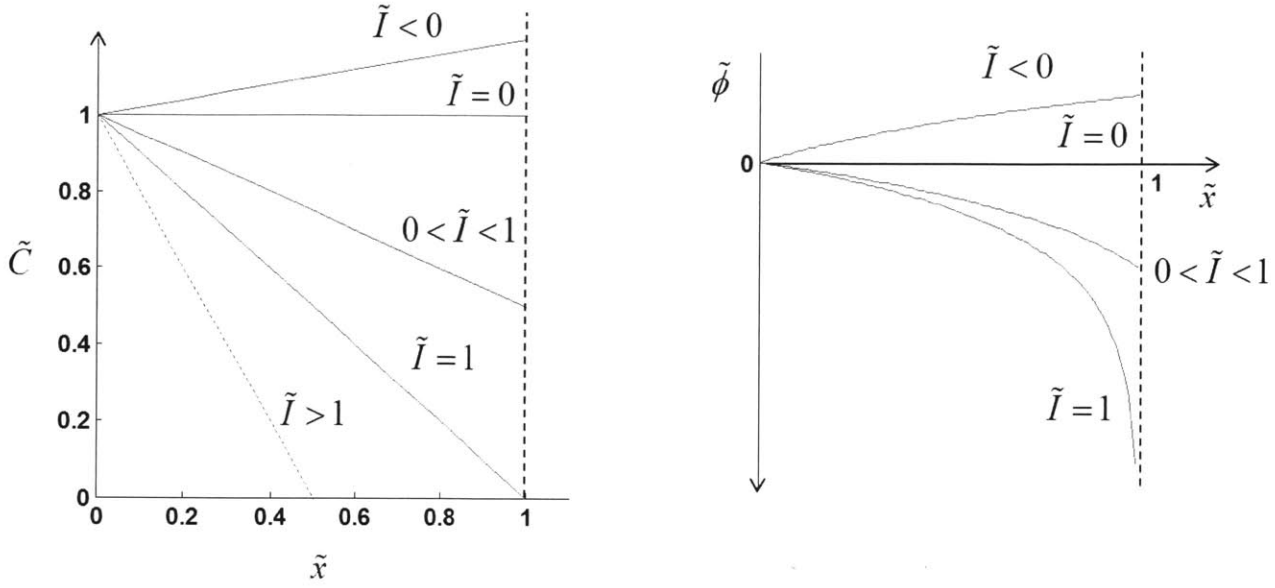

Figure 1.4 a) Non-dimensionalized ion concentration and **b)**electrostatic potential profiles in the model system of Fig. 1.3 under different currents.

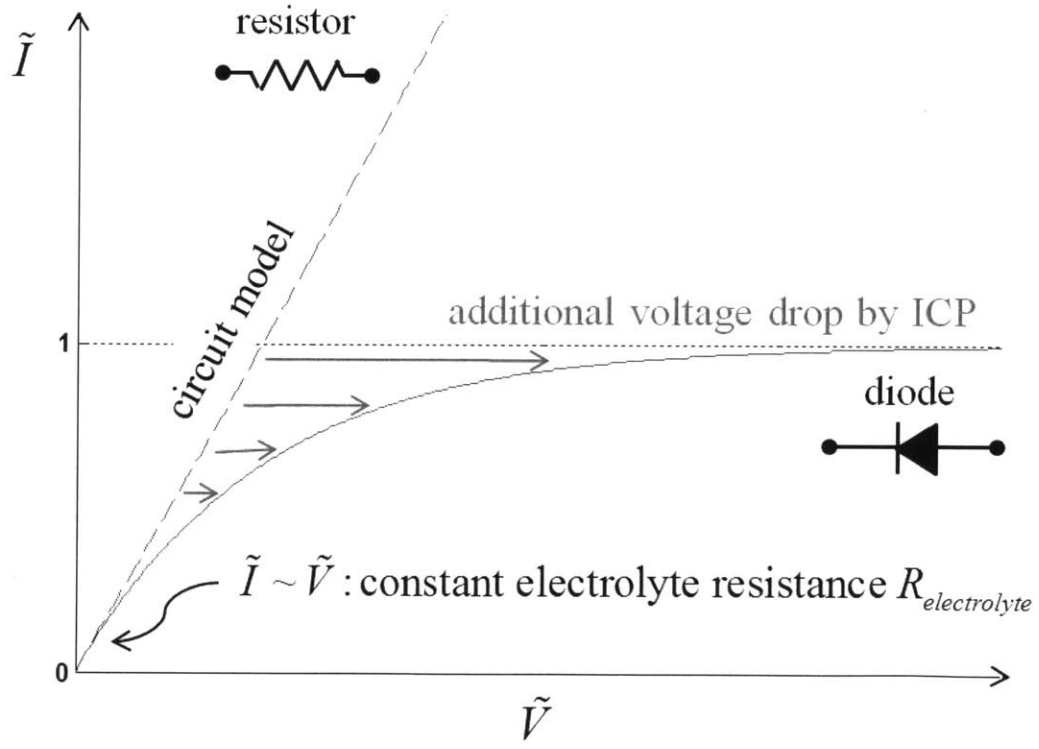

Figure 1.5 Current-voltage relation for the model system of Fig. 1.3. Internal resistance of the electrolyte becomes infinite at higher voltage by ICP, and the current is saturated at the limiting current. At lower voltage regime, the current is linearly proportional to the applied voltage, which is predicted in Ohm's law (*i.e.* the constant resistance of electrolyte).

Such limiting current by linear ICP has been frequently observed in various electrochemical systems with IEMs, such as fuel cells and electrodialysis[6, 14, 15]. The preceding analysis of linear ICP and limiting current in electrolytes can be traced back to Walther Nernst a century ago, and has fundamental / practical importance. Because the limiting current implies the point of the maximum ion flux and the point when the internal resistance becomes infinity, it becomes the standard condition to define optimized operating conditions for electrochemical systems with IEMs. Various ways to define the limiting current has been developed for more complex 2-D systems analytically (*e.g.* convective-diffusion model[6]) and empirically [16].

The preceding linear ICP theory, however, loses validity when the current approaches the limiting current, since the quasi-electroneutrality breaks down when the ion concentration goes to zero near IEMs.

1.3.2. Nonlinear ICP and Overlimiting Current

In 1988, Rubinstein *et al.*[17] found that the current starts to increase again after it is saturated in electrodialysis (ED) (Fig. 1.6a). This increase indicates that ions can pass through IEMs, overcoming the diffusion-limit (limiting current). The traditional convective-diffusion model with the Nernst-Plank-Poisson equations cannot predict this nonlinear ICP phenomenon, called the overlimiting conductance (OLC), which is observed in various IEM-electrolyte interfacial models[18-21].

The nonlinear ICP model includes the three current regimes: Ohmic (I), limiting (II), and overlimiting current (III) regimes (Fig. 1.6b). The existence of OLC has drawn much attention from physicists and engineers, because of its non-intuitiveness and the possibility to improve electrochemical systems' performance. Although the basic, 1D theoretical modeling of the nonlinear ICP has been presented in the pioneering works of Rubinstein and Zaltzman [19], it is

still an ongoing scientific challenge because of the multiphysics, multiscale nature of the problem.

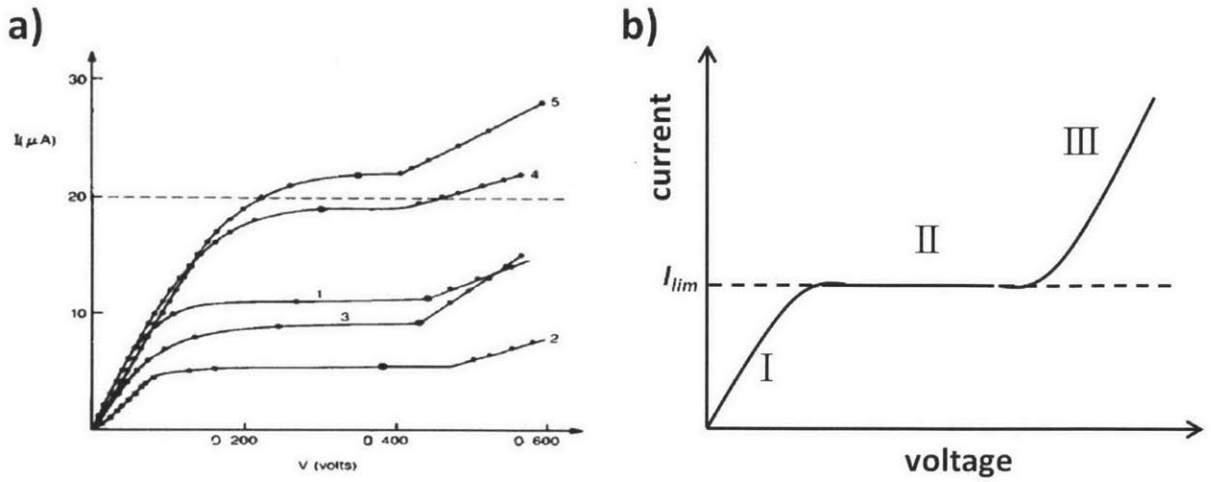

Figure 1.6 a) Current-voltage curves measured in ED systems (reprinted with permission from [17]) and **b)** the typical current-voltage relation of the interfacial systems with IEMs in liquid electrolytes. The current is saturated (*i.e.* limiting current), but it increases again (*i.e.* overlimiting current).

1.4 Thesis Objectives

The objectives of this Ph.D thesis are the fundamental study and exploration of applications of nonlinear ion concentration polarization (ICP) and overlimiting current (OLC). To achieve the goals, in Chapter 2, we visualize the nonlinear ICP and corresponding OLC in real electrochemical system, *i.e.* electrodialysis (ED). Then, we analyze the effects of the nonlinear ICP on ED system. In Chapter 3, based on the visualized nonlinear ICP and its effects, we clarify that the source of OLC is electroconvective vortex (EC), and characterize EC in ED system. Lastly, in Chapter 4 and 5, we explore novel applications utilizing the nonlinear ICP, *i.e.* single-step water desalination and purification and high-throughput bio-agent preconcentration for water monitoring. Specifically, the proposed objectives already accomplished in the thesis are:

a. Development of a universal experimental platform for studying the nonlinear ICP.

b. Microscopic analysis of the effects of nonlinear ICP and OLC on ion transport, salt removal performance, and current efficiency in ED system.

c. Clarification of the source of nonlinearity in ICP (*i.e.* electroconvection (EC)).

d. Characterization of electroconvection (EC) under shear flow in electrodialysis (ED).

e. Development of *en bloc* desalination / purification method (removing salt ions and charged bio-agents at one time) from brackish water by nonlinear ICP between two identical IEMs.

f. Clarification and quantification of desalting performances of new ICP platform vs. ED

g. Development of the strategy to scale-up new ICP desalination methods for commercialization.

h. Development of fast, massive bio-agent preconcentration method in a continuous manner.

References

[1] N. P. Berezina, N. A. Kononenko, O. A. Dyomina, and N. P. Gnusin, Adv Colloid Interfac **139**, 3 (2008).
[2] H. Strathmann, Desalination **264**, 268 (2010).
[3] F. G. Donnan, J Membrane Sci **100**, 45 (1995).
[4] R. B. Schoch, J. Y. Han, and P. Renaud, Rev Mod Phys **80**, 839 (2008).
[5] H. Strathmann, *Ion-exchange Membrane Separation Processe* (Elsevier, 2004), In Membrane Science and Technology Series.
[6] R. F. Probstein, *Physicochemical Hydrodynamics: An Introduction* (Wiley-Interscience, New York, 2003), 2 edn.
[7] M. Hichour, F. Persin, J. Sandeaux, and C. Gavach, Sep Purif Technol **18**, 1 (2000).
[8] J. Y. Luo, C. M. Wu, T. W. Xu, and Y. H. Wu, J Membrane Sci **366**, 1 (2011).
[9] K. N. Mani, J Membrane Sci **58**, 117 (1991).
[10] T. W. Xu, Resour Conserv Recy **37**, 1 (2002).
[11] V. Mehta, and J. S. Cooper, J Power Sources **114**, 32 (2003).
[12] S. J. Kim, Y. A. Song, and J. Han, Chem Soc Rev **39**, 912 (2010).
[13] M. Z. Bazant, 2011), pp. available from: http://ocw.mit.edu/courses/chemical.
[14] J. Newman, and K. E. Thomas-Alyea, *Electrochemical Systems* (John Wiley and Sons, Inc., 2004), third Edition edn.
[15] A. J. Bard, and L. R. Faulkner, *Electrochemical Methods: Fundamentals and Applications* (John Wiley and Sons, Inc., 2001), second edition edn.
[16] T. B. Drew, *Mass-transfer measuremetns by the limiting-current technique* (Academic Press, 1978), Vol. 10.
[17] I. Rubinstein, E. Staude, and O. Kedem, Desalination **69**, 101 (1988).
[18] I. Rubinstein, Phys Fluids a-Fluid **3**, 2301 (1991).
[19] I. Rubinstein, and B. Zaltzman, Phys Rev E **62**, 2238 (2000).
[20] S. J. Kim, Y. C. Wang, J. H. Lee, H. Jang, and J. Han, Phys Rev Lett **99**, 044501 (2007).
[21] G. Yossifon, and H. C. Chang, Phys Rev Lett **101**, 254501 (2008).

Chapter 2

Ion Concentration Polarization (ICP) in Electrodialysis (ED)[1]

2.1. Introduction to Electrodialysis (ED)

Electrodialysis (ED) is an one of the membrane-based separation process utilizing ion exchange membranes (IEMs)[1-3]. Ideally, anion exchange membranes (AEM) conduct negative salts (anions) only, while cation exchange membranes (CEM) conduct positive salts (cations) only. With this ion selectivity, the juxtaposed AEM and CEM can remove salts from incoming salty water under an electric field. The concept of ED was first suggested in early 20th century[4, 5], but a modern ED system known today was developed only in 1950, along with the first production of the synthetic ion exchange membranes (IEM)[6]. After installing the first commercial ED plant by Ionics, Inc. for Aramco (Saudi Arabia) in 1954, ED technology has achieved many improvements; membrane fouling and scaling were significantly reduced by electrodialysis reversal (EDR), and production of ultrapure water was achieved by electrodionization (EDI)[1, 3].

Despite these progresses, electrodialysis (ED) became a niche technology because of the dramatic improvement of Reverse Osmosis (RO), which is currently the dominating technology in desalination market[1, 2, 7]. However, ED technology still enjoys several important advantages, such as high water purity, scalability, and ion controllability. Firstly, ED technology can remove certain important ionic species more efficiently than RO, because it is not relying on the size of the molecules. For example, boron removal efficiency of RO (~30%) is much worse than that of EDI (~95%)[1]. Secondly, ED is scalable, and therefore ideal for on-demand, small-

[1] The published journal paper (R. Kwak, G. F. Guan, W. K. Peng, and J. Han, Desalination **308**, 138 (2013)) was used in its entirety for Chapter 2, with minor updates and modifications. R. K. and J. H. conceived the idea, designed the experiments, and wrote the manuscript. R. K. carried out the experiments and analyzed the data. G. G and W. K. P. fabricated the PDMS molds by 3D printing. J. H. supervised the study.

scale desalination, which would address many of the water challenges of remote, resource-limited areas[8, 9]. Contrast to RO process, which requires a high pressure pump to overcome significant osmotic pressure of salty water, ED process can be miniaturized. Lastly, ED process can be generalized as an ion manipulation process, resulting in many new applications: acid and base production, water softening, and waste water treatment[3].

The present IEMs for ED, have 96~99% ion selectivity and require only ~5% the total voltage drop of the entire ED system. Therefore, the technology of IEM is often considered mature, and it is unlikely to produce any further improvement of ED process[1]. On the other hand, system parameters related to the ion transport within the cell are not fully optimized, nor well characterized. Optimization of ED systems for better performance would require detailed, microscopic system characterization as well as robust theoretical (numerical) model for the process. Yet, ED systems engineering have been often relying on a "black-box" approach, where only inputs (current or voltage, flow rate, *etc.*) and outputs (voltage or current, conductivity *etc.*) of the systems are tracked, while various system parameters are varied, to optimize the system. This is in part due to the scientific complexity of the ED process itself. Current through IEMs typically initiate Ion Concentration Polarization (ICP) near the membrane, and physical modeling of ICP is an ongoing scientific challenge, due to its multiphysics, multiscale nature of the problem. Although the ion transport through ion exchange membranes has been theoretically studied in the pioneering works of I. Rubinsten and B. Zaltzman[10, 11], it is still non-trivial to build a predictive engineering model for a ED system, with a full consideration of system parameters and geometrical complexities. Often, these models either capture only 1-D ion transport behaviors around the membrane, or fail to incorporate the fluid flow and other details[12]. On the other hand, direct experimental monitoring of ED process *in situ* has not been

reported previously. V. A. Shaposhnik *et al.*[13-15] have developed the laser interferometric method for profiling salt concentration in ED process *in situ*, but this method is providing insufficient details regarding the dynamic changes of concentration / flow in ED unit cell, especially in high current regime[12].

In this chapter, we present a microscale experimental platform of electrodialysis (ED) which enables detailed, microscopic observation of ED process *in situ*, using a standard microscope. With this platform, we visualize fluid flow and concentration profile in ED systems directly for the first time. Both fluid flows and concentration profiles in ED undergo significant transitions, from a low current (Ohmic regime) to a high current (overlimiting regime) conditions. We also investigated the relationship between the salt removal performance and the observed concentration and flow patterns, and discussed insights revealed in this experiment for the future optimization of ED system in general.

2.2. Microscale ED Platform

2.2.1. Device Fabrication and Operation

Fig. 2.1a shows a micro ED platform with a single unit cell defined by the three IEMs, along with one desalted and one concentrated channels. To visualize ion and fluid transport within the cell, a microchannel is formed between the two IEMs. Polydimethylsiloxane (PDMS) is selected as a material for device fabrication because of its optical transparency and flexibility. Flexible PDMS device can make conformal contact with the surface of membranes and electrodes, preventing fluid leakages. Two PDMS blocks have five slots for three ion exchange membranes (IEM) and two electrodes (Fig. 2.1a). Microchannels are formed when the IEMs and the electrodes are positioned in the slots, and the two PDMS blocks are bonded. The width of the all channels is 1 mm, and the height of the channels is 200μm. To fabricate this PDMS slots, the structures are engraved in relief by the stereolithograph process (also known as 3D printing, Viper si2 SLA® system, 3D Systems Inc., Rock Hill, SC). The material for this mold is Watershed XC 11122 (DSM, inc., Netherlands). PDMS is then poured into the mold, cured, and casted away from the mold. The dry IEMs (two AEMs and one CEM) and electrodes are inserted into the slots on the lower PDMS block. Fumasep® FTAM-E and FTCM-E (FuMA-Tech GmbH, Germany) are used as an AEM and a CEM, respectively. The electrode is a 0.4 mm thick Al plate (McMaster-Carr, Inc, Atlanta, GA). Holes are punched on the upper PDMS block for connecting syringe pumps, conductivity meter, and electric wires. The two PDMS blocks are then bonded irreversibly by oxygen plasma treatment. Next, the channels of this assembled unit are filled with deionized water for 48 hours at 20 degree. During this period, swelling of IEMs occurs, resulting in the volume expansion. This expansion helps to seal any gaps between the IEMs and the PDMS blocks, forming a tight seal between chambers.

Fig. 2.1b shows the platform for visualizing ED systems. The micro ED system is loaded onto a commercial microscope (Fig. 2.1b). Real time, microscopic images of ED cell can be obtained using an inverted epifluorescence microscope (Olympus, IX-71), with a thermoelectrically cooled charge-coupled device (CCD) camera (Hamamatsu Co., Japan). Sequences of images were analyzed by ImageJ (NIH, Bethesda, MD, USA).

The hydrodynamic pressure is generated by a syringe pump (Harvard apparatus, PHD 2200), resulting 10μL/min of 10mM NaCl solution for all experiments. The corresponding average flow velocity is V~0.83 mm/s and Reynolds number using a hydraulic diameter D_H is Re_{DH}=0.28 ($Re_{DH} = VD_H/v$, $D_H = 4A/P$, where the area of the channel A, the wetted perimeter P, the kinematic viscosity of water $v=10^{-6}$ m^2/sec, respectively), which are smaller but on same laminar flow regime with large scale ED systems (Re=0.1~100)[15-17]. A benchtop conductivity meter(VWR sympHony conductivity meter, VWR International, LLC, Atlanta, GA) connected to a flow-through conductivity microelectrode (Microelectrode, Inc, Bedford, NH), can be directly mounted at the end of the desalted channel or the concentrated channel. It takes only about ten seconds for the desalted or the concentrated water in the cell to reach the conductivity meter, so the conductivity measurement tracks the changes in salt removal efficiency reasonably well. The measured conductivity is converted to salt concentration later (a detailed discussion is in Section 2.2.2). Through the inserted electrodes and the electric wires, constant voltage is applied and corresponding current is measured by Keithley 236 current-voltage source measurement unit (Keithley Instruments, Inc., Cleveland, OH). Operation voltage is between 0V to 100V. The contact resistance between the electrode and the electric wire is less than 0.2Ω, which is negligible compared to the overall electric resistance of ED system.

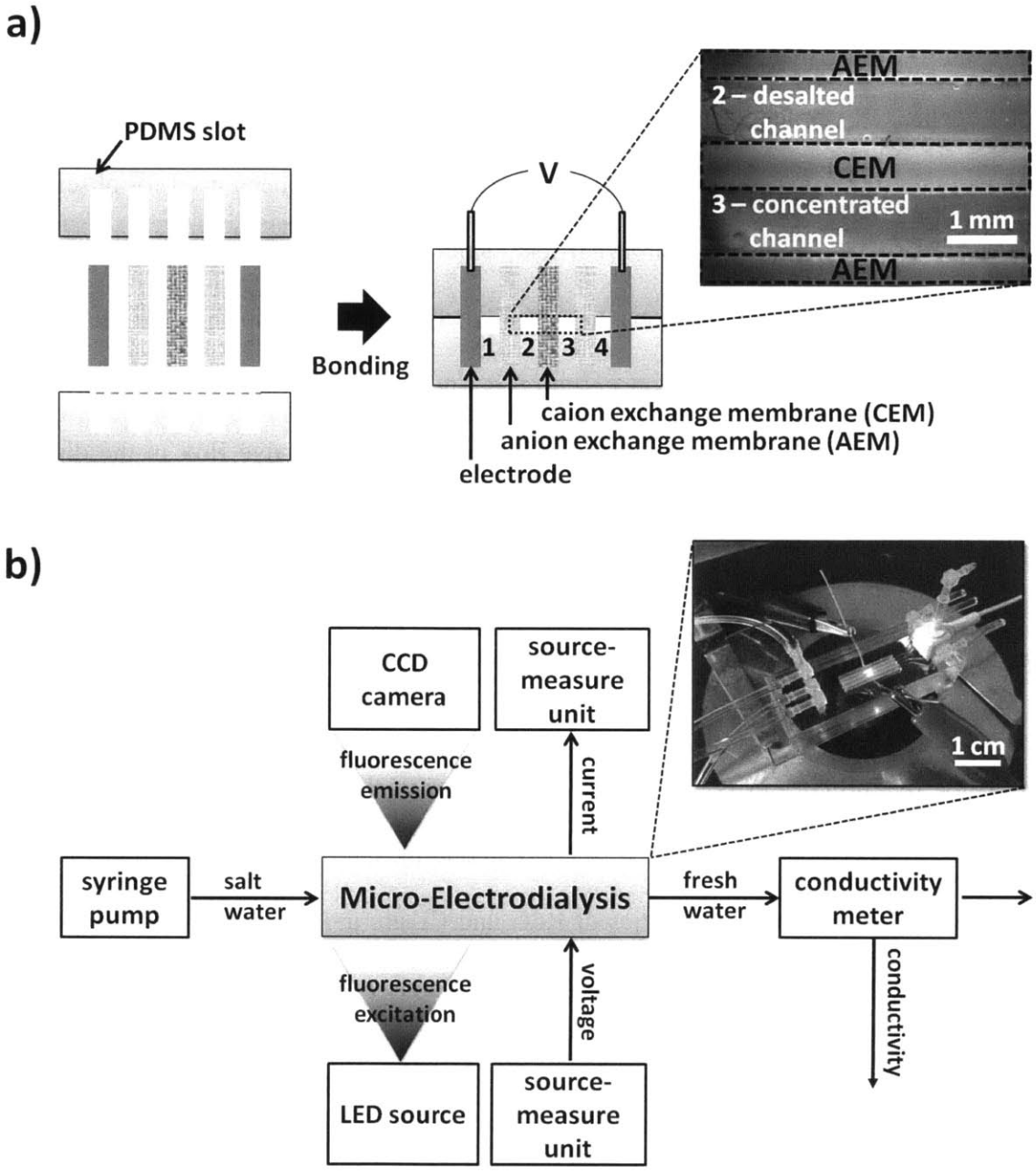

Figure 2.1 a) Schematic diagram of microscale electrodiaysis system before (left) and after assembly (right). This ED model system consists of two PDMS blocks, two AEMs, one CEM, and two electrodes. As a result, 4 microchannels are built: desalted and concentrated channel (2 and 3) and electrode channels (1 and 4). Inset figure shows the microscopic fluorescence image of the desalted and concentrated channels. The depth of PDMS slots is 3 mm and the widths are 0.38 mm for the CEM, 0.48 mm for the AEM, and 0.4 mm for the electrodes. The slot length is 20 mm, but the exposed area to the channels is 15 mm. The geometry of the channels is therefore 200μm in height, 1mm in width, and 15 mm in length. The IEMs and the electrodes are cut in 6mm x 20 mm. **b)** Schematic figure of micro ED operating platform and optical image (right and upper). 10mM NaCl solution with 10μM R6G flows into the four channels by the syringe pumps, and the conductivity meter measures conductivities of output fluids. The voltage source / current measurement apply constant voltages in the ED system and measure currents simultaneously.

2.2.2. Flow Visualization and Concentration Profiling

To visualize fluid flow and salt concentration, 10μM Rhodamine 6G (R6G) (Molecular Probes, Eugene, OR) is added in 10mM NaCl solution. Along with anionic fluorescence dyes (*e.g.* Alexa Fluor 488), this cationic fluorescence dye has previously been used for observing ICP near IEMs[18-20]. As minority charge carriers, R6G can trace salt concentrations in buffer solutions as long as the two conditions are satisfied; **i)**the concentration profile reach a steady state (no temporal changes), **ii)**dye concentration is low enough, so that dye molecules does not contribute to current flows significantly[21]. Then, conservation of dye flux in the direction of the field should render the dye concentration to be inversely proportional to the local electric field, and proportional to the local (majority) ion concentration. In our experiments, 10μM R6G is used in 10mM NaCl and the minimum concentration of NaCl achieved in the cell is about ~1mM (99.16μS/cm (0.799mM) at 100V in Fig. 2.2b and Fig. 2.3a). The contribution of each ion species to the overall current is proportional to the electrical mobility and their concentrations. R6G's contribution is then only 0.02~0.2 % compared to the chlorine ions (Cl^-) ($\mu_{R6G}C_{R6G}/\ \mu_{Cl}C_{Cl}$ ~ 10^{-4} or less), with electrical mobilities of R6G and Cl^- are $\mu_{R6G}=16.2\times10^{-9}$ and $\mu_{Cl}=79.1\times10^{-9}$ m^2/Vs respectively [21]. In addition, at least in the Ohmic / limiting regime, the condition for concentration steady state is satisfied: the electric noise is less than ~1% and the significant fluctuation of concentration profile was not observed (Fig. 2.2). The florescence intensity is linearly proportional to the R6G concentration when its concentration is less than 300μM [22]. The fluorescence signal intensity of R6G is also pH-independent between the pH value of 2 and 10 [23, 24]. Therefore, one can use the fluorescence signal of R6G as an indicator for local ion concentration in the cell, in Ohmic and limiting regime. Clearly, situations in overlimiting regime, with the development of dynamic vortices (Fig. 2.2c), the steady state condition is not satisfied[10, 12, 14]. Even then, dynamic changes in dye distribution can be used to identify

regions affected by fast fluid vortices generated in the overlimiting regime, which were shown to correlate well with flow patterns in previous experiments using microparticle tracking technique[25-27]. To obtain salt concentration profile in micro ED system, first, the fluorescence intensity is measured under various voltages at six points: 0, 1, 3, 6, 15mm away from the inlet along the channel, and at the outlet (Fig. 2.4 and Fig. 2.5). The relation between salt concentration and the fluorescence intensity is then calculated by comparing the average fluorescence intensity at the outlet and the measured conductivity in the desalted flow. Fig. 2.3 shows the conversion plot and equations of conductivity-salt concentration and fluorescence intensity-salt concentration. For the desalted flow, the measured conductivity corresponds to the average leveled fluorescence intensity calculated from Fig. 2.5. The converting equations are

$$\text{conductivity } (\mu S/cm) = 130 \times \text{salt concentration (mM)} - 4.7, \tag{2.1}$$

$$\text{fluorescence intensity (A.U)} = 165.2 \times \text{salt concentration (mM)} + 761.9. \tag{2.2}$$

Approximately, the fluorescence intensity 1000 is converted to 1 mM, 1500 to 4 mM, 2000 to 7 mM, 2500 to 10 mM, 3000 to 13 mM, and 3500 to 16 mM.

When unstable vortices appear near IEMs, the fluorescence intensity fluctuates due to repeated growing and shrinking of the depletion zone. Instead of averaging over this temporal fluctuation of the concentration profile, the intensity profile of the maximum depletion zone was measured and plotted, which corresponds to the faster ion transport (a detailed discussion is in Section 2.3.4). We did not have any surface treatment for preventing non-specific binding of R6G, because additional surface treatment might affect to the performance of the membranes. Any signal from non-specific binding of dyes was properly calibrated by subtracting background

fluorescence signal (0 V) from measured values.

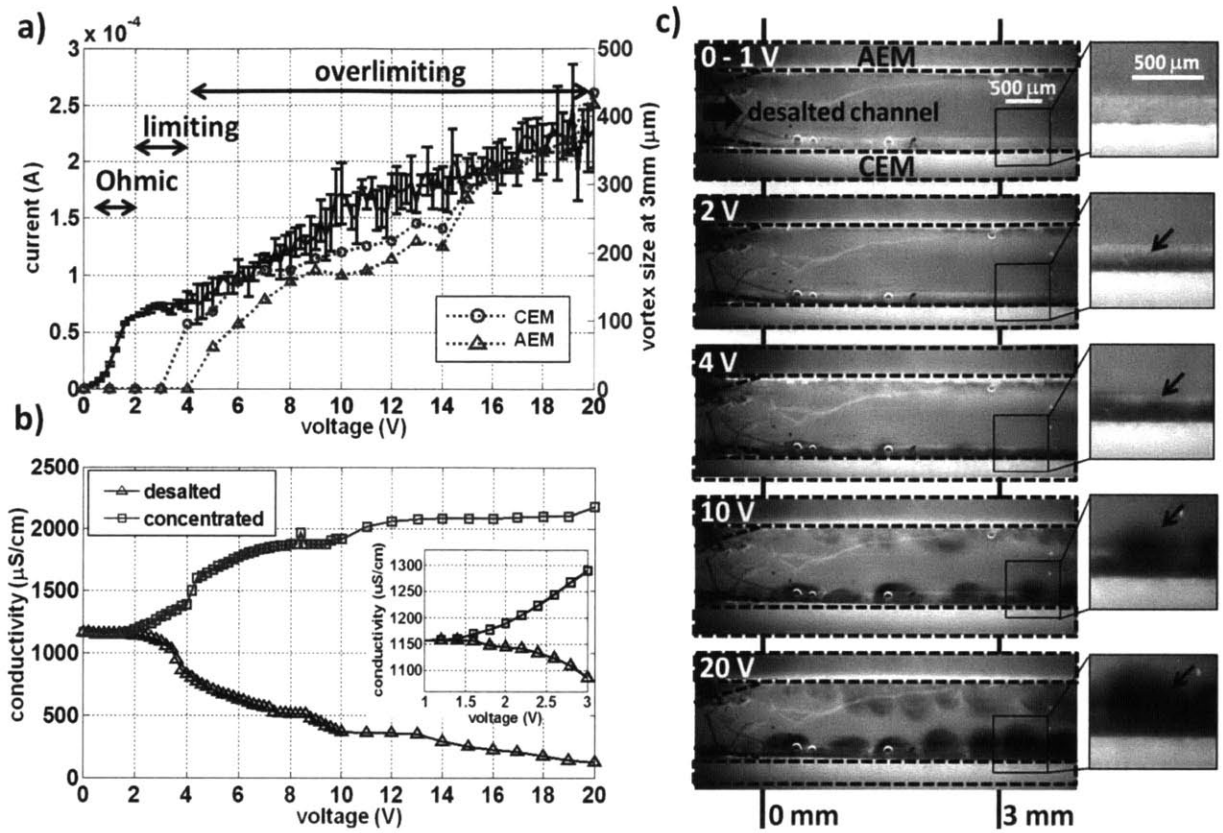

Figure 2.2. Variations in the current response and fluid dynamics with corresponding conductivity changes in the desalted and the concentrated flow. **a)** The current-voltage curve (solid line with error bars) and the size of the vortex near CEM (dotted line with circles) and AEM (dotted line with triangles) at 3 mm from the inlet (the second line in Fig. 2.2c). Effective electrode area is 0.2 mm×15 mm. Current-voltage response is measured by ramping up the voltage by discrete voltage jumps of 0.2V in every 30sec, which was repeated five times. The vortex size is measured in every 1V, when its size reaches the maximum during the fluctuation if any. The current is categorized by three regimes: Ohmic (0-2V), limiting (2-4V), and overlimiting (4-20V). At the range from 0 to ~1V, negligible Faradaic current occurs because of the reaction overpotential[28, 29]. **b)** The conductivity change of the desalted flow (solid line with triangles) and the concentrated flow (solid line with rectangular) from 0 V to 20 V, categorized into three current regimes. An enlarged plot between 1 and 3 V is also inserted. The conversion relation between the conductivity and salt concentration is presented in the Fig. 2.3a. The conductivity is measured in every 0.2 V before 10 V, and in every 1 V after 10 V. **c)** Visualized fluid flows and concentration profiles by R6G at the front part of the desalted channel at 0, 2, 4, 10, 20V. Magnified images for the interface of CEM and the electrolyte are also shown. The boundary layers (arrow at 2V), their perturbation (arrow at 4V), and the depletion zone by strong vortices (arrows at 10 and 20 V) are clearly observed. In addition, the circular depletion regions affected by vortices near AEM are clearly visualized as well. 10mM NaCl solution flows from left to right with the flow rate of 10μL/min. Two red lines indicate 0 and 3 mm from the inlet, respectively. Visualized images for overall channel is available in Fig. 2.4.

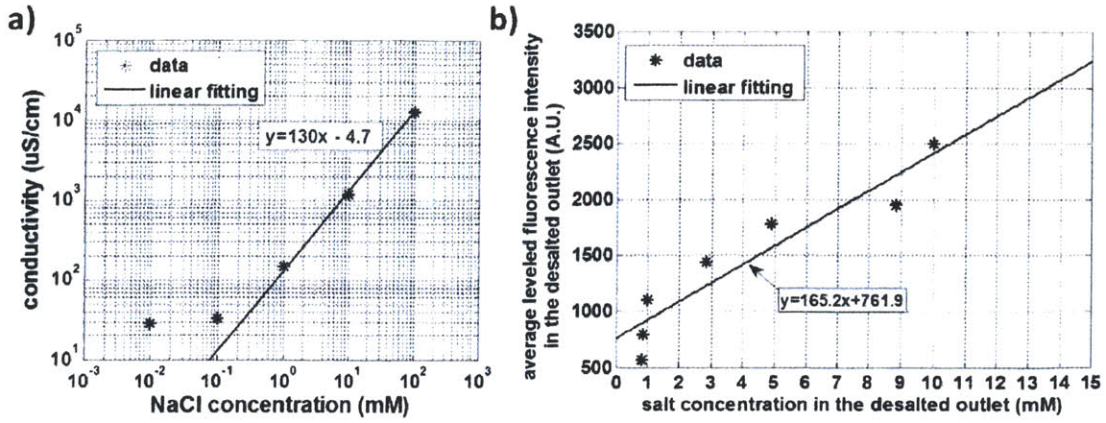

Figure 2.3. **a)** Conversion plots between conductivity (measured by in line conductivity measurement tool) and salt concentration. We measure the conductivity five times for 0.01, 0.1, 1, 10, and 100 mM NaCl solutions. Standard deviations for all solutions are less than 1%. Although the conductivity is linearly proportional to NaCl concentration, the conductivity measurement is not reliably below 1mM NaCl concentration. **b)** Conversion plots between calibrated R6G fluorescence intensity and salt concentration.

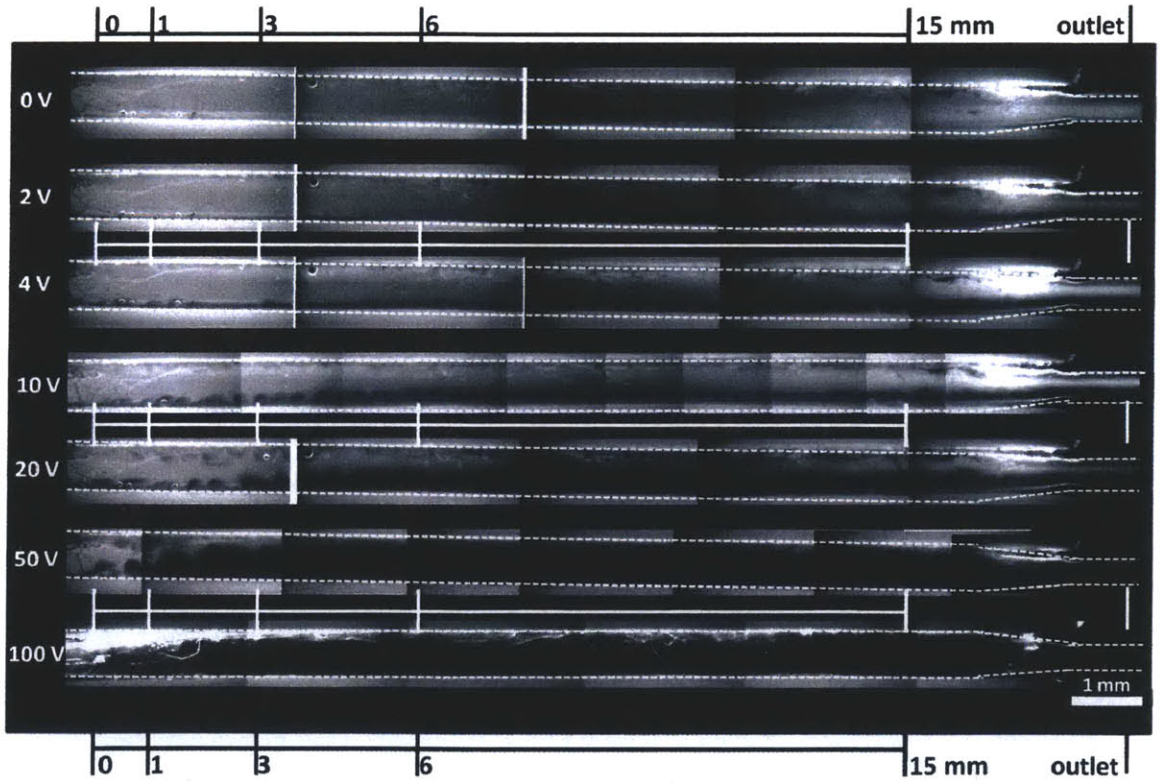

Figure 2.4. Combined images of desalted channels at various applied voltage (0, 2, 4, 10, 20, 50, and 100 V). The total length is 15 mm, and the width is 1 mm. The vortex size was measured at 3 mm, and the fluorescence intensity was measured (for local salt concentration profiles) at six points: 0, 1, 3, 6, 15 mm from the inlet, and at the outlet. Vortex growth with the voltage increase, and along the channel, is visualized.

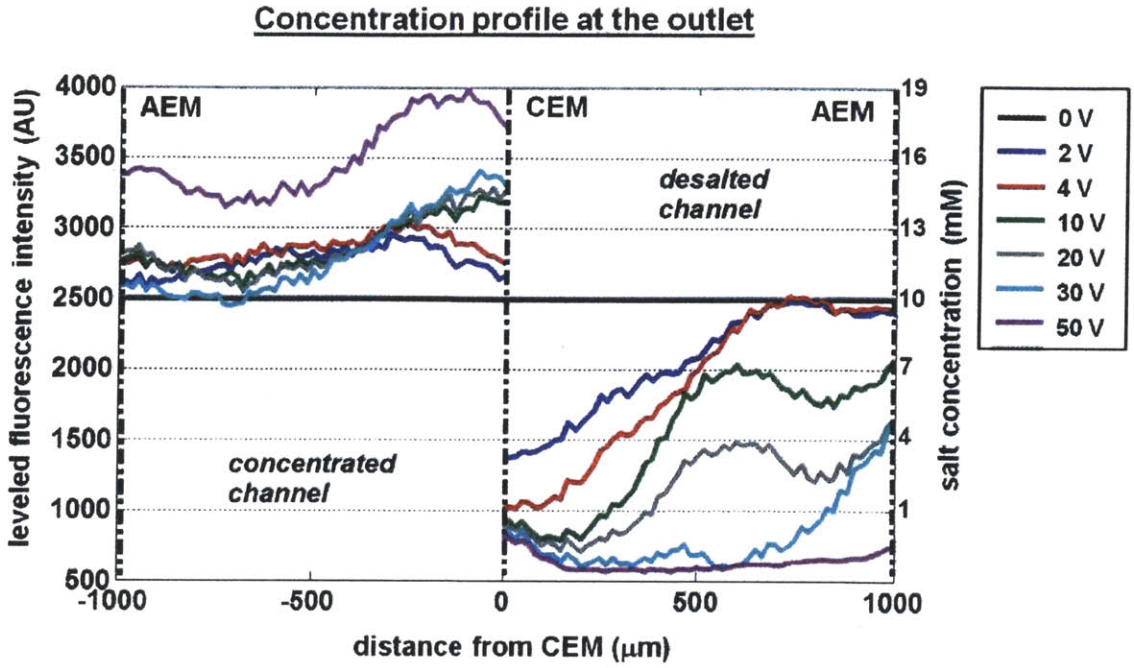

Figure 2.5. Calibrated fluorescence intensity at the outlet under various voltages: 0, 2, 4, 10, 20, 30, and 50 V. x-axis indicates the distance from CEM, whereas y-axis indicates the fluorescence intensity and corresponding salt concentration. At the outlet, there is no electric field and solid-liquid interfaces. For the desalted flow, the depletion of fluorescence dyes is well visualized, but it is stronger near CEM. It is presumably due to the higher permselectivity and conductivity of CEM.

2.3. Changing Dynamics Affect Ion Transport

2.3.1. Three Current Regimes and Flow Vortex Dynamics on IEMs

Fig. 2.2 shows the visualized micro ED system with current and conductivity measurements according to the applied voltage from 0 to 20V. In the current-voltage curve, three regimes can be distinguishable: Ohmic, limiting, and overlimiting regimes (Fig. 2.2a). These three regimes have been theoretically predicted[10] and observed in the current-voltage curves of single AEM or single CEM[16]. In this ED platform, each regime shows distinct flow pattern, concentration profile, and salt removal performance (Fig. 2.2b-c). The observed behaviors are clearly different from the prediction of the conventional theory of concentration polarization[30], where the ion depletion and enrichment behavior around ion exchange membrane (IEM) is explained by the coupled drift-diffusion (Fig. 2.6a). In this model, the concentration profile becomes linear, within a boundary layer often called as 'diffusion boundary layer'. Ions are transported mainly by diffusion/drift, while the convection is dominant only outside the diffusion boundary layer, where the ion concentrations return to those of bulk solutions. The thickness of diffusion boundary layer, which critically determines the overall ion transport efficiency, is largely determined by (mixing) fluid flow in the bulk solution. In contrast to this conventional model, as observed in our experiment, the (apparent) boundary layer thickness systematically depends on the applied voltage, even when the external flow conditions (tangential flow) remain the same. The concentration profiles within the boundary layer are not linear, and there is a clearly defined flat (although low) concentration region (Fig. 2.6b). Here, this region is termed as (ion) depletion zone[25, 31, 32], which is different from the 'diffusion layer', often referred in earlier literatures[12, 30]. In addition, complex (vortex-driven) structures of this depletion zone are observed. The observed behaviors are largely in line with the model proposed by Rubinstein and Zaltzman[10], where a non-linear electrokinetic fluid slip is considered to generate strong

vortices and efficient mixing within the boundary layer. Strong vortices were later shown to generate a region with almost a flat concentration, outside of the extended space charge layer (ESC) near the membrane surface[26]. In the depletion zone, ions are depleted down to ~1/100 of original concentration[8, 33], but the main ion transport mechanism within this zone is convection by strong vortices, not diffusion (there is no concentration gradient)[34, 35]. Fig. 2.7 and Fig. 2.8 show the gradual changes in concentration profile at different operation voltages and at different locations of the channel. As can be seen in the Fig. 2.7, the generation and expansion of concentration polarization region (and depletion zone) near AEM and CEM, as well as vortex generation, are well observed. In this experiment, we do not consider the thickness of electric double layer (EDL) and extended space charge layer (ESC) because these are negligible (<< 1μm).

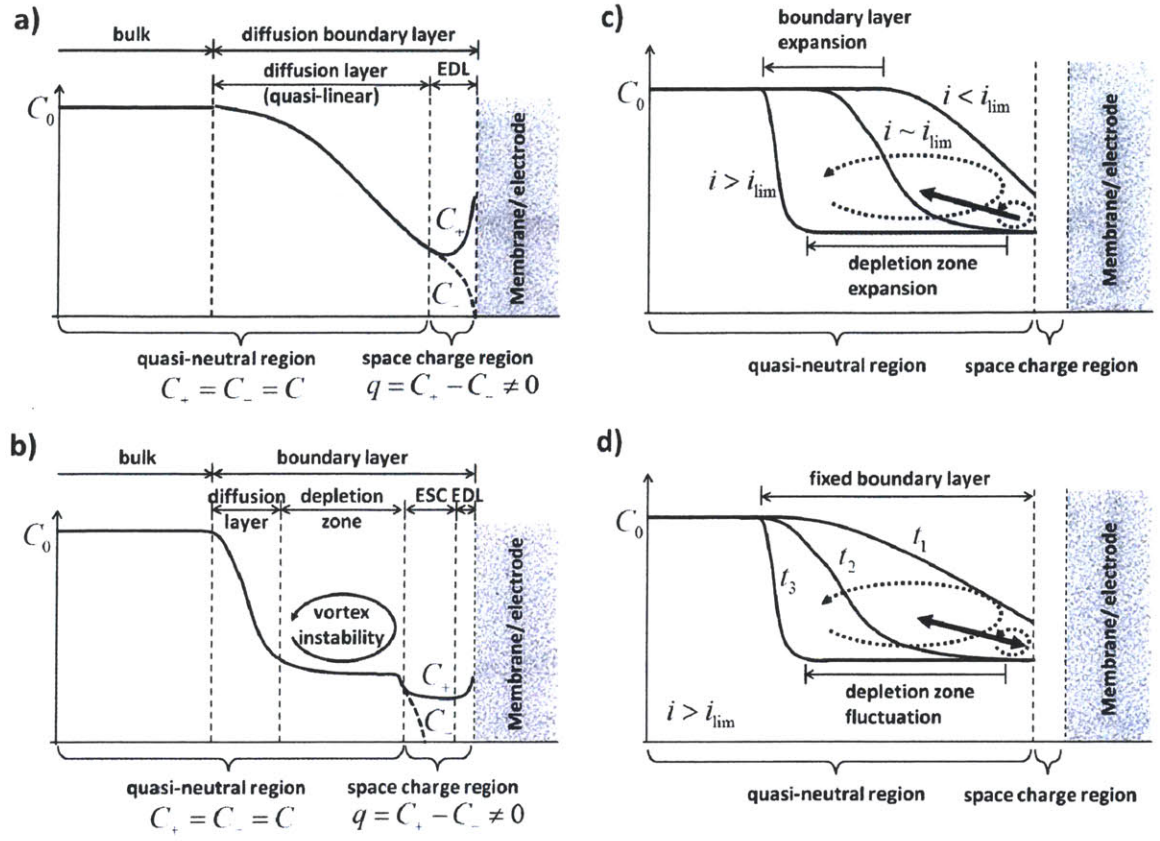

Figure 2.6 a) Structure of diffusion boundary layer, based on conventional model of ICP[30], **b)** Structure of boundary layer caused by ICP, as observed in our and other's work[10, 26, 34] **c)** Change of modified concentration profiles for three different current regimes: Ohmic ($i<i_{lim}$), limiting ($i\sim i_{lim}$), and overlimiting ($i > i_{lim}$), and **d)** Concentration fluctuation by unstable vortices in overlimiting regime ($i > i_{lim}$) (not in real scale). C_0, C_+, and C_- indicate the concentration of bulk, counterion (solid line), and coion (dotted line), respectively. Dotted circular lines indicate the vortices, and thick lines indicate the direction of vortex evolution according to voltage or current increase (Fig. 2.6c), and according to time (Fig. 2.6d), respectively.

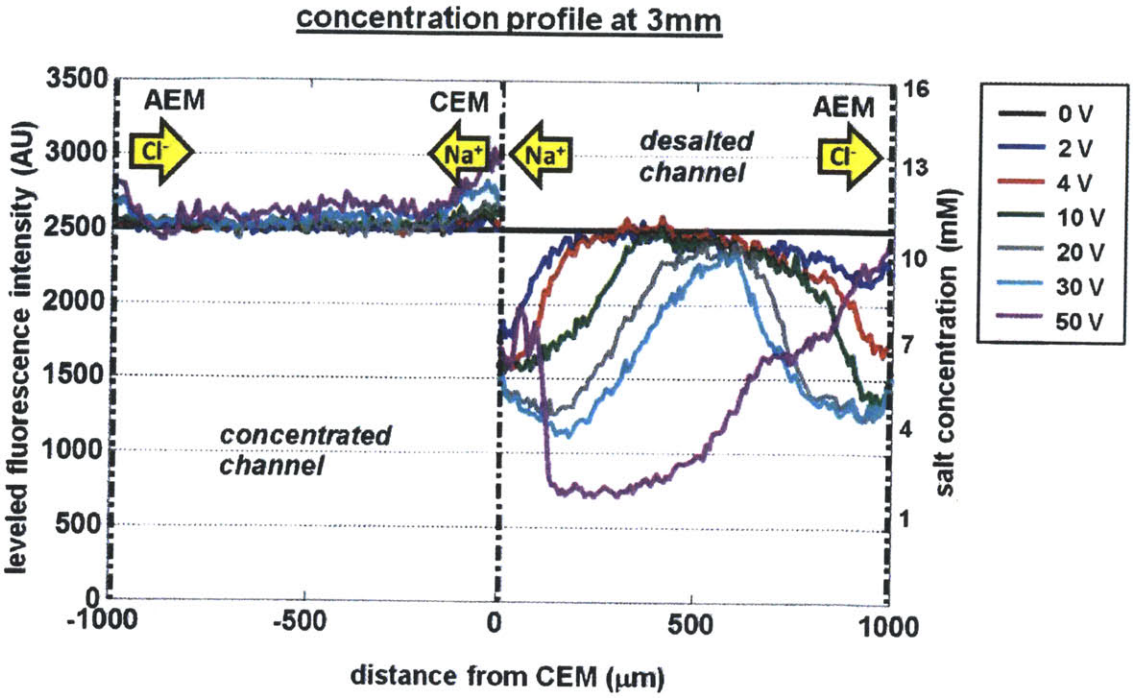

Figure 2.7 Calibrated fluorescence intensity at 3mm from the inlet under various voltages: 0, 2, 4, 10, 20, 30, and 50V. x-axis indicates the distance from CEM, whereas y-axis indicates the fluorescence intensity (corresponding to the local salt concentration). Fluorescence intensity near IEMs is increased slightly in the desalted channel, which is probably due to the adsorption of R6G into IEMs and the strong autofluorescence of IEMs. Depletion region and sharp diffusion layer are clearly observed at high voltage conditions.

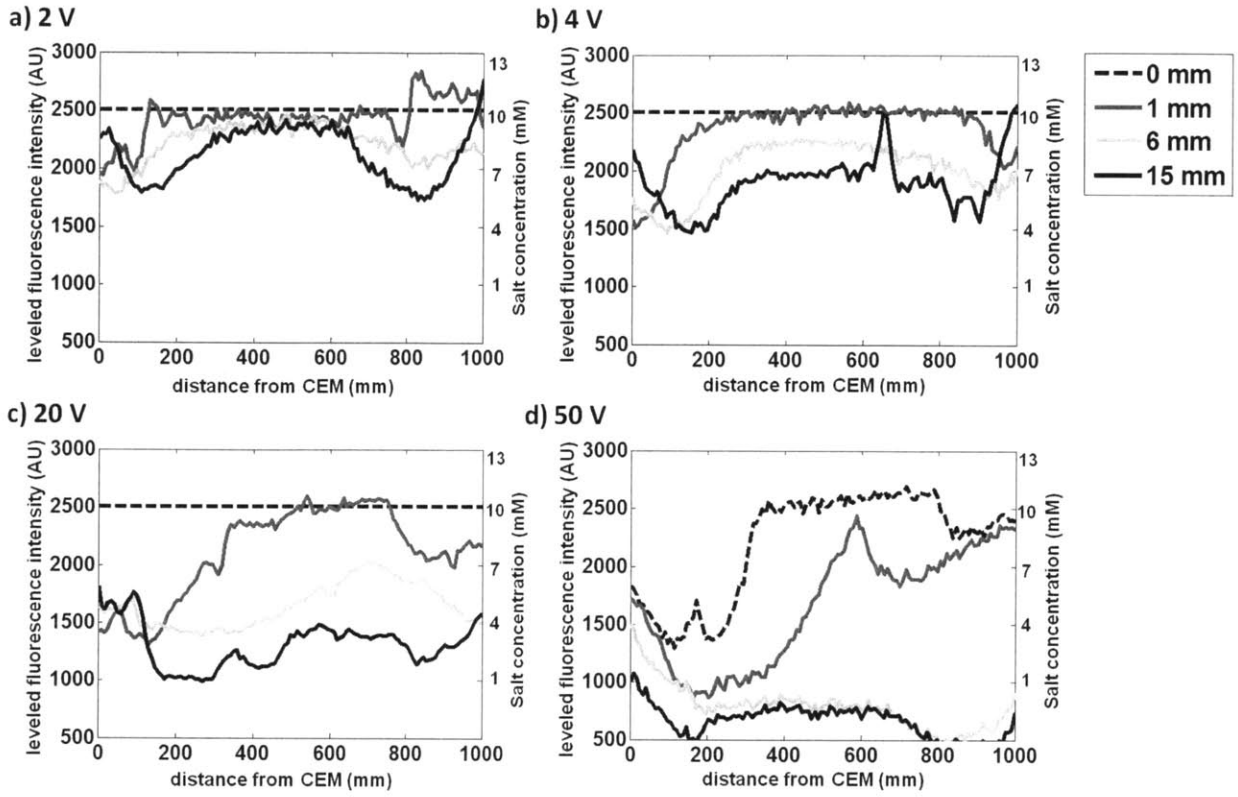

Figure 2.8 Calibrated fluorescence intensity in the desalted flow under various voltages(2, 4, 20, and 50 V) and points (0, 1 , 6, and 15 mm). x-axis indicates the distance from CEM, whereas y-axis indicates the fluorescence intensity and corresponding salt concentration. CEM and AEM are separated by 1mm. Fluorescence intensity near IEMs increases slightly in the desalted channel, which is probably due to the adsorption of R6G into IEMs and the strong autofluorescence of IEMs.

2.3.2. Ohmic Regime

First, in the Ohmic regime (V< 2V), the current linearly increases with the voltage, indicating a near-constant overall cell resistance, and then it begins to saturate by the formation of diffusion layer (0-2V in Fig. 2.2a). The near-zero current at V < 1V is due to reaction overpotential. In this regime, the diffusion (coupled with drift) is a dominant mechanism of ion transport. One can observe linear diffusion boundary layers formed near the membranes (Fig. 2.2c at 2V). Only linear diffusion layer appears near AEM and CEM (Fig. 2.6c at $i<i_{lim}$ and Fig. 2.7 at 2V). This diffusion layer is growing along the channel (Fig. 2.8a and Fig. 2.4). As the width of diffusion boundary layer (or diffusion layer) is increased at the downstream locations of the desalted

channel, the concentration gradient becomes smaller, which indicates slower ion transport at those locations. That is, a majority of system current passes through the front part of the channel, which was also experimentally observed by V.A. Shaposhink *et al.*[13].

For electrodialysis process, operating voltages are typically set at the upper end of the Ohmic regime (~2V in this experiment)[36, 37]. This is because of a dramatic jump of the electric resistance in the limiting current regime. However, the ion transport by diffusion is inefficient, demonstrated by rather small conductivity drop in the output (0-2 V in Fig. 2.2b).

2.3.3. Limiting Current Regime

As the voltage increases, the current-voltage curve saturates to a current plateau, by the diffusion limitation of ionic transport (2-4 V in Fig. 2.2a). In this limiting current regime, in the desalted channel, salt concentration is reduced to the lowest value near the interface of the IEMs and the electrolyte, and then formation of a depletion zone with flat (low) ion concentration occurs. The depletion zone, which has the lowest salt concentration, then expands with increased voltage (Fig. 2.2c at 4 V). Initially, at 2~3V, these depletion zones near IEMs are relatively stable, but they begin to fluctuate by electro-osmotic instability (EOI) at IEMs with high voltage or current[10]. This instability is due to the development of ESC next to classical EDL, which indicates the concentration plateau of counterion concentration by perfect repulsion of coion, resulting in strong flow vortices (Fig. 2.6b).

In the limiting regime ($2V < V < 4V$), the depletion zone begins to appear (Fig. 2.6c at $i \sim i_{lim}$ and Fig. 2.7 at 4V). Initially, near ~2V, vortices are not clearly visualized because of their small sizes, but one can confirm the existence of vortices in the depletion zone and fluctuation of the boundary layer. At the end of this regime, at 4V, both fluctuation of the boundary layer and vortices are visualized clearly (Fig. 2.4). As can be seen in the Fig. 2.7 at 4V and Fig. 2.8b, both

vortices and depletion zone expands, while the diffusion layer (region with concentration gradient, outside of depletion region in Fig. 2.6b) grows only slightly along the channel. This expansion is probably due to the vortex evolution time. It requires a few seconds for complete vortex evolution from the initial disturbance[10]. Interestingly, under constant flow rate in this system, the temporal process of vortex evolution is effectively 'visualized' at different points along the channel. This vortex evolution becomes faster at higher voltage (Fig. 2.9). The detailed description of this vortex would require careful modeling of many factors, such as current distribution, changes in membrane permselectivity, and continuous decrease/increase in ion concentration along the channel.

It is noted that the slope of the diffusion layer are still sharp at 15mm from the inlet of the channel (Fig. 2.8b at 4 V). This indicates that the ion and current flux are still maintained even at 15mm downstream the channel, and therefore utilizing that part of the channel for removal of the ions. In other words, the vortices by EOI near IEMs bring about dramatic enhancement of salt removal performance (Fig. 2.2b at ~4 V); which shows electroconvection by EOI boosts salt ion transport through IEMs, by generating overlimiting conductance in electrodialysis (ED).

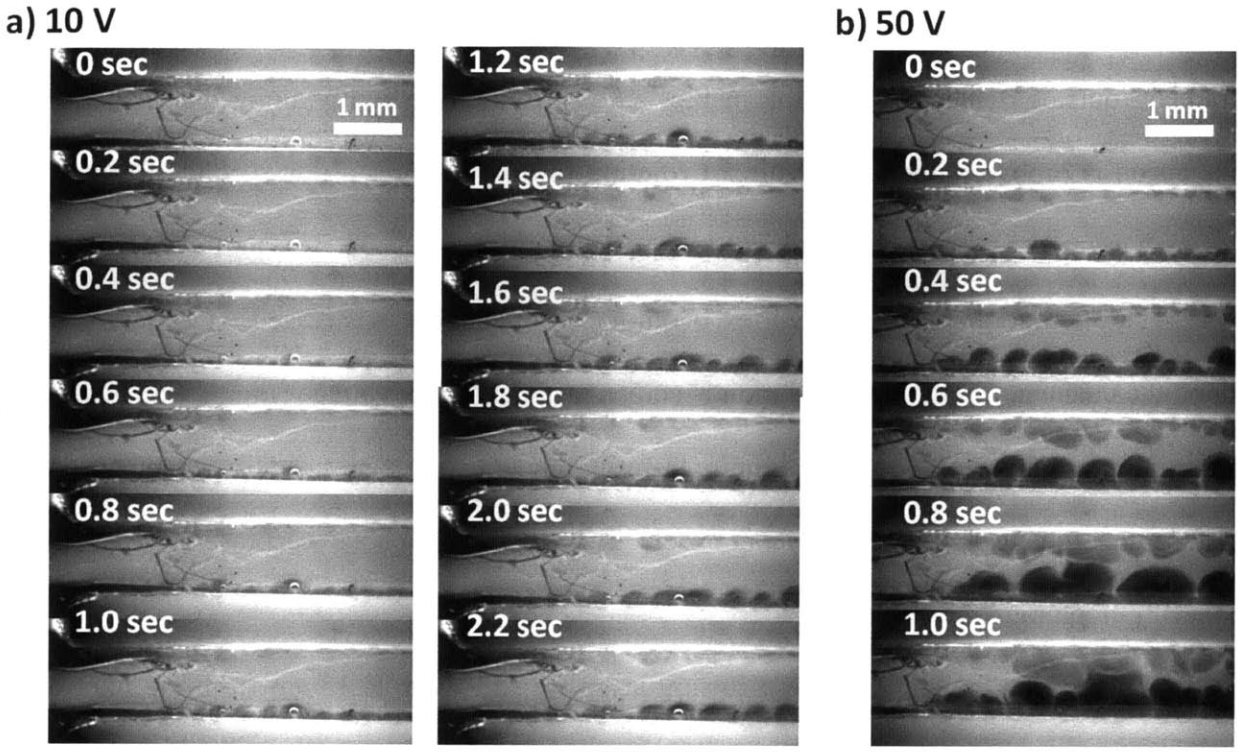

Figure 2.9 The vortex evolution at 10V and 50V is shown at different time points (0 - 3 mm from the inlet). The complete expansion of vortices occurs 2.2sec at 10V and 1.0 sec at 50 V. The higher voltage, the faster evolution of vortices becomes. This is also related to the faster saturation of current at higher voltage (Fig. 2.10).

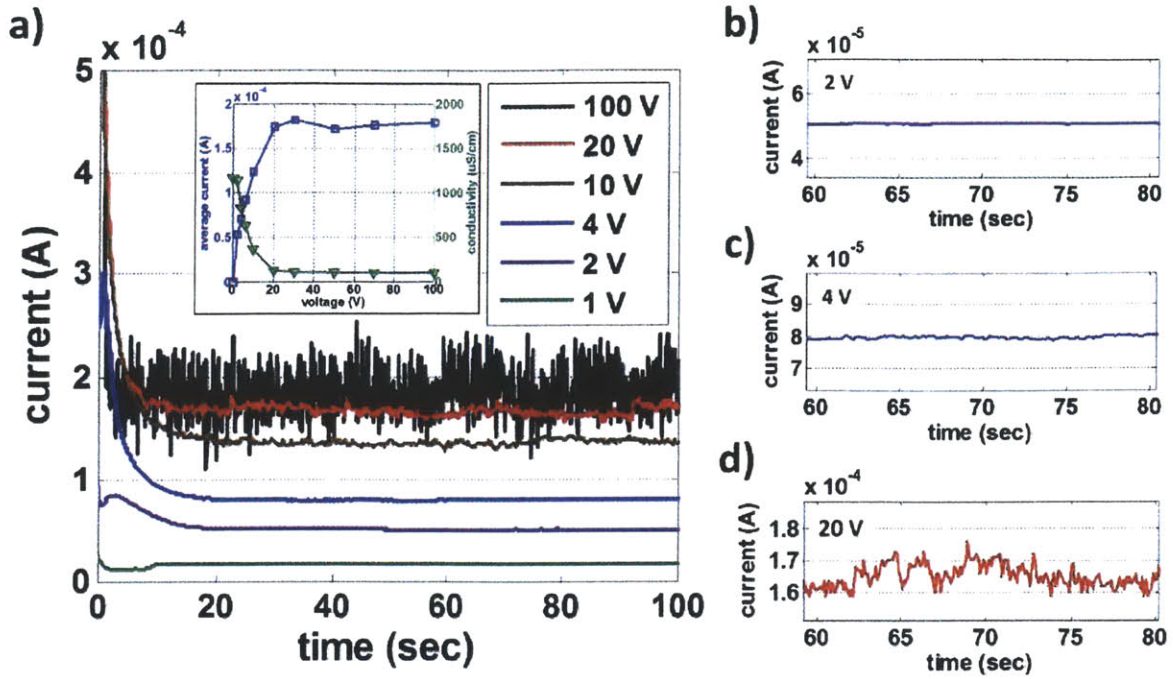

Figure 2.10 a) Time evolution of the current from 1V to 100V and **b-d)** Magnified figures at 60~80 sec in different current regimes: **b)** Ohmic (2V), **c)** Limiting (4V), **d)** Overlimiting (20V). Stable current is observed in Ohmic regime, but the current begin to oscillate starting from the onset of the overlimiting regime. The current shows chaotic oscillation in overlimiting regime. Magnified images from 1V to 100V for 8 different voltages (1, 2, 4, 6, 10, 20, 50, and 100 V) are also available (Fig. 2.12). The current is measured during 100sec in every 0.1 sec right after the voltage applying. The inset image shows the average current and the conductivity in the desalted flow up to 100 V. The average current is calculated by averaging currents from 30 to 100sec.

2.3.4. Overlimiting Current Regime

As the voltage increases, in the overlimiting regime (V > 4V), both depletion zone and overall boundary layer become thicker (Fig. 2.6c at $i>i_{lim}$ and Fig. 2.7 at 10-30V). As the depletion zone (affected by fluidic vortices) expands, the layer outside of the depletion zone should accommodate higher concentration gradient, and therefore higher ion transport flux; this is caused the vortices become not only larger, but faster[34] (Fig. 2.6c and Fig. 2.11a). Further along the channel, two boundary layers originating from AEM and CEM begin to meet in the finite channel width (Fig. 2.2c and Fig. 2.7 at 20 V). Above 20 V, vortices from AEM and CEM span almost the entire channel width, resulting in a narrow, undesalted region in the middle of

the channel (Fig. 2.7 30V and Fig. 2.8d 50V at 1mm). As vortices expand at the further downstream locations, however, the stronger vortices from CEM overwhelm the relatively weaker vortices from AEM, blurring the edges of the two boundary layers (Fig. 2.8c 20V at 6 mm and Fig. 2.8d 50 V at 3 mm). The asymmetry of vortices from AEM and CEM is due to two reasons: the different transport properties and the different Stokes radius of sodium and chlorine ions. First, the limiting current density by the transport of sodium ion (at CEM) and chlorine ion (at AEM) are not the same. From the Peers equation[12], the limiting current is inversely proportional to the difference of the effective transport number of counter-ion in the membrane and the transport number in solution (when other parameters, bulk concentration, electrolyte diffusivity, and the thickness of diffusion boundary layer, are fixed). Although the effective transport numbers of counter-ion are close to 1 for both AEM and CEM in dilute condition (10mM NaCl)[38], the transport numbers t of co-ions on CEM and AEM are different significantly, because t is linearly proportional to diffusivity D of co-ions[12]; as a result, the limiting current density at CEM (by sodium ion) is about 1.5 times lower than that at AEM (by chlorine ion)(D_{Cl^-}/D_{Na^+}=2.032/1.334). Therefore, as voltage increases, the current density reaches the limiting current density at CEM first, which also initiates vortices and overlimiting conductance first. This mismatching of the limiting current density also induces the non-zero slope of current-voltage curve in the limiting regime (Fig. 2.2a) and the asymmetry of concentration profiles (Fig. 2.7 and Fig. 2.8). Next, the Peclet number Pe is used for characterizing the contribution of convection with respect to diffusion. In the physicochemical hydrodynamic systems, the convection term in Pe can be replaced by electroconvection term, and this Peclet number is proportional to the Stokes radius of ion[39]. Therefore, ions which have larger Stokes radius d shows stronger electroconvection[40]. That is, the vortices at CEM is

stronger than the vortices at AEM (d_{Na+}=0.183 nm, d_{Cl-}=0.120 nm)(d_{Cl-} is calculated by multiplying d_{Na+}[40] and the ratio of diffusivity, D_{Na+}/D_{Cl-}=1.334/2.032[28] because the stokes radius d is inversely proportional to the diffusivity D).

This electroconvection pattern becomes a dominant transport mechanism when larger and stronger vortices are generated at higher voltages (4-20V in Fig. 2.2a-b). As the voltage increases, the flow vortices grow larger and more unstable. As seen in the Fig. 2.2c (10V and 20V), the circular depletion regions (created by vortices) repeatedly grow and shrink in size along the channel. Here, the thickness of overall boundary layer is fixed, whereas that of depletion zone fluctuates (caused by the fluctuation in vortex size); as a result, higher concentration gradient (and faster ion transport) occurs in diffusion layer when the vortex expands (Fig. 2.6d and Fig. 2.11b). Interestingly, because of this vortex fluctuation, the flow vortices seem to "migrate" along the channel. Although R6G in the solution cannot directly visualize the direction of these vortices, previous experimental and theoretical results suggest that one can expect paired vortices, one with clockwise rotation, and another counter-clockwise[10, 20, 25]. These new characteristics of vortices are discussed in Section 3. It is noted that, when the voltage is higher than 20V, the vortices from AEM and CEM overlap and interact with each other (Fig. 2.2c and Fig. 2.4), resulting in strongly chaotic current behavior (Fig. 2.10a).

The current-time curve also visualizes the dynamic system response, largely caused by vortex oscillation, in the ED system (Fig. 2.10). Time evolution of current shows steady state in Ohmic regime (1-2V), and chaotic oscillation in overlimiting regime (above 4V). Although the numerical model[10] and experiment[16] have revealed this shift, this is the first time when such dynamic behaviors were clearly visualized in a realistic ED system. In the Ohmic regime, any perturbation is suppressed by viscous damping, so the current becomes steady (Fig. 2.10b at

2V)[10, 12]. In the initial stage of the limiting regime, however, nonlinear vortices generate the fluctuation of currents (Fig. 2.10c at 4V). As these vortices become unstable, current oscillation also becomes chaotic (Fig. 2.10d at 20V). The higher the voltage, the greater becomes the current fluctuation amplitude (Fig. 2.10a). The transition of current behavior from periodic to chaotic oscillation is well visualized from the data (Fig. 2.12). This tendency can be clearly observed in current power spectrum by Fast Fourier Transform (FFT) (Fig. 2.13). Two jumps of the amplitude of random current fluctuation happen when **i)**vortices are visibly initiated in overlimiting regime (from 1-6V to 15-20V) and **ii)**vortices on CEM and AEM are overlapped (50V). It is noted that the average current after 20V shows the second plateau, and the salt removal efficiency in the output desalted stream saturates (inset graph in the Fig. 2.10a), which is discussed in Section 2.4.

Regarding the ion concentration profile in the overlimiting regime, V.I. Vasil'eva *et al.*[15] and V.V. Nikonenko *et al.*[12] previously argued that the thickness of diffusion layer should decrease at higher current ED processes. However, they have opposite claims about the thickness of boundary layer. V.I. Vasil'eva *et al.*[15] argued that the boundary layer thickness actually increases based on the interference-based measurement, but V.V. Nikonenko *et al.*[12] claimed that the thickness decreases for higher current flow based on the theoretical one-dimensional stationary model. This contradiction can be explained clearly by taking into account the depletion zone. According to our experimental result, the significant expansion of vortex instability induces the increased thickness of depletion zone (with flat concentration profile) and boundary layer, but the diffusion layer (outside of the depletion zone) shrinks at higher voltage (or higher current). At overlimiting current regime, it is noted that the stronger convection by vortices in depletion zone maintains the larger concentration gradient of the diffusion layer.

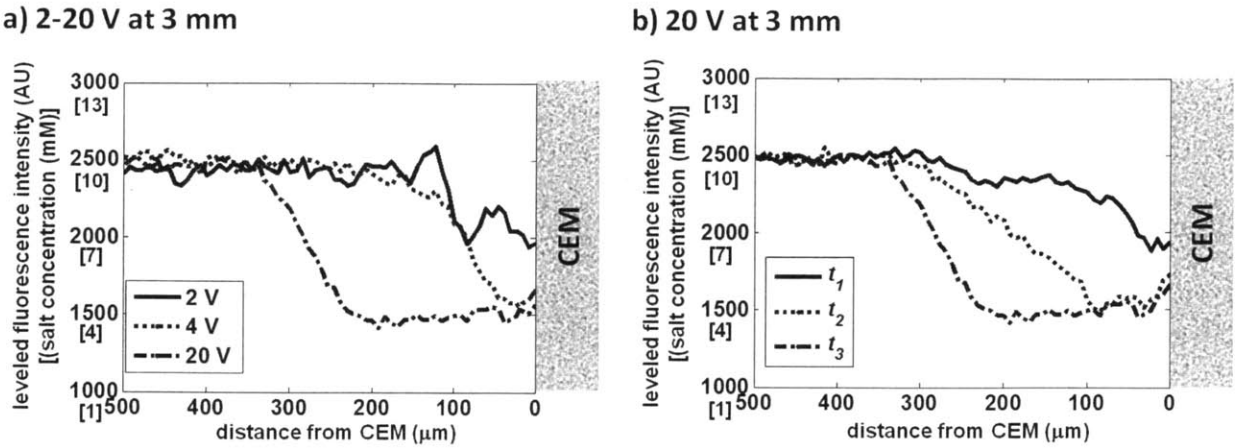

Figure 2.11 Calibrated fluorescence intensity near the CEM interface, showing the concentration profile **a)** at three different current regime (Ohmic: 2 V, limiting: 4 V, and overlimiting: 20 V) and **b)** three different arbitrary times (t_1, t_2,and t_3) at 3 mm from the inlet. x-axis indicates the distance from CEM, whereas y-axis indicates the fluorescence intensity and corresponding salt concentration. These profiles, Fig. 2.11a and b are matched with Fig. 2.6c and d, respectively.

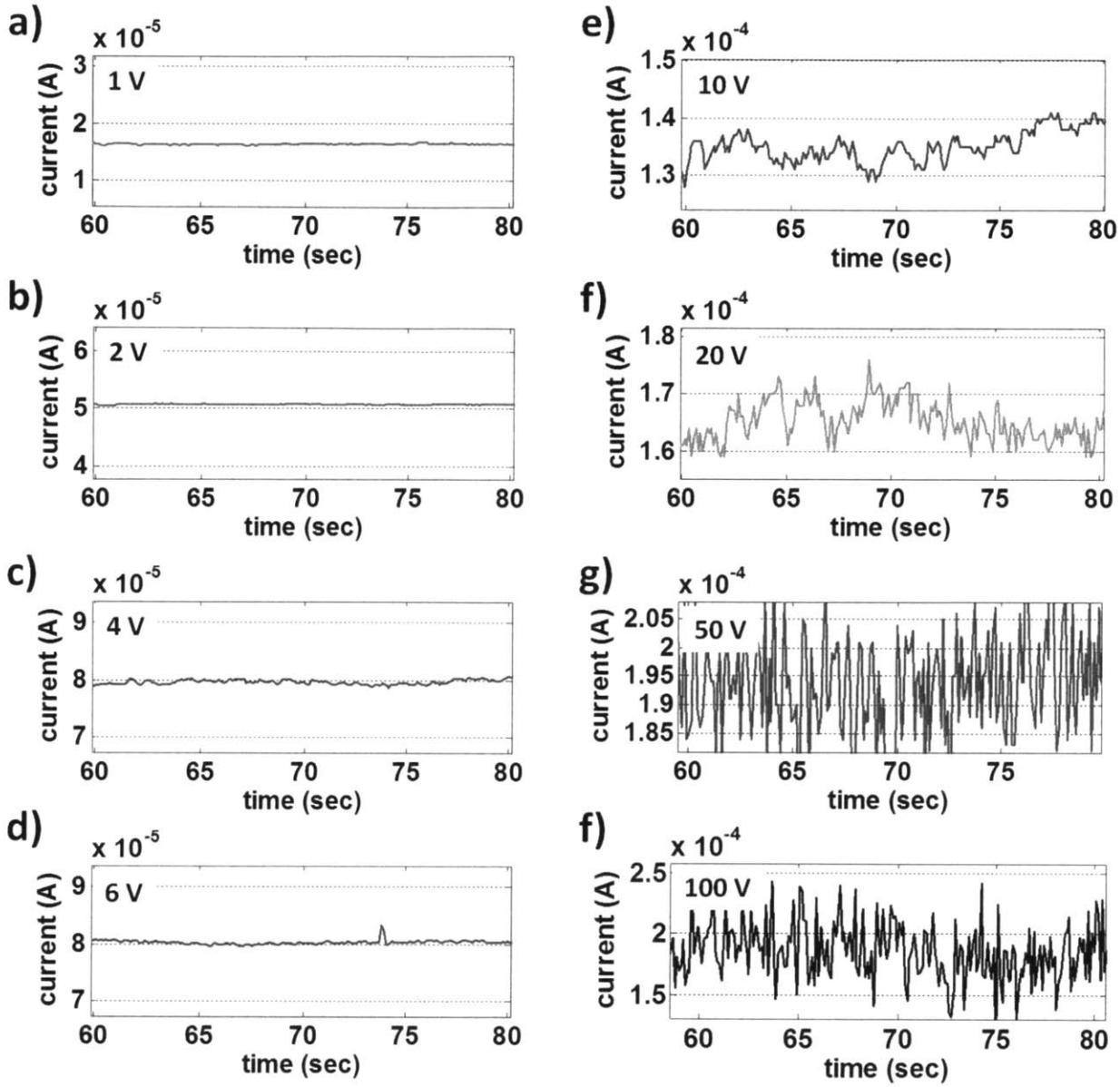

Figure 2.12 The magnified current-time curves of Fig. 2.10 at 60~80sec, from 1 V to 100 V. **a-b)** In the Ohmic regime, at 1-2 V, the current is stable. **c)** As vortex instability occurs, current fluctuation is observed at 4V, and **d-f)** this oscillation becomes increasingly chaotic. The standard deviation of current signal increases from 1V to 100V: 0.134 (1V), 0.331 (2V), 0.549 (4V), 0.511 (6V), 2.42 (10V), 4.81 (20V), 5.86 (30V), 9.40 (50V), 22.8 (100V) μA. The effective electrode area is 0.2 mm×15 mm.

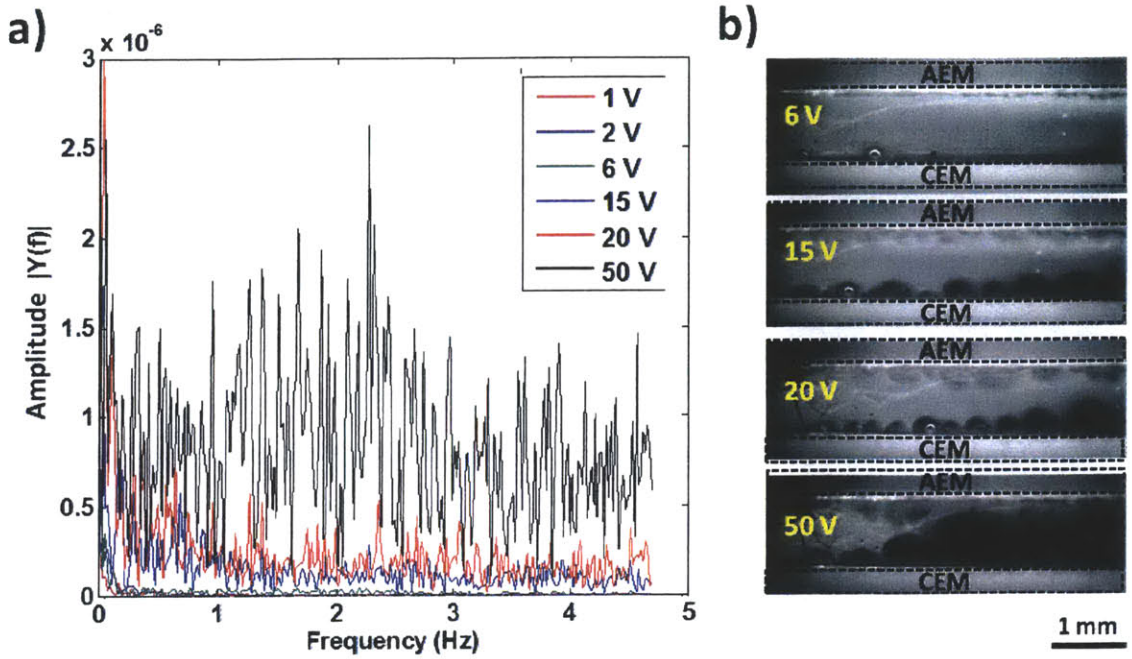

Figure 2.13 a) Current power spectrum by FFT and **b)** fluorescent images from 1 to 50V. The current-time data in Fig. 2.10 is used. Frequency regime is limited under 5 Hz because the current response are measured in 10 Hz (once in 0.1 sec).

2.4. Current Efficiency

Lastly, we discuss the efficiency of the micro ED system including intensive current regime. One of key parameters for optimizing ED system is current efficiency, which describes how effective salt ions can be separated by IEMs for a given applied current. This efficiency is calculated by

$$\text{current efficiency} = \frac{zFQ(C_{\text{Concentrated}} - C_{\text{Desalted}})}{2NI}, \tag{2.3}$$

where $C_{\text{Concentrated}}$ and C_{Desalted} are concentrated and desalted flow concentration (initial concentration: C_0=10 mM), respectively. z is the charge of ions (z=1 for sodium or chlorine ions), F is the Faraday constant (96,485 C/mol), Q is a flow rate (Q= 10 μL/min), N is the number of cell pairs (N=1), and I is the current[17]. Current efficiency also can be calculated only with the discrepancy between concentrated (or desalted) flow concentration and the initial concentration. While current efficiency has been measured frequently, according to various input parameters (*e.g.* flow rate, applied voltage or current, initial concentration), there has been no clear physical explanations about the trend of current efficiency yet [17].

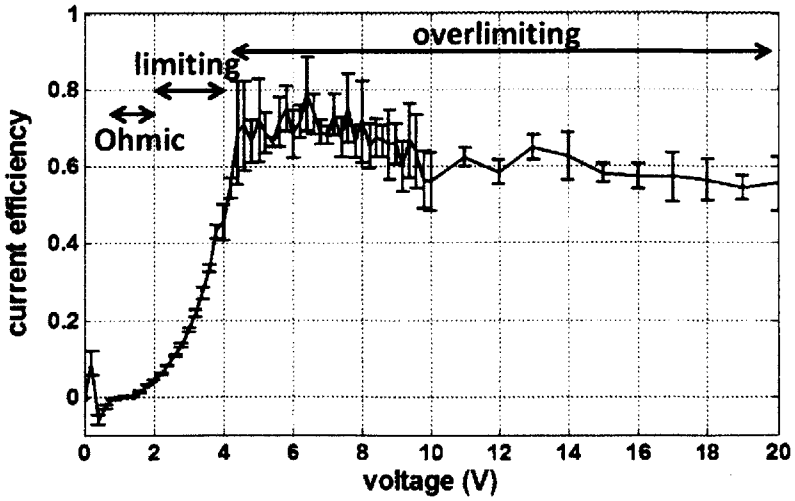

Figure 2.14 Current efficiency of the ED system as a function of operating voltage between 0 and 20V: Ohmic (0-2 V), limiting (2-4 V), overlimiting (4-20 V).

Fig. 2.14 shows calculated current efficiency by substituting measured currents and conductivities according to voltages. As higher voltage, current efficiency decreases in Ohmic regime due to higher current and constant cell resistance (*i.e.* very weak salt removal), whereas current efficiency increases in limiting regime, especially after the vortex instability occurs. At ~7 V, current efficiency begins to drop because the conductivity drop in desalted flow becomes gradual while the current increases (Fig. 2.2a-b). As a result, instead of the end of Ohmic regime, the maximum efficiency occurs at 4-8V, which is in the initial stage of the overlimiting regime. Herein, the unstable vortices form, resulting in the dramatic decrease of conductivity (Fig. 2.2a-b). At below 1.23V, Faradic current is negligible due to reaction overpotential. Somc amount of salts may be removed via capacitive charging (capacitive deionization (CDI) regime), and ideally current efficiency should be 1. In this experiment, however, the amount of removed salt by CDI is negligible (current efficiency≈0) because of the low surface-to-volume ratio of aluminum electrodes (Fig. 2.2b). In addition, current efficiency calculated in this regime is prone to a large error and perhaps not adequate for characterizing CDI efficiency in this system (Fig. 2.14). At higher voltage, over 7V, the salt removal performance is better, whereas current efficiency is lower because of high current. There are four possibilities to lower current efficiency: fluid leakage, current leakage, co-ion transfer, water splitting at high voltage. Symmetric conductivity variation of concentrated / desalted channel indicates that the fluid leakage between the channels is negligible (Fig. 2.2b). High permselectivity of AEM and CEM in a dilute condition (10mM NaCl) would prevent co-ion transfer through the membranes successfully; the permselectivity of IEMs are 96% (FTCM-E) and 90% (FTAM-E) in 0.1/0.5M KCl at 25°C, and this would be significantly enhanced by high apparent transport number as in dilute solution (10mM NaCl solution)[38]. However, the two remaining factors, current leakage beside the membrane and

water splitting at high voltage may be able to decrease current efficiency[41].

This observed saturation of salt-removal efficiency in the overlimiting regime also can be explained by the following. At 50 V, the depletion zone and the vortices are observed at 0 mm (Fig. 2.8d). At 100 V, ultra-strong vortices from IEMs appear, resulting perfect salt removal (as monitored by R6G) at the very front end of the channel (Fig. 2.4). In detail, due to these strong vortices, almost all salts can be removed before 15 mm at 20 V, 6 mm at 50 V, and ~0 mm at 100V (Fig. 2.4). After the concentration drops below ~1 mM at the rear part of the channel, more current flows through the front part of the channel. The electric conductivity of 1 mM NaCl is too low to allow enough current flow (Fig. 2.3). As a result, instead of additional salt removal below 1 mM, the required length for obtaining 1 mM from 10 mM NaCl solution decreases as the voltage increases. This also can explain why the current and the conductivity in the desalted flow are almost saturated after 20 V (Fig. 2.10a). However, it is noted that, this does not mean ED system cannot obtain ultra-pure water below 1 mM; while the conductivity of desalted channel is almost saturated, it keeps decrease gradually from 1.002 mM (125.60 μS/cm) at 20 V to 0.799 mM (99.16 μS/cm) at 100 V.

2.5. Outlook and Future Works

In this chapter, we investigated the clear change of dynamics from Ohmic to overlimiting regime through the comparison of measurable parameters (current, voltage, conductivity, and current efficiency) and visualized concentration / flow profiles. Although this experimental platform enables better understanding of nonlinear ICP and OLC, several scientific issues come to the front as a result.

One of the important issues is the marked difference of the optimized operating condition and current efficiency between research papers including ours and commercialized ED systems. According to the recent article published by GE[2], which is one of the leading companies for ED technology, the optimized condition has been always on Ohmic regime with 90-95% of current efficiency. However, the current efficiency has been observed in the wide range (10-80%) in research papers[17]. This significant discrepancy is probably due to the difference of the system scale between ED plants and lab-scale devices; although the commercial ED is highly stacked (> several hundred cell pairs), ED in research papers has only 1-20 cell pairs. It is also noteworthy that ED systems in commercial market and research papers have quite different geometries (*e.g.* intermembrane distance: 1-10mm[15, 17, 42]) and flow conditions, probably resulting inconsistency of current efficiency. The best way to solve this issue is to study overlimiting regime with commercial ED devices or similar multi-stacked system.

Secondly, although conductivity drop of desalted flow (Fig. 2.2b) and current efficiency (Fig. 2.14) are good indicators, these performance metrics do not take into account energy consumptions (electric and pumping energy) and capital cost (*e.g.* the required membrane area). For example, as visualized in the Fig. 2.4, the required channel length for desalting water below a certain level (< 1 mM) becomes shorter with higher applied voltage (or current). This indicates the pumping power and the required membrane size can be significantly reduced. In the fluidic

channel, the pumping power is proportional to the flow rate and pressure drop along the channel, and this pressure drop is proportional to the length of the channel. Therefore, one can probably reduce the overall cost to operate the system, and build smaller, portable device at higher electric potential. To find the optimization point, we need to quantify desalting performance with various indicators, including energy consumption, energy per ion removal, area efficiency, *etc.*. This issue will be revisited in Chapter 4.

Next, there are still many parameters which can affect the device performance and change the optimization point. Here, we only change voltage or current regimes at fixed geometry, component and salinity of the solution, flow rates, and water recovery (50%). This means that there is still much possibility to enhance the performance of ED by characterizing the detailed ion transport with microscopic details. The questions to be explored in the future are the following:

i) Here, we used the brackish water model (10mM NaCl). Can nonlinear ICP and OLC help to enhance ED's performance in different salinities of water, such as ultra-pure water generation (< 0.1mM), seawater desalination (~500mM), and produced water treatment (> 1M)?

ii) Here, we used the binary electrolyte (NaCl). As discussed in Chapter 2.2, different electrolytes or ions induce different limiting current density and probably different critical voltage to initiate electroconvection. Then, how will desalting performance and optimization point be shifted according to the component of electrolytes (*e.g.* non-binary electrolytes and complex salt mixtures)?

iii) We can control water recovery by adjusting flow rate ratio of desalted and brine flows. Then, what is the optimized water recovery and flow rates, in the light of achieving the

best possible energy efficiency (*i.e.* energy per ion removal)?

iv) The thickness of depletion zone governs the amount of rejected salts in desalted flow (described in Chapter 4), and the thickness increases (decreases) as higher voltage or current (higher flow rate or velocity) (described in Chapter 3). Then, what is the optimized thickness of depletion zone, flow rate, and the width of the desalted channel?

Lastly, the ability of visualization of this microscale experimental platform would be useful for various electrochemical desalination systems such as capacitive deionization (CDI) and electrodeionization (EDI). As in ED, CDI and EDI's parameters related to the ion transport are yet to be characterized in microscopic detail. Because their system designs are quite similar with ED (CDI: two juxtaposed porous electrodes, EDI: juxtaposed IEMs and ion exchange resins between IEMs), we will be able to fabricate microscopic visualization platforms with methods demonstrated here.

References

[1] V. D. Grebenyuk, and O. V. Grebenyuk, Russ J Electrochem+ **38**, 806 (2002).

[2] E. R. Reahl, General Electric Company Available from: http://www.gewater.com/pdf/Technical%20Papers_Cust/Americas/English/TP1038EN.pdf (2004).

[3] H. Strathmann, Desalination **264**, 268 (2010).

[4] F. G. Donnan, Z Elktrochem Angew P **17**, 572 (1911).

[5] T. Teorell, Proc. Natl. Acad. Sci. U. S. A. **21**, 152 (1935).

[6] W. Juda, and W. A. Mcrae, J Am Chem Soc **72**, 1043 (1950).

[7] T. Humplik, J. Lee, S. C. O'Hern, B. A. Fellman, M. A. Baig, S. F. Hassan, M. A. Atieh, F. Rahman, T. Laoui, R. Karnik, and E. N. Wang, Nanotechnology **22**, (2011).

[8] S. J. Kim, S. H. Ko, K. H. Kang, and J. Han, Nat Nanotechnol **5**, 297 (2010).

[9] M. A. Shannon, Nat Nanotechnol **5**, 248 (2010).

[10] I. Rubinstein, and B. Zaltzman, Phys Rev E **62**, 2238 (2000).

[11] I. Rubinstein, and B. Zaltzman, Adv. Colloid Interface Sci. **159**, 117 (2010).

[12] V. V. Nikonenko, N. D. Pismenskaya, E. I. Belova, P. Sistat, P. Huguet, G. Pourcelly, and C. Larchet, Adv. Colloid Interface Sci. **160**, 101 (2010).

[13] V. A. Shaposhnik, V. A. Kuzminykh, O. V. Grigorchuk, and V. I. Vasileva, J. Membr. Sci. **133**, 27 (1997).

[14] V. A. Shaposhnik, V. I. Vasil'eva, and O. V. Grigorchuk, Adv. Colloid Interface Sci. **139**, 74 (2008).

[15] V. I. Vasil'eva, V. A. Shaposhnik, O. V. Grigorchuk, and I. P. Petrunya, Desalination **192**, 408 (2006).

[16] E. I. Belova, G. Y. Lopatkova, N. D. Pismenskaya, V. V. Nikonenko, C. Larchet, and G. Pourcelly, Journal of Physical Chemistry B **110**, 13458 (2006).

[17] M. Sadrzadeh, and T. Mohammadi, Desalination **249**, 279 (2009).

[18] F. C. Leinweber, and U. Tallarek, Langmuir **20**, 11637 (2004).

[19] Q. S. Pu, J. S. Yun, H. Temkin, and S. R. Liu, Nano Lett. **4**, 1099 (2004).

[20] G. Yossifon, and H. C. Chang, Phys Rev Lett **101**, 254501 (2008).

[21] R. D. Chambers, and J. G. Santiago, Anal. Chem. **81**, 3022 (2009).

[22] P. R. Ojeda, I. A. K. Amashta, J. R. Ochoa, and I. L. Arbeloa, J Chem Soc Farad T 2 **84**, 1 (1988).

[23] F. L. Arbeloa, I. L. Gonzalez, P. R. Ojeda, and I. L. Arbeloa, J Chem Soc Farad T 2 **78**, 989 (1982).

[24] Z. Chen, Y. J. Tang, T. T. Xie, Y. Chen, and Y. Q. Li, J Fluoresc **18**, 93 (2008).

[25] S. J. Kim, Y. C. Wang, J. H. Lee, H. Jang, and J. Han, Phys. Rev. Lett. **99**, (2007).

[26] S. M. Rubinstein, G. Manukyan, A. Staicu, I. Rubinstein, B. Zaltzman, R. G. H. Lammertink, F. Mugele, and M. Wessling, Phys Rev Lett **101**, 236101 (2008).

[27] G. Yossifon, P. Mushenheim, Y. C. Chang, and H. C. Chang, Phys Rev E **81**, (2010).

[28] A. J. Bard, and L. R. Faulkner, *Electrochemical Methods: Fundamentals and Applications* (John Wiley and Sons, Inc., 2001), second edition edn.

[29] J. Newman, and K. E. Thomas-Alyea, *Electrochemical Systems* (John Wiley and Sons, Inc., 2004), third Edition edn.

[30] R. F. Probstein, *Physicochemical Hydrodynamics: An Introduction* (Wiley-Interscience, New York, 2003), 2 edn.

[31] S. J. Kim, Y. A. Song, and J. Han, Chem. Soc. Rev. **39**, 912 (2010).
[32] Y. C. Wang, A. L. Stevens, and J. Y. Han, Anal. Chem. **77**, 4293 (2005).
[33] R. Kwak, S. J. Kim, and J. Han, Analytical Chemistry **83**, 7348 (2011).
[34] S. J. Kim, Y. C. Wang, J. H. Lee, H. Jang, and J. Han, Phys Rev Lett **99**, 044501 (2007).
[35] E. V. Dydek, B. Zaltzman, I. Rubinstein, D. S. Deng, A. Mani, and M. Z. Bazant, Phys Rev Lett **107**, 118301 (2011).
[36] R. Valerdi-Perez, and J. A. Ibanez-Mengual, Desalination **141**, 23 (2001).
[37] H. J. Lee, H. Strathmann, and S. H. Moon, Desalination **190**, 43 (2006).
[38] C. Larchet, L. Dammak, B. Auclair, S. Parchikov, and V. Nikonenko, New Journal of Chemistry **28**, 1260 (2004).
[39] I. Rubinstein, Phys Fluids a-Fluid **3**, 2301 (1991).
[40] J. H. Choi, H. J. Lee, and S. H. Moon, J Colloid Interf Sci **238**, 188 (2001).
[41] V. V. Nikonenko, N. D. Pis'menskaya, and E. I. Volodina, Russ J Electrochem+ **41**, 1205 (2005).
[42] Y. Tanaka, J Membrane Sci **216**, 149 (2003).

Chapter 3

Electroconvective Vortex (EC) Characteristics under Shear Flow[2]

3.1. Introduction to EC on IEMs

As described above, while important in many electrochemical systems, physical modeling of ICP remains challenging due to multiphysics, multiscale nature of the problem. One of the most tantalizing problems in ICP is the mechanism of overlimiting current (or overlimiting conductance)(OLC)[1], which cannot be explained by the standard theory of ICP[2] that considers only diffusion and drift. Various mechanisms for OLC have been proposed, including electroconvection(EC) (electroosmotic instability[3-6] and bulk electroconvection[7, 8]), chemical reaction (water splitting[1]), and electrostatic effects (surface conduction and electroosmotic flow[9]). While different non-chemical mechanisms were considered important according to the scale of systems[9], EC mechanism has been tied to OLC in macroscale systems (*e.g.* electrodialysis (ED)) with experimental evidences[5, 6, 10] and theoretical predictions[4, 6] of symmetric vortex pairs. Recently, however, Andersen *et al.*[11] argued that EC may be not the source of OLC for following reasons. **i)** Experiments[5, 6, 10] were performed in microfluidic devices, and there are different source of vortex by electrostatic effects[9] or unsymmetrical geometry (nanochannels were located only on the bottom of the channel). **ii)** Also, flat depletion zone (with low concentration) is not the evidence of EC, since it can occur in microchannels without EC[12]. **iii)** Especially, the chemical effects "current-induced membrane discharge" could generate OLC and also suppress EC in real systems[11].

Perhaps the scientific difficulty regarding the ICP and OLC is due to the fact that there has

[2] The published journal paper (R. Kwak, V. S. Pham, K. M. Lim, and J. Y. Han, Phys. Rev. Lett. **110**, 114501 (2013)) was used in its entirety for Chapter 3, with minor updates and modifications. Among the authors, R. K. and J. H. conceived the idea, designed the experiments, and wrote the manuscript. R. K. carried out the experiments and analyzed the data. V. S. P carried out the simulations, and this work supervised by K. M. L. G. G and W. K. P. fabricated the PDMS molds by 3D printing. J. H. supervised the overall study.

been a general lack of direct experimental studies. Most previous studies[1, 4-10, 12, 13] often captured ion / fluid transport behaviors with 1-D quiescent conductance in over-simplified systems, which cannot represent conditions of real electrochemical systems. Consequentially, they also failed to capture the effect caused by shear flow, even though many engineering systems, from conventional ED systems to new ICP devices (*e.g.* preconcentration[14] and desalination systems[15]) operate under shear flow in tangential direction to IEMs. While Balster *et al.* discussed the effect of flow direction on micro-textured membranes, they did not go into microscopic details[16]. In Chapter 2, we developed a microscale ED system and visualized *in situ* fluid flow and ion concentration, for the purpose of investigating and optimizing ED process. In this chapter, using the micro ED platform, we investigate concentration profile and fluid flow of ICP, and verify the existence of EC under various shear flow conditions and voltages. The experimental result is then compared with recently-developed multiscale numerical simulation[17]. In addition, new scaling relation between the thickness of EC vortex and shear flow rate is established and validated. We also reveal the unique unidirectional vortex structure and vortex advection in sheared EC for the first time.

3.2.EC under Shear Flow in ED

3.2.1. Sheared EC in ED

Fig. 3.1 shows typical flows and ion concentration characteristics observed in the experimental system. It is noted that all parameters are controllable (*e.g.* flow rate, voltage, and geometry) or traceable (*e.g.* streamline, current, conductivity) in the micro ED platform. We also carried out multi-scale numerical simulation, based on the routines developed by Pham *et al.*(all simulations in Chapter 3 are courtesy by Van Sang Pham)[17]. The simulation relies on the direct, coupled solution of the full set of Poisson-Nernst-Plank-Navier-Stokes equations(see Appendix A, Fig. A1). Fig. 3.2 shows the behavior of ion concentration polarization under shear flow: sheared EC with local ion concentrations and fluid flows, obtained from experiment and numerical simulation. The modeling results largely reproduce both flow and concentration profiles observed in the experiments, over a range of applied voltage and shear flow rates (see Fig. 3.3 for full set of experimental data). As previously observed without shear[10], the series of wavy depletion boundary layers (thickness: d_{bl}) are generated near IEMs because EC enhances the convective mixing. However, there are unique behaviors of ICP under shear flow which have not been predicted / observed until now. These behaviors are clearly different from the traditional picture of convective-diffusive model[2], and even from the model by Rubinstein and Zaltzman[4] where symmetric bi-directional vortex were predicted.

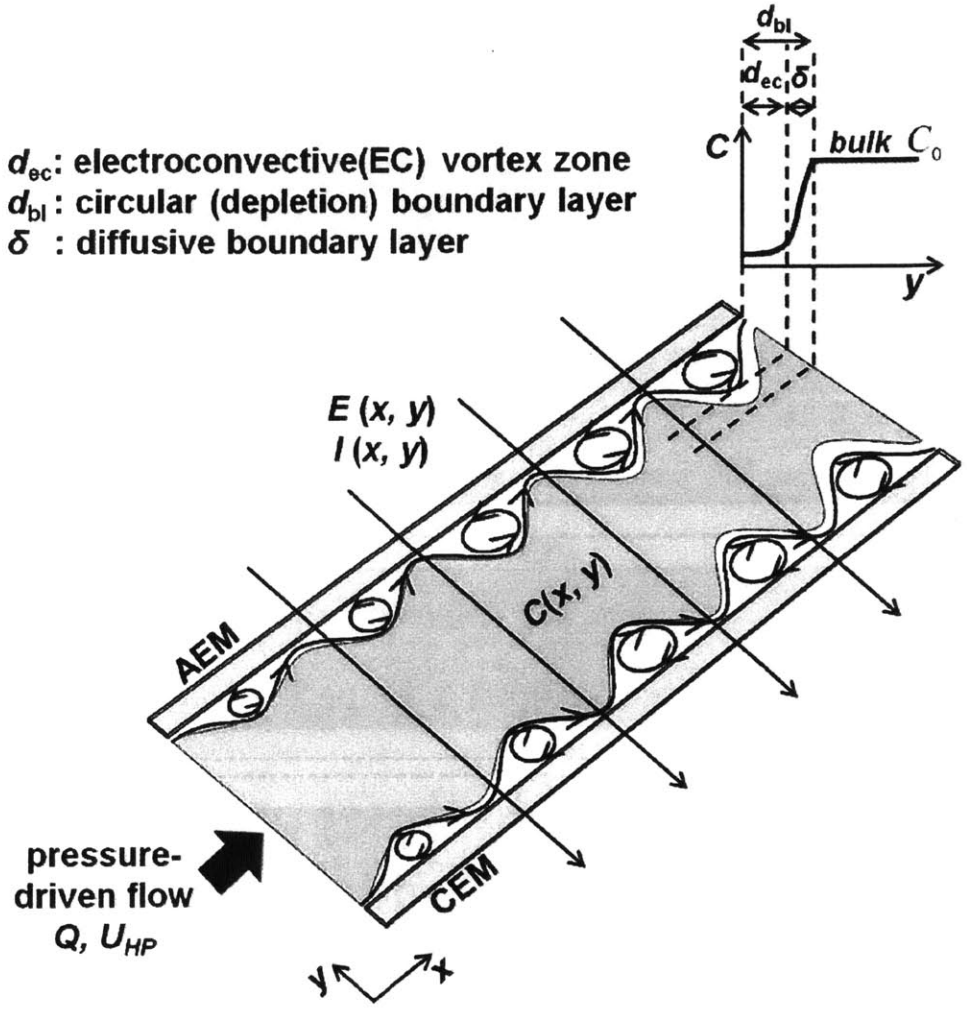

Figure 3.1 Schematic diagram of sheared EC vortices (black ellipses) and ion concentration profiles C initiated by ICP under shear flow in the microscale ED system. When the pressure-driven HP flow (with flow rate Q and average velocity U_{HP}) is applied, with a sufficient high voltage V, the EC zone d_{ec} and the corresponding circular depletion boundary layer d_{bl} are observed on both CEM and AEM. The vortices have only one direction (clockwise on CEM and counter-clockwise on AEM), instead symmetric pairs. By combining the unidirectional vortices and HP flow, meandering fluid flows are induced above the EC vortices. A typical concentration profile (at the maximum height of the vortex) near the AEM, along with the thicknesses of d_{ec}, d_{bl}, and δ are shown in the inset. C_0 indicates the 'bulk' concentration at a given location, which gradually decreases downstream of the channel by electrodialysis[18]. The direction of electric field E and current I is from AEM to CEM (black arrows). The detailed fabrication and operating procedures are described in Section 2.2.

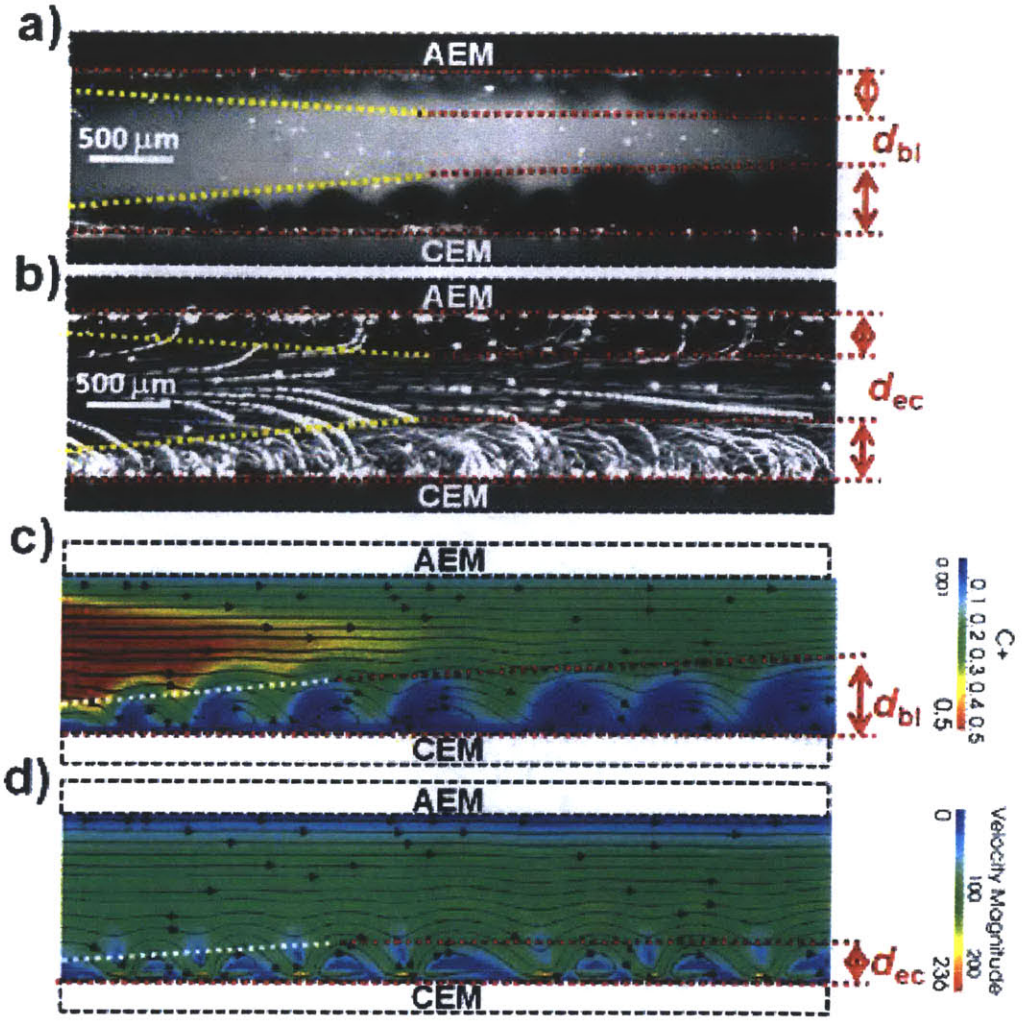

Figure 3.2 Sheared ICP is visualized by showing local ion concentration profiles (Fig. 3.2a and c) and EC vortices (Fig. 3.2b and d) from the experiment (at V=10 V and U_{HP} = 0.83 mm/s (Q=10 μL/min)(Fig. 3.2a-b) and the simulation (at V= $25V_0$ and U_{HP}= $80U_0$, where V_0 =25 mV and U_0 =29.66 μm/s(see Appendix A, Table A1)) (Fig. 3.2c-d). CEM (AEM) is located at the bottom (top) of the channel, and the ratio of channel width to length is 1:5 in both the experiment and the simulation. In the experiment, the local ion concentration was tracked with 10 μM Rhodamine 6G (R6G), and circular depletion boundary layers d_{bl} are observed as a dark region caused by the depletion of R6G (Fig. 3.2a); in simulation, ion depletion is represented as a blue region (Fig. 3.2c). Fluid flows were visualized by stacking the time-lapse images of 10μm polystyrene (PS) beads (Fig. 3.2b). The vortex evolution is clearly visualized at the entrance region in both the experiment and the simulation (yellow and white dotted lines).

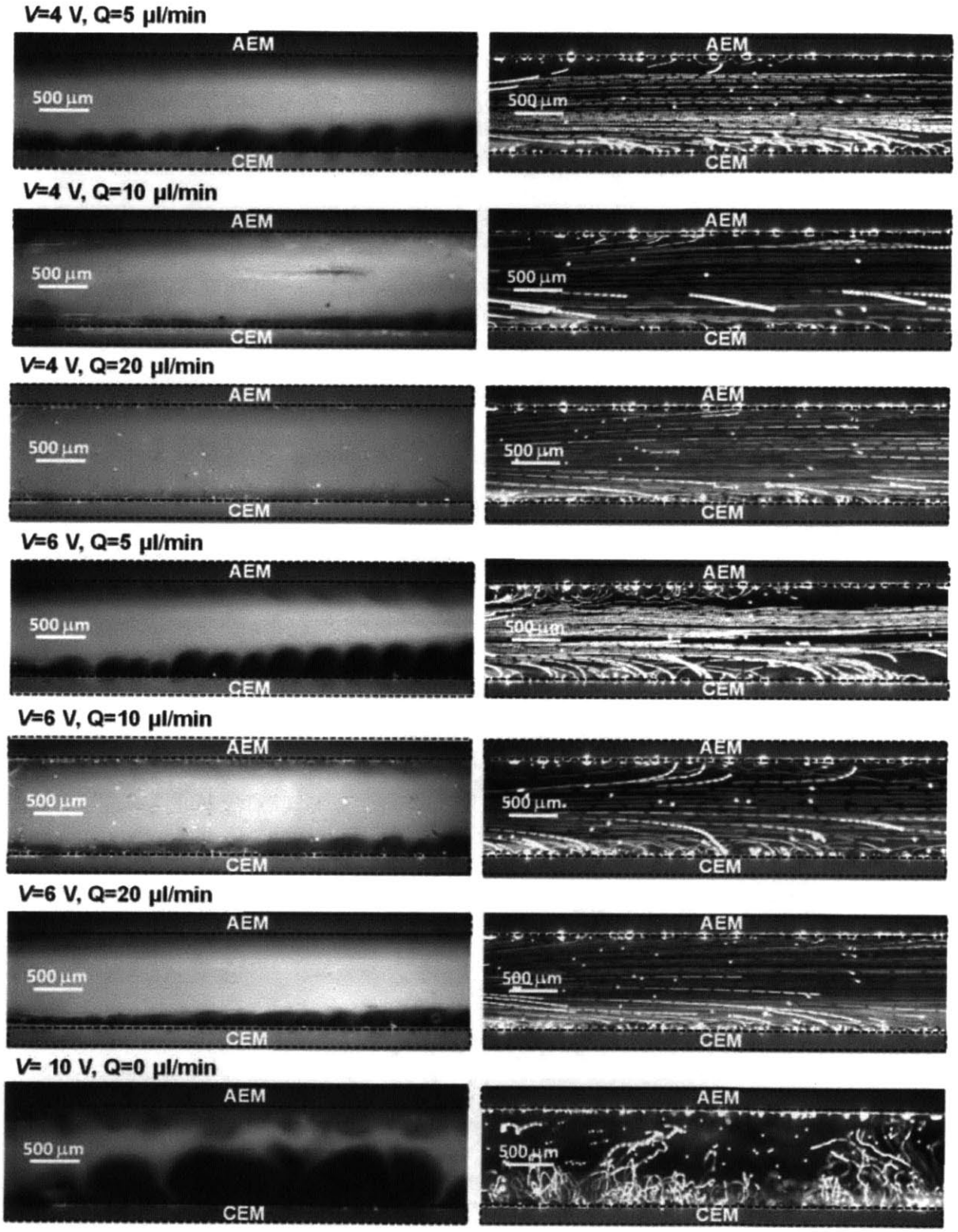

Figure 3.3 The full set of experimental results with various conditions (applied voltage: 4~20V, flow rates: 0~50μL/min). Ion concentration (left) and fluid flows (right) were visualized by 10 μM R6G and 10 μm PS beads, respectively. When U_{HP}=4.2 mm/s (Q=50μL/min), EC vortices were not distinguished themselves clearly, so the advection speed could not be determined.

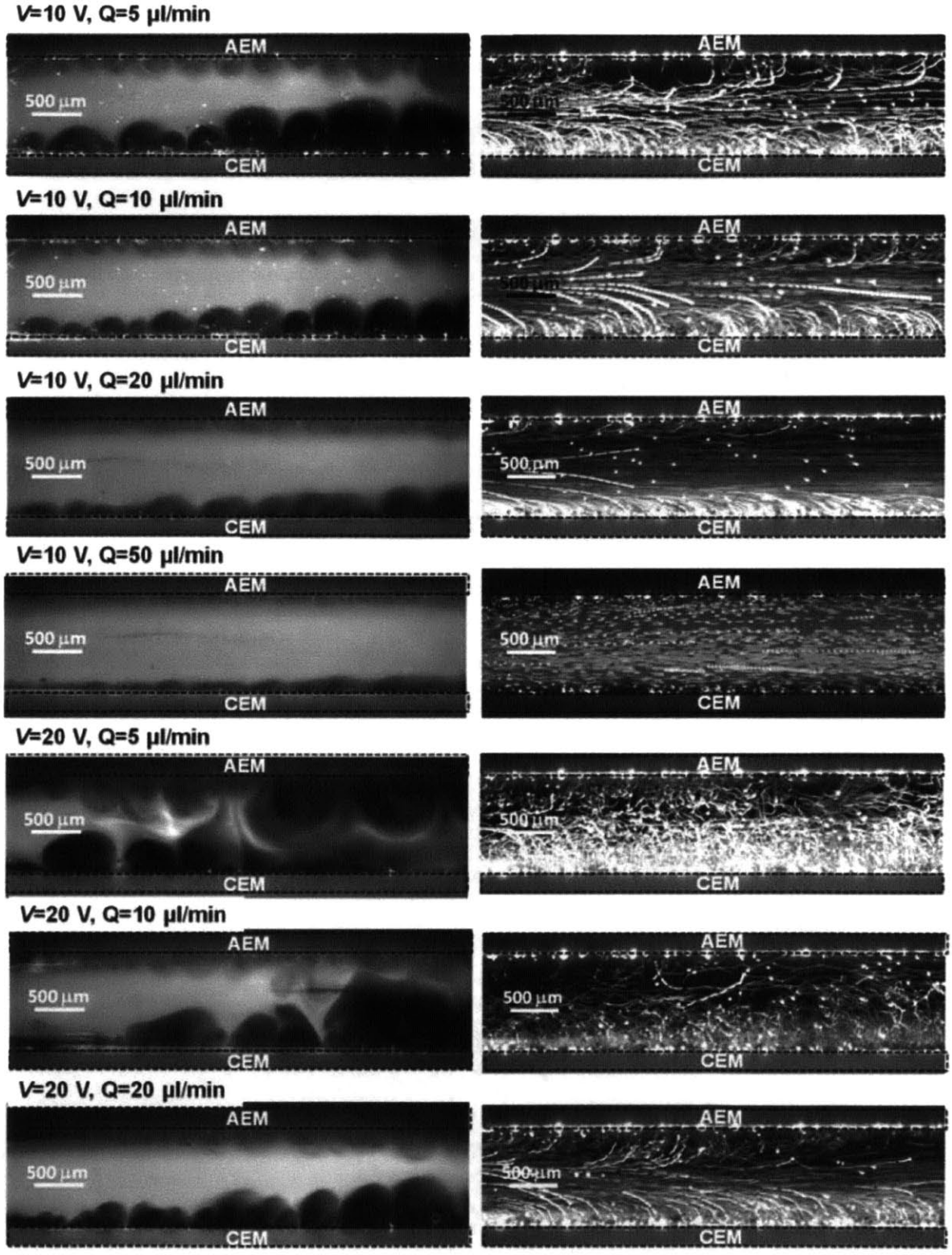

Figure 3.3 (continued)

3.2.1. Unidirectional Vortex Structure of Sheared EC

The first unique behavior is unidirectional electroconvective vortices, in contrast with symmetric vortex pairs predicted and observed for the situation without shear flow[6, 10]. When Hagen–Poiseuille (HP) flow is applied from left to right, only clockwise vortices on CEM and only counter-clockwise vortices on AEM occur (Fig. 3.1 and 3.2). Unfavorably-directed vortices are suppressed by the shear flow, and favorably-directed vortices are expanded in the lateral direction; as a result, flow streamlines meander along the edges of these vortices. This shift from symmetric vortex pairs to asymmetric, unidirectional vortex by shear was previously observed in annular 'electroconvection' in liquid crystal films[19, 20]. Electroconvective vortices and corresponding ion depletion on AEM are weaker (or none in simulations) than that on CEM, due to the difference of transport properties and Stokes' radius of cation and anion (sodium and chlorine ions); the limiting currents and the overlimiting threshold voltages to generate EC are different for CEM and AEM (Fig. 2.2a)[1, 21].

3.2.2. Height Selection of Sheared EC

The second unique behavior is the height selection of electroconvective vortex zone as a function of applied voltages and flow velocities. The vortex height becomes saturated, after it evolves completely at a certain distance from the entrance region of the channel (yellow and white dotted lines in Fig. 3.2). This reflect that the vortex evolution needs a few seconds[10, 18, 22]. After this evolution, we chose the thickness of EC vortex zone d_{ec} by a meandering streamline, which shows strong vertical motions (y-direction) up to the IEMs' surfaces (black wavy streamlines in Fig. 3.1, red dotted lines in Fig. 3.2b and d). This parameter largely determines the overall conductance (efficiency) of ion transport in the system. The corresponding circular depletion boundary layer d_{bl} is determined from the maximum height of regions with

appreciable concentration modification from the fluorescent images (dark regions in Fig. 3.1, red dotted lines in Fig. 3.2a and c); this layer includes the EC vortex zone d_{ec} and the diffusive boundary layer δ ($\delta = d_{bl} - d_{ec}$).

The governing equations for describing ion transport across IEM are Nernst-Plank equations, Poisson's equation, and Stokes' equations (with electric body force), which represent mass transport, electrostatic balances, and viscous fluid flows[7, 23]. Combining Poisson's equation and Stokes' equation, we obtain $0 = -\nabla P + \mu\nabla^2 u + \varepsilon\nabla^2\phi\nabla\phi$; Here, the first and last terms can be considered as 'source terms' (responsible for the viscous flow), representing the external pressure gradient and the electric body force on residual space charge, respectively (P: pressure, μ: dynamic viscosity, u: flow velocity, ε: electric permittivity, and ϕ: electric potential). If there is no external pressure gradient or shear flow, the viscous term and the electric body force term are balanced. ($\mu\nabla^2 u \sim \varepsilon\nabla^2\phi\nabla\phi$). If we assume the electroconvective vortex and the electric potential drop occur only in EC zone d_{ec} (almost all potential drop occurs within d_{ec}, due to significantly low ion concentrations(see Appendix A, Fig. A3)[14, 15, 18]), we obtain a simple linear relation between d_{ec} and ϕ ($d_{ec} \sim \sqrt{\varepsilon/\mu\omega}\cdot\phi$, $\omega = \nabla\times u$: vorticity) as observed in previous works[5, 6, 10].

When HP flow is applied, however, we have to consider the external pressure gradient as well as electroconvective flow generated from the membrane walls. The tangential flow is developed by the external pressure gradient, and the vortical flow is developed by the electric body force. At the boundary of the EC zone d_{ec}, therefore, these two driving forces will be balanced, $\nabla P \sim \varepsilon\nabla^2\phi\nabla\phi$. The pressure gradient can be described with the average flow velocity of HP flow U_{HP}, and the hydrodynamic diameter of the channel D_h, $P/L \sim 64\mu U_{HP}/D_h^2$, and

$D_h = 2wh/(w+h)$ for rectangular channels (L: length, w: width, h: height)[24]. As a result, we obtain a scaling relation for sheared EC (the detailed derivation is described in Appendix A);

$$\frac{d_{ec}}{w} \sim C\left(\frac{\phi^2}{U_{HP}}\right)^{1/3}, \quad C = \left[\frac{\varepsilon}{64\mu w^3}\left(\frac{2wh}{w+h}\right)^2\right]^{1/3} \tag{3.1}$$

This scaling relation, which is clearly different from conventional convective-diffusive model $(d_{bl}/w)^3 \sim (D/U_{HP}w)\cdot(x/w)$ (D: diffusivity of ions)(Eq. 6.2.12 in [2]), reveals that the dimensionless thickness of EC zone d_{ec}/w is linearly proportional to $\left(\phi^2/U_{HP}\right)^{1/3}$. The scaling constant C, predicted from structural parameters of the channel, is 0.0107 and 0.1303 for the experimental system (w=1 mm, h=0.2 mm) and simulation (w=20 μm, $h \to \infty$), respectively (μ=0.001kg/m·s, ε=80×8.854×10^{-12} F/m). Fig. 3.4 shows the dimensionless thickness of EC zone for various experimental and simulation conditions according to the scaling factor $\left(\phi^2/U_{HP}\right)^{1/3}$. Not only that all measured values collapse onto straight lines (dotted lines in Fig. 3.4), but the slopes of lines (experiment: 0.0101/0.0107 on CEM/AEM, simulation: 0.1258) agree well with the scaling constant (error < 5%). These fitting lines do not pass through the origin, because the onset of EC instability occurs at the finite voltage (Fig. 2.2a). It is noted that the overlimiting threshold voltage is fixed even under different flow rates (Fig. 3.5).

This scaling analysis allows one to predict ion concentrations and fluid flows by sheared ICP, which routinely occurs in real electrochemical systems. At low voltage or strong HP flow, $\left(\phi^2/U_{HP}\right)^{1/3} << 1$ ($\nabla P >> \varepsilon\nabla^2\phi\nabla\phi$), the thickness of EC zone d_{ec}/w is near zero; EC is completely suppressed or flushed away by HP flow, so tangential flow patterns largely dominate in the system, with minimal diffusion layer near IEMs (Fig. 3.6). As the scaling factor $\left(\phi^2/U_{HP}\right)^{1/3}$ increases, the region governed by EC expands and the sheared EC zone begins to

appear, along with circular depletion boundary layers and meandering flow patterns. When d_{ec}/w becomes larger than 0.5, the vortices on CEM and AEM start to overlap and interact with each other, inducing strongly chaotic behaviors both for ion concentration and fluid flows. The concentration/flow profiles from simulation and experiment are well-matched when d_{ec}/w is similar, even when other parameters (*e.g.* Reynolds number and other structural dimensions) are not equal (Fig. 3.6). This would indicate that the balance of HP and EC flows primarily governs the concentration / flow profiles of the system. In this experiment and simulation, diffusion is suppressed by fast HP flow. Therefore, the diffusive boundary layers δ do not increase significantly (Fig. 3.6).

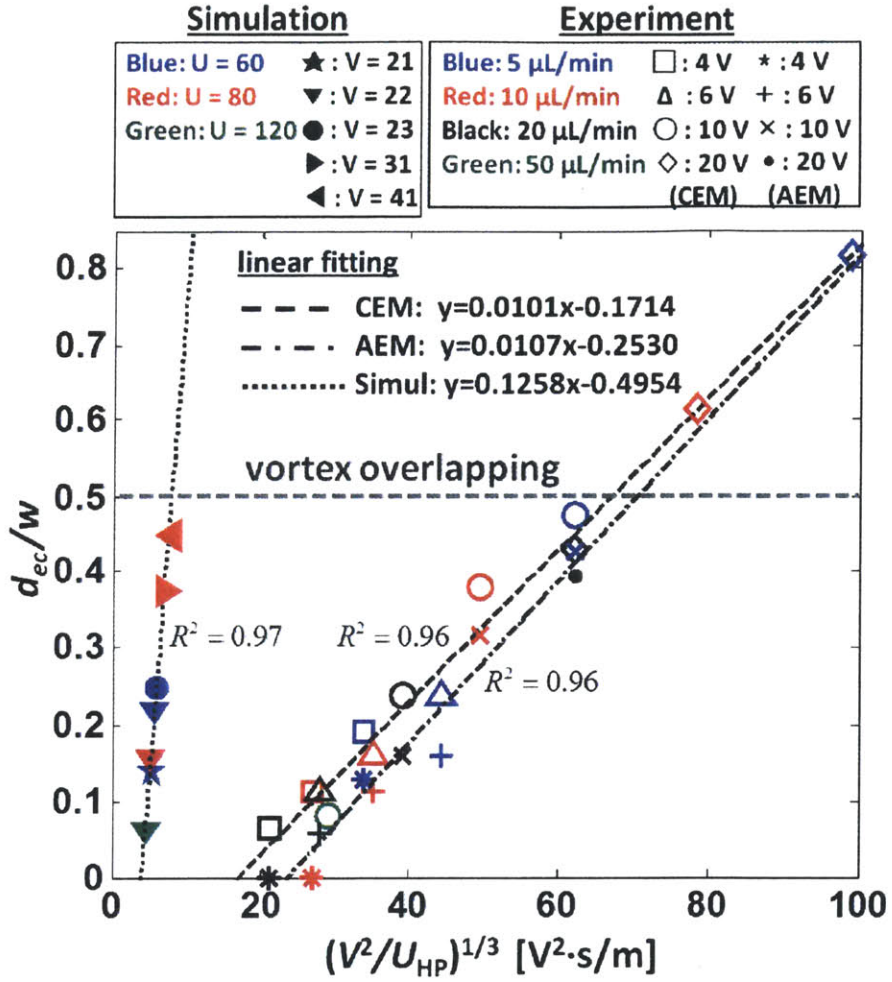

Figure 3.4 Dimensionless thickness of EC vortex zone d_{ec}/w plotted against the scaling factor $\left(\phi^2/U_{HP}\right)^{1/3}$ at various applied voltages and flow rates for both experiment (V = 4-20 V and Q= 5-50 μL/min (U_{HP} =0.42-4.17 mm/s)) and simulation (V=21V_0-41V_0 and U_{HP}=60U_0-120U_0, where V_0 =25 mV and U_0 =29.66 μm/s). Dotted lines are the best fitting straight lines for two different sets of experiment data on CEM and AEM, and one set of simulation data.

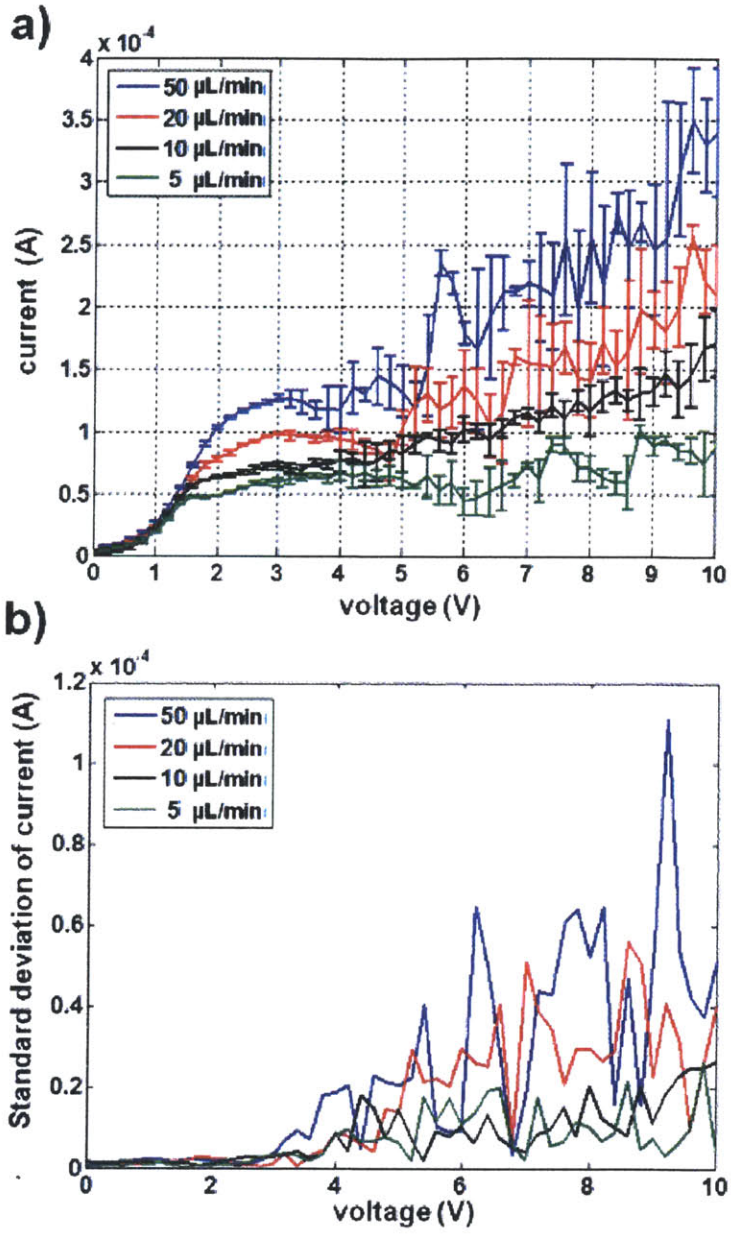

Figure 3.5 Current-voltage (IV) curves under various flow rates (Q= 5, 10, 20, 50 µL/min (U_{HP}=0.42, 0.83, 1.67, 4.17 mm/s)) to address the relation between the flow rate (shear rate) and overlimiting threshold voltage. By observing the slope change of the current-voltage curves (Fig. 3.5a) and the initiation of the current fluctuation (Fig. 3.5b), we verified that the overlimiting threshold voltage is fixed at about 4V (on the CEM side, experiment). This indicates that the initiation of electroconvection (EC) is independent of the shear flow rate. Effective electrode area was 0.2 mm×15 mm. Current-voltage response was measured by ramping up the voltage by discrete voltage jumps of 0.2 V in every 30 sec, which was repeated three times. 10 mM NaCl solution was used.

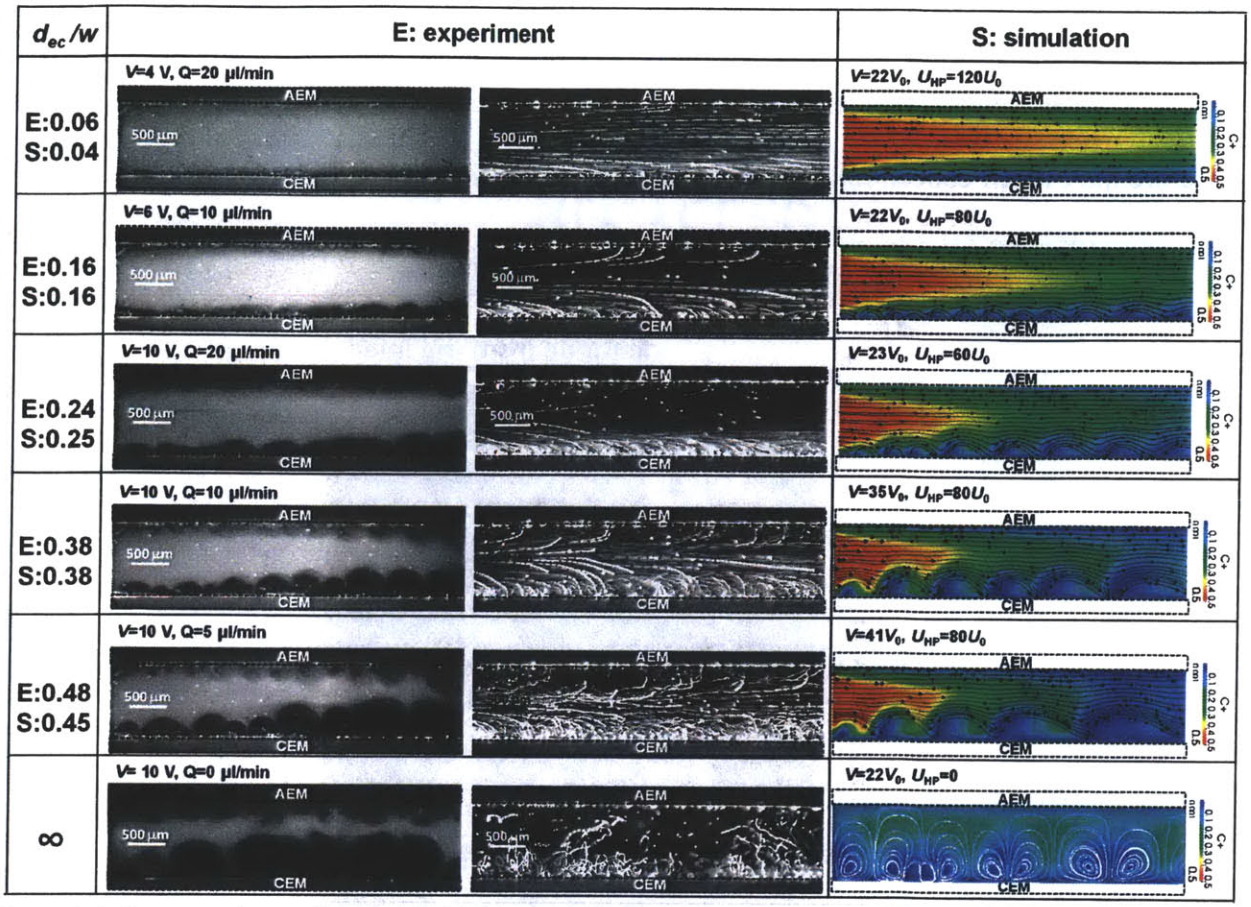

Figure 3.6 Concentration profiles and fluid flow visualized in experiment by R6G and PS bead (the first and second columns) and in simulation (the third column) at six regimes according to the dimensionless thickness of EC vortex zone on CEM, d_{ec}/w. As d_{ec}/w on CEM or $(\phi^2/U_{HP})^{1/3}$ changes, the number of EC vortices also varies. Here, the Peclet numbers are high enough to suppress significant diffusion; in experiment, when U_{HP} = 0.83 mm/s, the Peclet number $Pe_L = U_{HP}L/D_{ions}$ is 3320 (L= 4 mm, D_{ions}~10^{-9} m^2/s (D_{Na+}=1.28×10^{-9} m^2/s, D_{Cl-}=1.77×10^{-9} m^2/s[25]) and the expansion of diffusive boundary layer $\delta/w = L/(w\sqrt{Pe_L})$ is only 0.069. In simulation, when U_{HP} = 2.4 mm/s and L= 0.1 mm, Pe_L and δ/w are 240 and 0.3, respectively.

3.2.3. Advection of Sheared EC

The last unique behavior is vortex advection along the direction of shear flow (Fig. 3.7). As described in previous studies without shear, the vortex width and height are determined by the applied voltage as well as the geometry of the system[4, 6, 10]; but the position of the vortex is not fixed and can be shifted. Under tangential shear flow, EC vortices would migrate. The vortex advection speed (U_{ec}) only depends on the average flow velocity, and largely independent of the

applied voltage (Fig. 3.8). This is the case for both experimental and simulation results. As all existing vortices advect downstream, new vortices are generated at the front end of the channel; therefore the overall concentration/flow profiles are maintained, except for the temporal / spatial fluctuation (Fig. 3.7a).

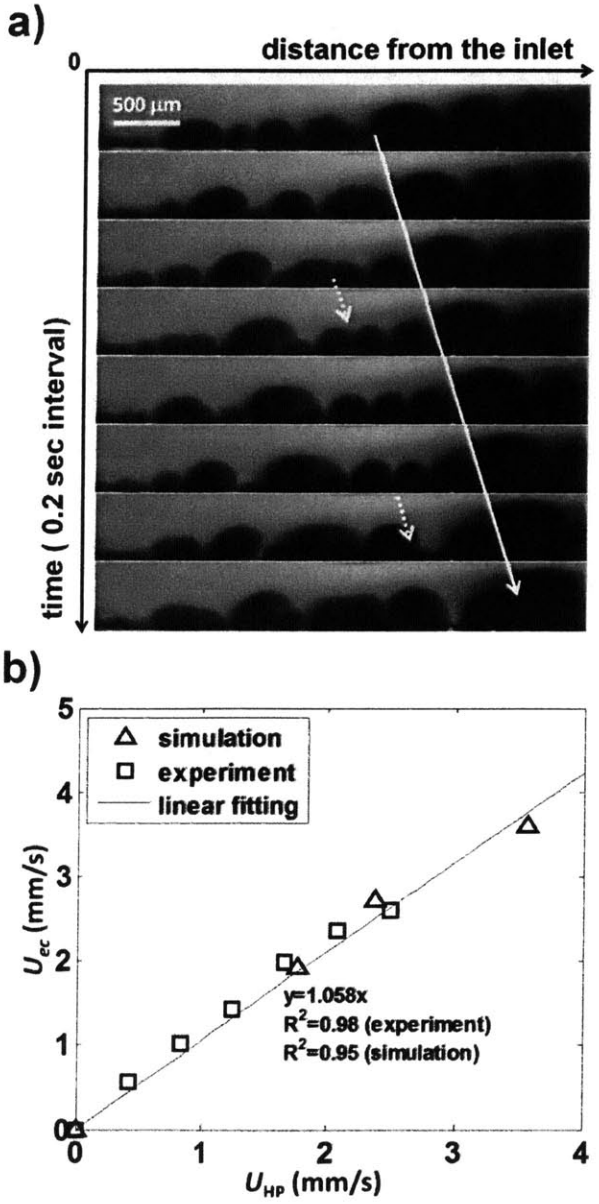

Figure 3.7 a) Space-time plot of vortex advection visualized by the corresponding circular depletion boundary layer. The time interval between adjacent images is 0.2 sec. Even when neighboring vortices merge or separate (white dotted arrows), their advection with constant speed is clearly observed (white solid arrow). **b)** vortex advection speed U_{ec} according to the average flow velocity U_{HP} (rectangular: experiments at U_{HP}=0.42-2.5 mm/s (Q=5-30 μL/min), triangle: simulations at U_{HP}= 1.78-3.56 mm/s (U_{HP}=60U_0-120U_0, U_0=29.66 μm/s)). The best fitting curves for both experiment and simulation results are the same, y=1.058x (the x-intercept is set at 0.).

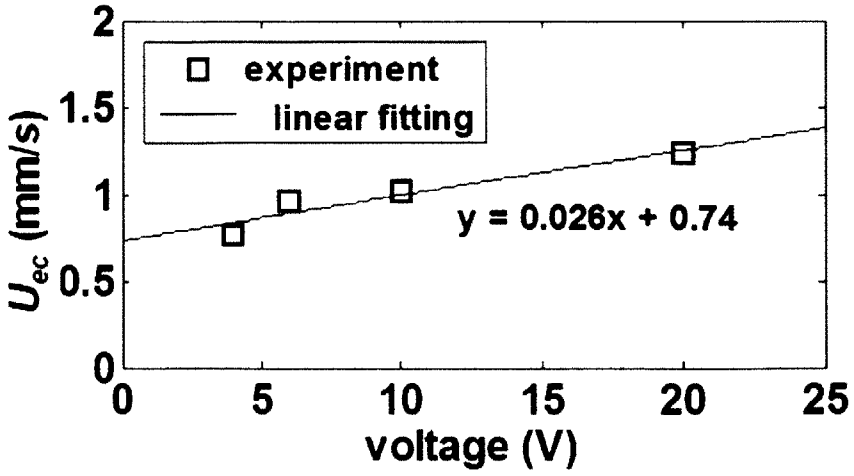

Figure 3.8 Vortex advection speed U_{ec} according to applied voltages in experiment at fixed U_{HP}= 0.83 mm/s (Q=10 μL/min). As can be seen, the speed increase slightly, but it is negligible compared to the its strong dependence on the average flow velocity U_{HP} (Fig 3.7b).

3.3. Outlook and Future Works

In this chapter, we have gained important insights on the nonlinear ICP and OLC under shear flow, and the results can be used for analyzing and optimizing commercial ED systems. Especially, the height selection of sheared EC will allow us to model desalting performances of ED in overlimiting regime.

The possible work to be done is therefore investigating the relation between the height of the EC vortices and salt removal performance in ED. The conductivity is uniformly low in the EC zone in overlimiting regime (in contrast with gradual, semi-linear decrease of ion concentration in Ohmic regime), therefore EC vortex height will be proportional to the salt removal rate in desalted flow (we will discuss this issue in Chapter 4). In addition, if we characterize the voltage-current responses in overlimiting regime with a simple scaling, we can predict energy consumption and current efficiency of ED systems.

Next, there are new scientific questions emerging from the work in this chapter. To fully elucidate the sheared EC, we need to investigate **i)** the transition from symmetric vortex to unidirectional vortex, **ii)** the vortex interactions when EC on AEM and CEM are overlapping, **iii)** the selection of vortex width (or wave number), and **iv)** vortex speed and height when the bulk conductivity is significantly decreased by desalting.

Particularly, the vortex structure transition is an interesting scientific issue. We can approach the transition from the conservation of angular momentum (*i.e.* circulation=surface integral of vorticity). In non-shear condition, the emergence of symmetric vortex pairs is due to the zero initial angular momentum. In this situation, when the shear flow is applied, the flow acts as a source of vorticity; as a result, the symmetry of vortex is broken. The unidirectional vortices we observed in this chapter would be the extreme case of strong shear flow. The vortex transition

may relate to the emergence of chaotic fluidic motions closely. As observed in Chapter 2 (Fig. 2.13) (and will be observed in Chapter 4 in Fig. 4.4), current and fluidic fluctuations are amplified when the unidirectional vortices are not developed regularly, because of vortex overlapping at sufficiently high applied voltage (or current). Although the fine distinction of the vortex symmetry is difficult to visualize, monitoring current or voltage fluctuation and simulation models can help to validate this hypothesis.

References

[1] V. V. Nikonenko, N. D. Pismenskaya, E. I. Belova, P. Sistat, P. Huguet, G. Pourcelly, and C. Larchet, Adv. Colloid Interface Sci. **160**, 101 (2010).

[2] R. F. Probstein, *Physicochemical Hydrodynamics: An Introduction* (Wiley-Interscience, New York, 2003), 2 edn.

[3] I. Rubinstein, E. Staude, and O. Kedem, Desalination **69**, 101 (1988).

[4] I. Rubinstein, and B. Zaltzman, Phys Rev E **62**, 2238 (2000).

[5] S. J. Kim, Y. C. Wang, J. H. Lee, H. Jang, and J. Han, Phys Rev Lett **99**, 044501 (2007).

[6] S. M. Rubinstein, G. Manukyan, A. Staicu, I. Rubinstein, B. Zaltzman, R. G. H. Lammertink, F. Mugele, and M. Wessling, Phys Rev Lett **101**, 236101 (2008).

[7] I. Rubinstein, Phys Fluids a-Fluid **3**, 2301 (1991).

[8] T. Pundik, I. Rubinstein, and B. Zaltzman, Phys Rev E **72**, 061502 (2005).

[9] E. V. Dydek, B. Zaltzman, I. Rubinstein, D. S. Deng, A. Mani, and M. Z. Bazant, Phys Rev Lett **107**, 118301 (2011).

[10] G. Yossifon, and H. C. Chang, Phys Rev Lett **101**, 254501 (2008).

[11] M. B. Andersen, M. van Soestbergen, A. Mani, H. Bruus, P. M. Biesheuvel, and M. Z. Bazant, Phys Rev Lett **109**, 108301 (2012).

[12] A. Mani, and M. Bazant, Phys Rev E **84**, (2011).

[13] I. Rubinstein, and B. Zaltzman, Adv. Colloid Interface Sci. **159**, 117 (2010).

[14] R. Kwak, S. J. Kim, and J. Han, Analytical Chemistry **83**, 7348 (2011).

[15] S. J. Kim, S. H. Ko, K. H. Kang, and J. Han, Nat Nanotechnol **5**, 297 (2010).

[16] J. Balster, M. H. Yildirim, D. F. Stamatialis, R. Ibanez, R. G. Lammertink, V. Jordan, and M. Wessling, J Phys Chem B **111**, 2152 (2007).

[17] V. S. Pham, Z. Li, K. M. Lim, J. K. White, and J. Han, Phys Rev E **86**, 046310 (2012).

[18] R. Kwak, G. Guan, W. K. Peng, and J. Han, Desalination (DOI:10.1016/j.desal.2012.07.017, 2012).

[19] Z. A. Daya, V. B. Deyirmenjian, S. W. Morris, and J. R. de Bruyn, Phys Rev Lett **80**, 964 (1998).

[20] Z. A. Daya, V. B. Deyirmenjian, and S. W. Morris, Phys Fluids **11**, 3613 (1999).

[21] N. P. Berezina, N. A. Kononenko, O. A. Dyomina, and N. P. Gnusin, Adv Colloid Interfac **139**, 3 (2008).

[22] E. A. Demekhin, V. S. Shelistov, and S. V. Polyanskikh, Phys Rev E **84**, 036318 (2011).

[23] S. J. Kim, Y. A. Song, and J. Han, Chem. Soc. Rev. **39**, 912 (2010).

[24] F. M. White, *Fluid Mechanics* (McGraw-Hill, New York, 2003), 5th ed. edn.

[25] S. Koneshan, J. C. Rasaiah, R. M. Lynden-Bell, and S. H. Lee, J. Phys. Chem. B **102**, 4193 (1998).

Chapter 3 Appendix A

Simulation setup (courtesy by Van Sang Pham)

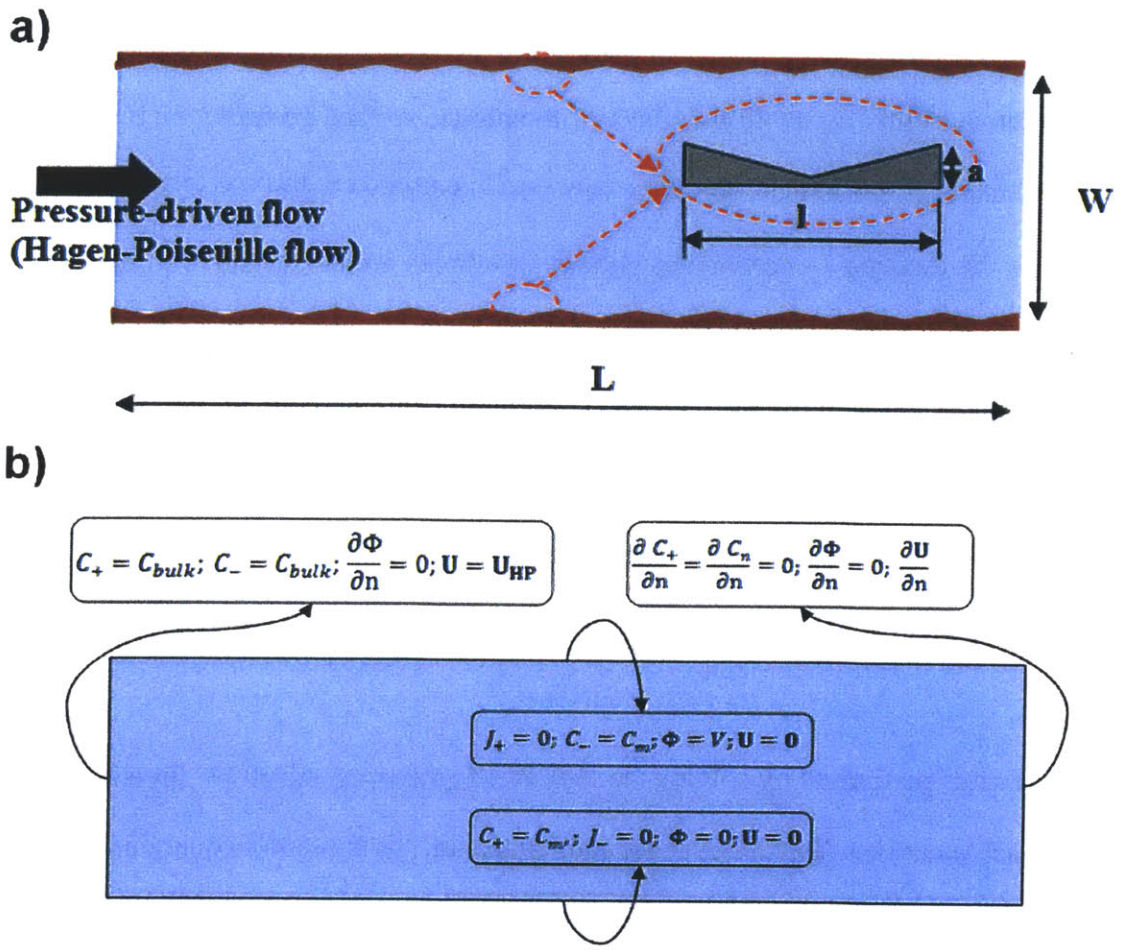

Figure A1. a) Simulation model of ED and **b)** boundary conditions

In order to obtain simulation results for the ED cell, we consider a simulation model sketched in Fig. A1, where an ED cell consists of a CEM and an AEM on top and bottom, respectively. A pressure-driven flow of electrolyte solution enters the channel from the left end, and exits to the right end. To mimic the membranes' micron or sub-micron roughness, the membranes are modeled by a series of wavy perm-selective surface (Fig. A1a). This IEM wavy surface is to produce a periodical electric field; this generates a small, perturbative fluid motion when an external electric field is applied. Such a fluid flow perturbation is typically confined within the

distance of ~O(a) (a: the amplitude of the membrane surface) in the Ohmic regime, and therefore does not lead to significant changes in ion transport. However, in the overlimiting regime, this perturbation can lead to significant fluid instability and changes in both ion concentration and flux. To avoid the effect of membrane surface geometry on the fluid flow, the wave amplitude is purposely chosen to be very small compared to the wavelength (a/l =0.001). It is noted that the limiting / overlimiting voltage thresholds are not sensitive to the change of the wavelength at fixed wave amplitude. At a/l =0.001, if the wavelength l changes ~100%, the threshold voltage shifts only by ~1-2%[1]. A significant increase of the wavelength l (*i.e.* becoming a flat membrane) will weaken the gradient of the lateral electric field, so the extended space charge layer (developed outside the electric double layer of the membrane) is less unstable on the same applied voltage; hence, a larger threshold voltage is required for generating the instability.

Simulation is performed by solving the full set of governing equations directly, including the Nernst-Planck equations (Eq. A1-A2) for ions transport, the Poisson's equation (Eq. A3-A4) for the dependence of electric potential field on the ion concentrations, and Navier-Stokes and fluid continuity equations (Eq. A5-A6) for fluid motion in the channel[1]. These equations are given in dimensionless form as follows,

$$\frac{1}{\tilde{\lambda}_D}\frac{\partial \tilde{C}_\pm}{\partial \tilde{t}} = -\nabla \cdot \tilde{\mathrm{J}} \tag{A1}$$

$$\tilde{\mathrm{J}}_\pm = -\tilde{D}_\pm\left(\nabla \tilde{C}_\pm + Z_\pm \tilde{C}_\pm \nabla \tilde{\Phi}\right) + Pe\tilde{\mathrm{U}}\tilde{C}_\pm \tag{A2}$$

$$\tilde{\lambda}_D^2 \nabla \cdot \left(\nabla \tilde{\Phi}\right) = -\tilde{\rho}_e \tag{A3}$$

$$\tilde{\rho}_e = Z_+ \tilde{C}_+ + Z_- \tilde{C}_- \tag{A4}$$

$$\frac{1}{Sc}\frac{1}{\tilde{\lambda}_D}\frac{\partial \tilde{\mathrm{U}}}{\partial \tilde{t}} = -\nabla \tilde{P} + \nabla^2 \tilde{\mathrm{U}} - \mathrm{Re}\left(\tilde{\mathrm{U}}\cdot\nabla\right)\tilde{\mathrm{U}} - \tilde{\rho}_e \nabla \tilde{\Phi} = 0 \tag{A5}$$

$$\nabla \cdot \tilde{\mathrm{U}} = 0 \tag{A6}$$

where $\tilde{t} = t/\tau_0$, $\tilde{C}_+ = C_+/C_0$, $\tilde{\phi} = \phi/\phi_0$, $\tilde{\mathrm{U}} = \mathrm{U}/U_0$, $\tilde{P} = P/P_0$ are the normalized time, ion concentrations, electric potential, vector of fluid velocity, and pressure, respectively. The corresponding reference values are given as follows.

$$\tau_0 = \frac{l_0^2}{D_0}; C_0 = C_{\mathrm{bulk}}; \phi_0 = \frac{k_B T}{Ze}; U_0 = \frac{\varepsilon \phi_0^2}{\eta l_0}; P_0 = \frac{\eta U_0}{l_0} \tag{A7}$$

where C_{bulk} is the bulk concentration, $l_0 = w$ is the characteristic length scale, $D_0 = (D_+ + D_-)/2$ is average diffusivity, k_B is the Boltzmann constant, T is absolute temperature, e is the elementary charge, Z is ion valence, η is dynamics viscosity of solution, and ε is permittivity. Parameters $\tilde{D}_\pm = D_\pm / D_0$, $\tilde{\lambda}_D = \lambda_D / l_0$, and $\tilde{\rho}_e = \rho_e / C_{\mathrm{bulk}}$ are normalized diffusion coefficient, Debye length ($\lambda_D = \sqrt{\varepsilon k_B T / 2 C_{\mathrm{bulk}} Z^2 e^2}$) and the space charge, respectively. $Pe = U_0 l_0 / D$, $Sc = \eta / \rho D_0$, and $Re = \rho U_0 l_0 / \eta$ are the Pélect number, the Schmidt number, and the Reynolds number, respectively.

The governing equations (Eq. A1-A6) are solved numerically using the finite volume method for discretization and Newton-Raphson method for the nonlinear equations generated by discretization of the Poisson-Nernst-Planck equation[2, 3]. The transient terms are treated implicitly using a three-level scheme which is second-order accuracy. Within each time step the Poisson-Nernst-Planck equations (Eq. A1-A4) and the Navier-Stokes equations (Eq. A5-A6) are solved in an iterative manner. Starting with a velocity field from previous iteration or initial condition, the Poisson-Nernst-Planck equations are solved simultaneously. The potential and ion

concentrations obtained are used to calculate electrical body force. The Navier-Stokes equations are then solved with the electrical body force to obtain the velocity field for the next iteration. The process is iterated until convergence is reached. The Navier-Stokes equations are solved by a coupled method which uses Rhie-Chow interpolation to produce an equation for pressure from the continuity equation[4, 5]. Linear algebraic equations are solved using the PETSc library which implements the Krylov-subspace method[6]. Due to the rapid change of variable near the membranes surface, mesh for the computational domain is strongly refined near the membranes using GMSH[7].

Boundary conditions are also supplied for the closure of the equations. The boundary conditions are given in Fig. A1b, where the permselective membranes are assumed to be impermeable to co-ions, and allow counter-ions to pass through at a constant concentration ($C_m = 2C_0$); a pressure gradient is applied between the inlet and the outlet to drive the incoming Hagen-Poiseuille flow with a parabolic velocity profile (U_{HP}: average speed). The common no-slip boundary condition for fluid flow is also enforced at the membrane surfaces.

In this computation, the dimensionless Debye length employed is smaller than that of the experiment; however, we did not use the usual simplifying assumption of the thin Debye layer limit. Instead, the ion concentrations, potential and fluid flow at all voltage biases (Ohmic, limiting and overlimiting regimes) were directly obtained by solving the full set of nonlinear and coupled governing equations (Poisson-Nernst-Planck and Navier-Stokes), and with the no-slip boundary conditions. The slip condition (second-kind electroosmosis) introduced by Rubinstein and Zaltzman[8] is only applicable in overlimiting current regime; this methodology is therefore not useful to predict the threshold voltage of transition between limiting and overlimiting regimes. The electrolyte solution is sodium chloride (NaCl) which can fully disassociate into Na^+

and Cl^- ions in the aqueous solution. Parameters used in this study are given in Table A1.

Table A1. Parameters used for simulation

Symbol	Description	Value
T	Absolute temperature	300 K
λ_D	Debye length	13.8 nm
D_+	Diffusivity of cations	$1.33\times10^{-9} m^2/s$
D_-	Diffusivity of anions	$2.03\times10^{-9} m^2/s$
C_0	Bulk concentration	0.5 mM
ϕ_0	Thermal voltage	25 mV
U_0	Velocity scale	29.66 μm
l_0	Length scale	20 μm

Current-voltage curves

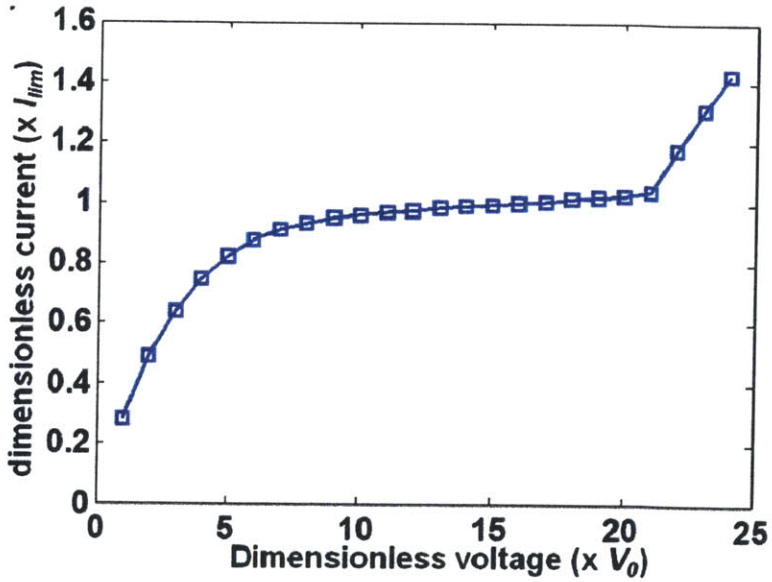

Figure A2. The current-voltage curve in the simulation ED model.

Fig. A2 shows the current-voltage (IV) curve from the simulation. Three regimes are clearly observed: Ohmic, limiting, and overlimiting regimes. The critical voltages to initiate

electroconvection (EC) is $21V_0$ (V_0=25 mV). The current is scaled with the limiting current I_{lim} in the simulation. No EC was observed on the AEM side in this simulation.

Electric field and potential drop

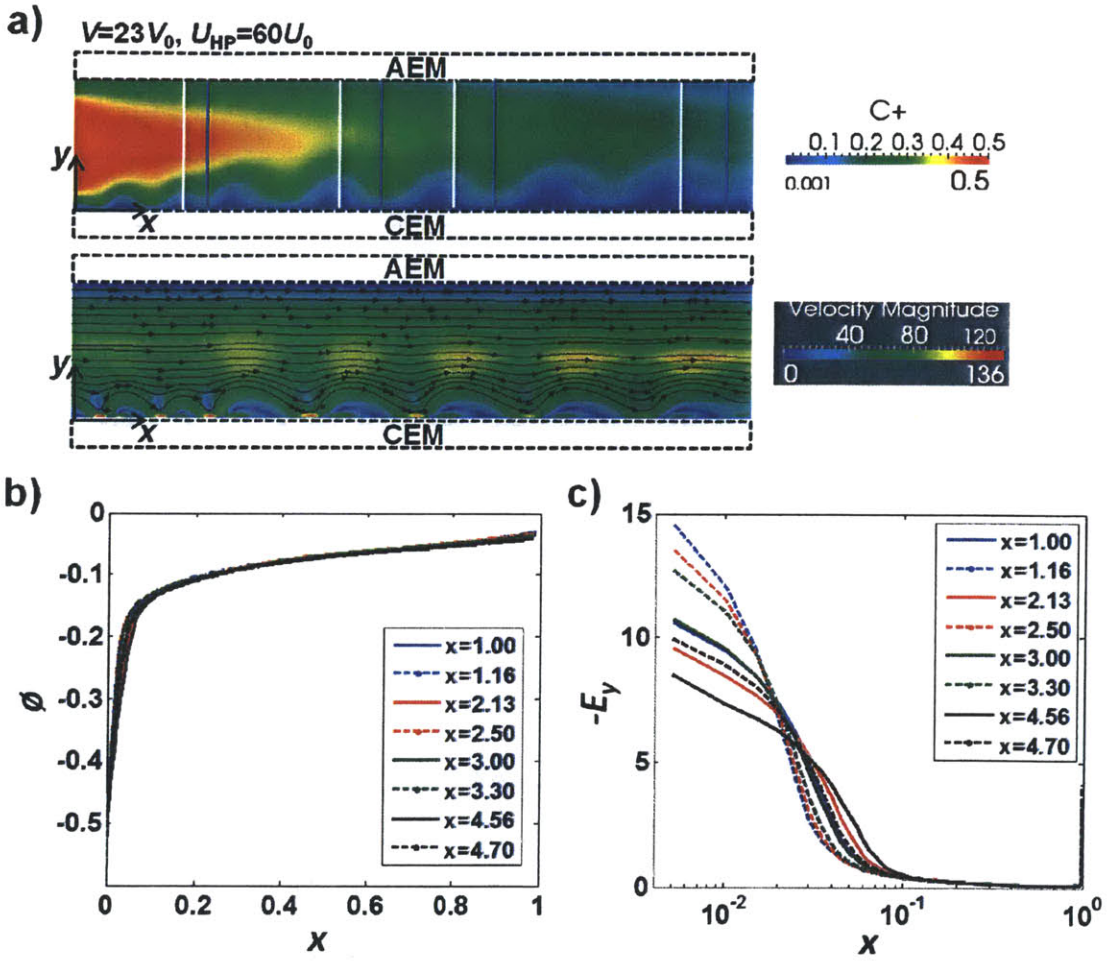

Figure A3. a) Concentration and **b)**velocity maps in the simulation model. **c)**Electric potential (ϕ) and **d)**its gradient (electric field E_y) in y-direction are plotted at the peaks (x=1, 2.13, 3, and 4.56) and the valleys (x=1.16, 2.5, 3.3, and 4.7).

From the Nernst-Plank equations for anions, $F_- = -D\nabla C_- + uC_- - \mu_- C_- \nabla\phi$, the anion flux F_-=0 and fluid velocity u=0 near the CEM surface, because of the ideal selectivity of CEM and no-slip, no-permeability conditions. Then, we obtain $(1/C_-)(\partial C_-/\partial y) \sim \partial\phi/\partial y$, which indicates that the electric field is proportional to the concentration gradient on the CEM surface (y=0); the

concentration of anion C_- would vary mainly in the y direction ($\partial\phi/\partial y \neq 0$) and be near constant in the x-direction ($\partial\phi/\partial x \approx 0$) since it would assume the lowest level[9, 10]. Fig. A3 shows the electric potential ϕ (Fig. A3c) and corresponding electric field E_y (Fig. A3d) in y-direction at eight points (x=1, 1.16, 2.13, 2.5, 3, 3.3, 4.56, 4.7) for $V = 23V_0, U = 60U_0$. The four points are on the peak of circular depletion boundary layer (white lines) and the other four points are on the valley of circular depletion boundary layer (blue lines) (Fig. A3a). As can be seen, almost all potential drop occurs within the depletion zone (0<y<0.1-0.2), which have extremely low ionic conductance (blue region in Fig. A3a). Consequently, the normal electric field near the CEM are not changed significantly, even the bulk ion concentration decreases along the channel (Fig. A3d). Instead, interestingly, the normal electric field E_y is much stronger at the valley of EC (blue line in Fig. A3a) compared with that at the peak; strong incoming flows toward the CEM by EC enhance the concentration and its gradient at the valley, while outcoming flows expand the ion depletion and increase the resistance (Fig. A3a-b). As a result, almost all ion transport (current) occurs through these valleys, with higher local field (E_y) and smaller resistance. This non-uniform ion transport was also observed in non-sheared systems[1].

The detailed derivation of the scaling law

Fluid motion in ED system is described by Stokes' equation, neglecting inertia terms and external body forces (*e.g.* gravity) except electric body force (the same equation with Eq. 1.41):

$$0 = -\nabla P + \mu\nabla^2 u + \varepsilon\nabla^2\phi\cdot\nabla\phi . \tag{A8}$$

First, when the external pressure gradient and corresponding shear flow do not occur, there

is only source to generate electroconvection, *i.e.* electric body force. Then, the height of vortex is determined by balancing the source, electric body force, and fluid viscosity:

$$\mu\nabla^2 u \sim \varepsilon\nabla^2\phi\cdot\nabla\phi\,. \tag{A9}$$

Here, the fluid velocity u will not be constant along the vortex streamline, so we apply the curl operator to obtain the vorticity w:

$$\nabla\times(\mu\nabla^2 u) \sim \nabla\times(\varepsilon\nabla^2\phi\cdot\nabla\phi), \tag{A10}$$

$$\mu\nabla^2 w \sim \nabla\times(\varepsilon\nabla^2\phi\cdot\nabla\phi). \tag{A11}$$

The vorticity is constant along the single vortex streamline; the vorticity has only z-axis direction with 2-D approximation (on xy-plane). If we assume **i)**the most voltage drop occurs in the electroconvection zone and **ii)**consider the outermost vortex and vorticity, both gradient and curl operators can be scaled by the height of electroconvection ($\nabla\sim 1/d_{ec}, \nabla\times\sim 1/d_{ec}$). As a result, Eq. A11 becomes

$$\mu\frac{w}{d_{ec}^2}\sim\varepsilon\frac{\phi^2}{d_{ec}^4}, \tag{A12}$$

and we obtain the scaling law for non-sheared electroconvection:

$$d_{ec}\sim\sqrt{\varepsilon/\mu w}\cdot\phi\,. \tag{A13}$$

Secondly, in ED system case, there are two driven forces to generate fluid motions: external pressure gradient (tangential flow) and electric body force (vortical flow). Then, the height of electroconvection is selected when these two driven forces are balanced:

$$\nabla P \sim \varepsilon \nabla^2 \phi \cdot \nabla \phi . \tag{A14}$$

The pressure gradient develops in the tangential direction, so

$$\frac{P}{L} = \varepsilon \frac{\phi^2}{d^3_{ec}} . \tag{A15}$$

From the Hagen-Poiseuille equation which describe the pressure driven tangential flow by balancing the external pressure gradient and fluid viscosity, we obtain

$$\nabla P \sim \mu \nabla^2 u , \tag{A16}$$

$$\frac{P}{L} = \frac{64 \mu U}{D_h^{\,2}} , \tag{A17}$$

where the hydrodynamic diameter of rectangular channel is $D_h = 2wh/(w+h)$. Substituting Eq. A17 into Eq. A15, the scaling law for sheared electroconvection can be obtained:

$$\frac{d_{ec}}{w} = \left[\frac{\varepsilon}{64 \mu w^3} \left(\frac{2wh}{w+h} \right)^2 \right]^{1/3} \cdot \left(\frac{\phi^2}{U} \right)^{1/3} . \tag{A18}$$

References

[1] V. S. Pham, Z. Li, K. M. Lim, J. K. White, and J. Han, Phys Rev E **86**, 046310 (2012).

[2] S. V. Patankar, and D. B. Spalding, Int J Heat Mass Tran **15**, 1787 (1972).

[3] J. H. Ferziger, and M. Peric, *Computational Methods for Fluid Dynamics* (Springer, 2001), 3rd ed. edn.

[4] C. M. Rhie, and W. L. Chow, AIAA Journal **21**, 1525 (1983).

[5] M. Darwish, I. Sraj, and F. Moukalled, J Comput Phys **228**, 180 (2009).

[6] J. B. S. Balay, K. Buschelman, V. Eijkhout, W. Gropp, D. Kaushik,, and L. C. M. M. Knepley, B. Smith, and H. Zhang, (Mathematics and Computer Science Division, Argonne National Laboratory, June 2012).

[7] C. Geuzaine, and J. F. Remacle, Int J Numer Meth Eng **79**, 1309 (2009).

[8] I. Rubinstein, and B. Zaltzman, Phys Rev E **62**, 2238 (2000).

[9] V. V. Nikonenko, N. D. Pismenskaya, E. I. Belova, P. Sistat, P. Huguet, G. Pourcelly, and C. Larchet, Adv Colloid Interfac **160**, 101 (2010).

[10] I. Rubinstein, and B. Zaltzman, Adv Colloid Interfac **159**, 117 (2010).

Chapter 4

Scalable, Single-Step Water Desalination and Purification using ICP

4.1. Introduction to Water Purification by ICP

Nowadays, fresh water is not any more 'free' resource of nature. Much of freshwater sources in the world today are polluted and not adequate for human consumption. A bottled of clean, purified water is currently sold at higher price than that of gasoline. Polluted drinking water creates various water-related diseases, such as anemia, arsenicosis, cholera, malaria, and lead poisoning. Various governments and water industry recognize that this water shortage problem will become worse in the coming years, and counteract by securing water-related technologies to monitor, clean, and manage water resources. The topics of major technological and societal interest on the water-energy nexus are the development of more scalable (portable), inexpensive, and efficient water purification systems to remove both salts and detrimental biological agents, including toxins, proteins, bacteria, and cells from various water sources (*e.g.* ground and brackish water, sea water, and even produced water from oil/gas industry).

When the nonlinear ICP with OLC was shown to generate wide depletion zone with extremely low salt concentration near IEMs, as described in Chapter 3, the desalting capability of nonlinear ICP has been recognized as the next-generation electrochemical desalination device. In 2010, S.J. Kim *et al.*[1] demonstrated a microfluidic desalination device by generating the strong depletion zone of nonlinear ICP under pressure-driven flow. Recently, Ali Mani *et al.*[2] and Kyle N. Knust *et al.*[3] also discussed the possibility to use SC or selective Faradic reaction in microfluidic channels for generating ICP and purified water flow. While these previous works clearly demonstrated the desalination capability of nonlinear ICP, they have three critical

challenges. First, the detailed mechanism of ICP desalination process was not quantitatively established, and the critical difference (both in terms of mechanism and performance metrics) between ICP vs. ED systems were not fully understood. This is important since ICP can also occur in standard ED systems (see Chapter 2 and 3), the fact that has not been widely appreciated previously. This lack of theoretical understanding of ICP desalination significantly limits engineering and optimization efforts. Second, the previous ICP and related platforms[1-3], while adequate as a proof of concept, had a (microfluidic) design feature that are not adequate for a high efficiency, robust desalination system. The electrodes were connected to the ICP zones with long microchannels creating unnecessary power consumption along the way. In addition, electrodes were exposed directly to the desalting flow, which allowed Faradaic reaction to affect the system performance and the quality of desalted water[1-3]. For example, chlorine ions, which is the most abundant ions in ground water, can be oxidized and disproportionated at anode, generating poisonous chlorine gas and hydrochloric acid (HCl) / hypochlorous acid (HOCl), respectively[4]. With the problems on the water quality, the additional hydrogen ion (H^+) production can worsen the energy consumption to reject those ions. The standard potential of the chlorine oxidation is only 1.39V, so corresponding pH change by its disproportionation in aqueous solutions has been observed even in capacitive deionization (CDI) operated under 2V [5]. Last, scaling-up to realistic, macroscopic system is one of the biggest huddles of such microfluidics-based platforms.

In this chapter, we demonstrate and characterize an *en bloc* desalination/purification method (removing salt ions and charged biomolecules and particles simultaneously) from brackish water by nonlinear ICP phenomenon between two identical IEMs. Through visualizing and tracing conductivity, dye concentration, and particle movement, we have demonstrated the

production of purified water by eliminating salt ions, dyes and particles. The desalting performance is not only predictable by the scaling law governing electroconvection (EC) zone height (see Chapter 3.2.2), but also stable and unaffected by Faradaic reactions at the electrodes. We quantify the enhancement of both energy and current efficiency of ICP desalination over standard ED process. In addition, we have also developed a straightforward strategy to scale up the demonstrated platform for commercialization, by stacking the unit platforms in parallel, just as in ED.

4.2. ICP Desalination Platform with Two Identical IEMs

4.2.1. Device Concept

Between two juxtaposed CEMs (termed as '2CEM'), ion depletion zone (d_{de}) and ion enrichment zone (d_{en}) are generated under an electric field (Fig. 4.1a). As cations are selectively transferred through the CEMs, anions are relocated in order to achieve electroneutrality, resulting in the concentration drop (increase) in ion depletion (enrichment) zone. The concentration drop (*i.e.* salt removal) is low and spatially gradual at relatively low voltage or current (Ohmic regime). However, at higher voltage or current (overlimiting regime), strong EC facilitates cation transport through CEMs, allowing us to "relocate" most salt ions. The depletion zone in overlimiting regime is characterized by flat and low ion concentration profile, and corresponding strong electric field, and general inhibition of charged agents (*e.g.* proteins and bacteria) entering this zone[4, 5]. As a result, we can separate and collect the desalted/purified flow from the brine flow by bifurcating the channel at the end of channel. This ICP desalination/purification also happens with two AEMs (termed as '2AEM') but the location of desalted/brine flows are reversed (Fig. 4.1b).

To clarify the difference between ICP desalination platform and ED, we also build ED system (Fig 4.1c). While cations and anions in ED can move toward the electrodes under the electric field, cations (anions) are 'imprisoned' between two AEMs (CEMs) in the ICP platform. Therefore, if the internal relocation of anion (for Fig 4.1a) or cation (for Fig 4.1b) by ICP does not happen for some reason (*e.g.* very heavy, immobilized ions), the desalted flow will not be produced. The ICP platform can be stacked just as in standard ED system, so we need to set the cell number N of the system to calculate current efficiency values. Typically, one cell in ED systems indicates one desalted and one concentrated flows regardless of the channel width (Fig. 4.2b). The corresponded one ICP cell to the one ED cell is achieved by changing the AEM (or

CEMs) to the CEM (or AEMs) in ED (Fig. 4.2a). Two systems have exactly the same parameters (desalted flow rate, number of IEMs, and device geometry), and we can compare ICP and ED methods fairly. It is noteworthy that ICP system collect two desalted and two brine flows, unlike ED system (one desalt and one brine flows)(Fig. 4.2). Here, the half regions of both ICP and ED systems are fabricated (grey dotted boxes in Fig. 4.2). The cell number for both platforms is still one (N=1), because the ion depletion zones occur equally: two depletion zones on two CEMs (or AEMs) in ICP system, and two depletion zones on one CEM and one AEM in ED. In ICP platform, the conductivities of one desalted flow on the lower CEM is gathered and gauged, but we let the other desalted flow on the upper CEM flow (Fig. 4.2a).

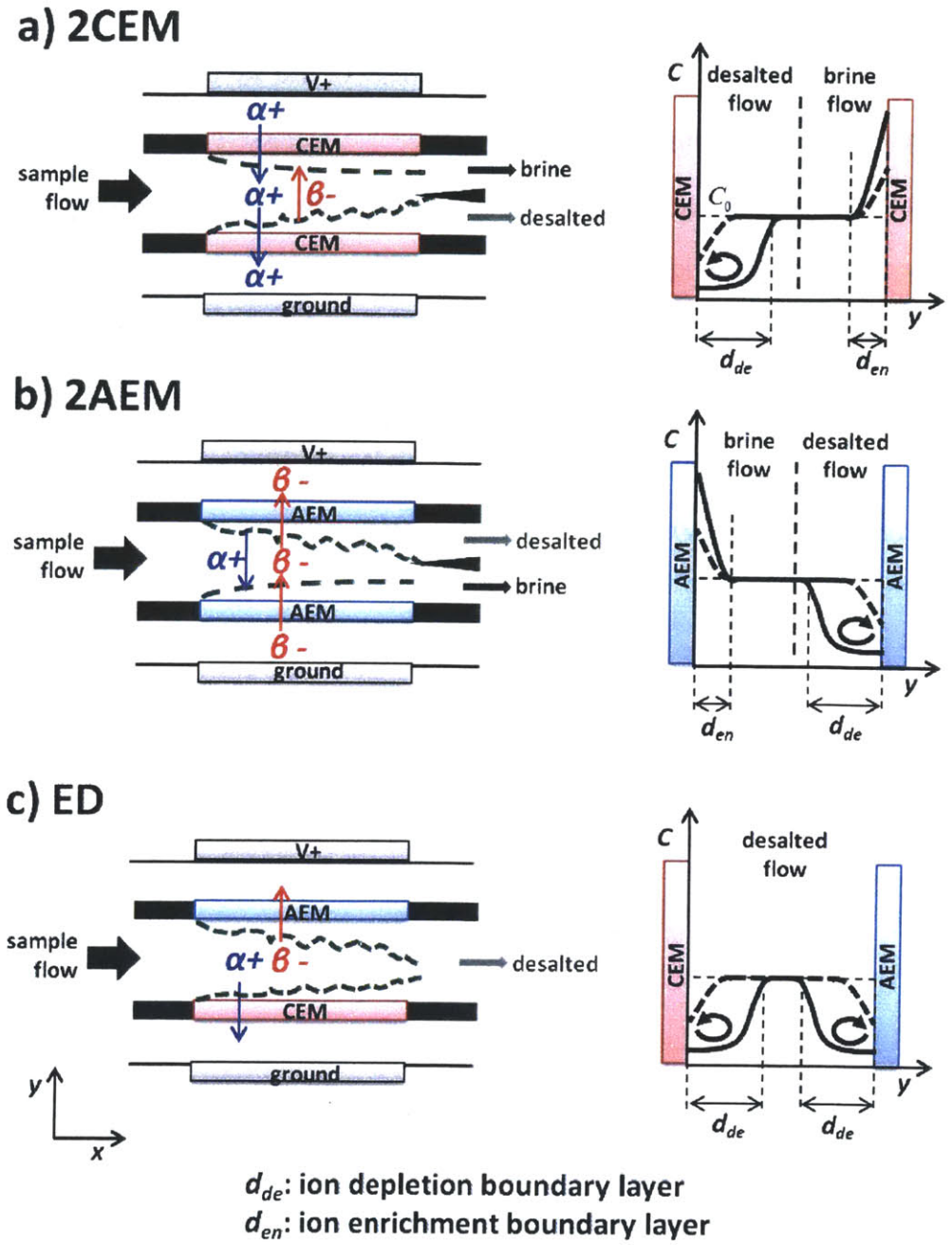

Figure 4.1 a-b) schematic figures of desalination/purification strategy utilizing ICP between two identical IEMs and **c)** comparison with ED. Two electrodes and two CEMs (or AEMs) are juxtaposed, and the channel between the two CEMs (or AEMs) is bifurcated at the end of the membranes. Blue and red arrows indicate the movement of cations α^+ and anions β^-. Ion depletion zone d_{de} with low ion concentration occurs at the anodic side of CEMs and at the cathodic side of AEMs (meandering green dotted lines in Fig. 4.1a-c). Electroconvective vortices exist in this depletion zone (solid black circles). Ion enrichment zone d_{en} with high ion concentration occur at the other side of CEMs and AEMs (curvy green dotted lines). Black (gray) block arrows on right figures indicate the corresponding brine (desalted) flow by ion enrichment (depletion) by ICP.

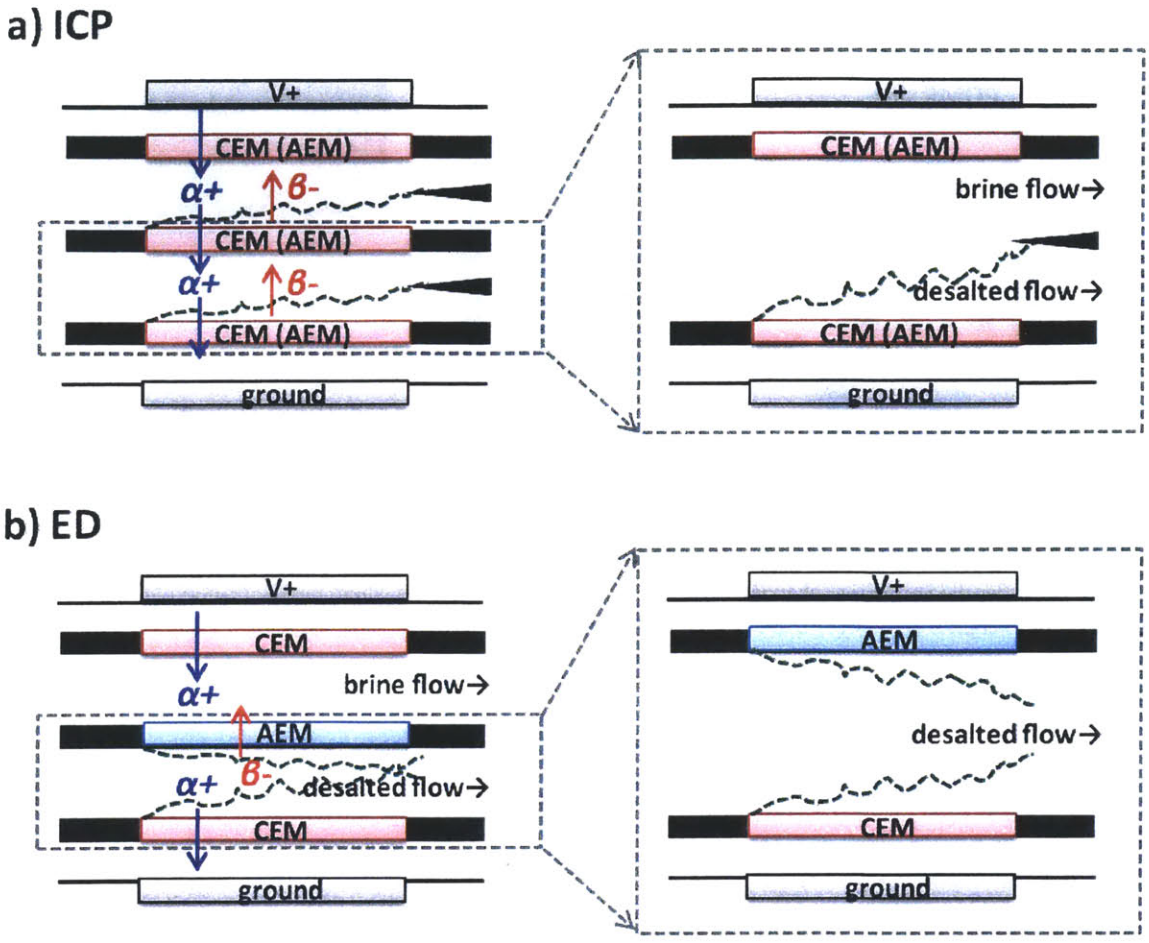

Figure 4.2 Schematic figures to compare **a)**ICP and **b)**ED platforms. To correspond the one EC cell (Fig. 4.2b), three identical IEMs constitute ICP platforms (Fig. 4.2a). In ICP system, the two channels between the three IEMs are bifurcated to collect desalted flows separately. Blue and red arrows indicate the movement of cations α^+ and anions β^-. Meandering green dotted lines are ion depletion zones on IEMs. Grey dotted boxes are the ICP and ED systems fabricated here (Fig. 4.1).

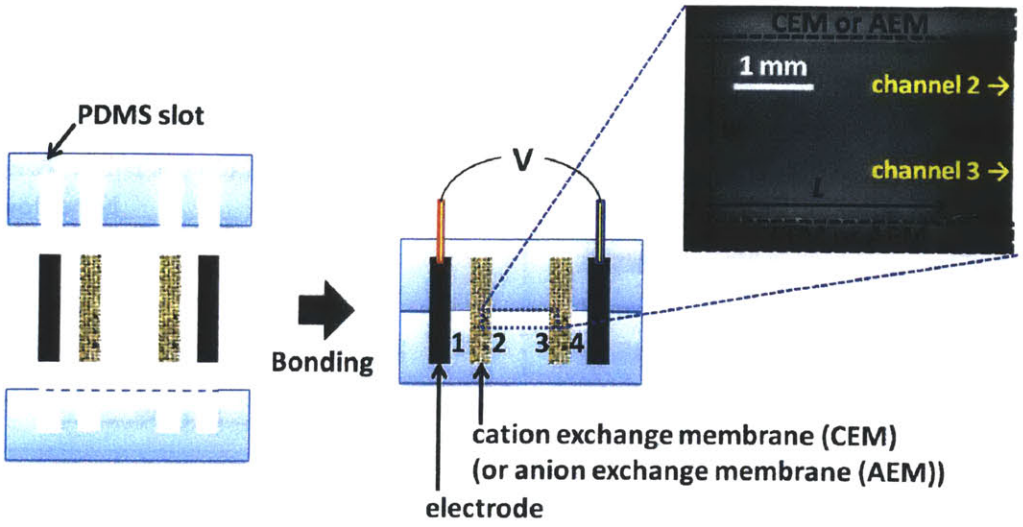

Figure 4.3. Schematic diagram of the new ICP desalination system before (left) and after assembly (right). Three channels are built between two CEMs (or AEMs) and two electrodes: one channel between two IEMs which are bifurcated as desalted and brine channels (2 and 3), and electrode channels where faradic reaction happens (1 and 4). The channel height h and length L are 0.2 and 5-10 mm, respectively. The inter-membrane distance w between two IEMs is 2 - 2.38 mm.

4.2.2. Device Fabrication, Operation, and *in situ* Visualization

To demonstrate and characterize desalination/purification of the new platform, the sample device is fabricated by slotting IEMs and electrodes into Polydimethylsiloxane (PDMS) (Fig. 4.3). In 10mM NaCl solution as a model of brackish water, the fluorescent dye, 0.78μM Alexa Fluor 488 (Invitrogen, Carlsbad, CA) or 5μM R6G, is added to visualize ICP phenomenon. Here, we use the positively charged R6G for 2AEM and the negatively charged Alexa Fluor 488 for 2CEM and ED, respectively. These dyes were selected to visualize the trapped ions between the two IEMs and ion enrichment in brine flow. Dye concentrations are relatively low, so they do not contribute to the current response yet can still represent local ion concentrations[6]. Fumasep® FTAM-E , FTCM-E (FuMA-Tech CmbH, Germany), and carbon paper (Fuel Cell Store, Inc., Boulder, CO) are used as an AEM, CEM, and electrodes respectively. The more detailed fabrication and operating procedures are same described in Chapter 2.2.

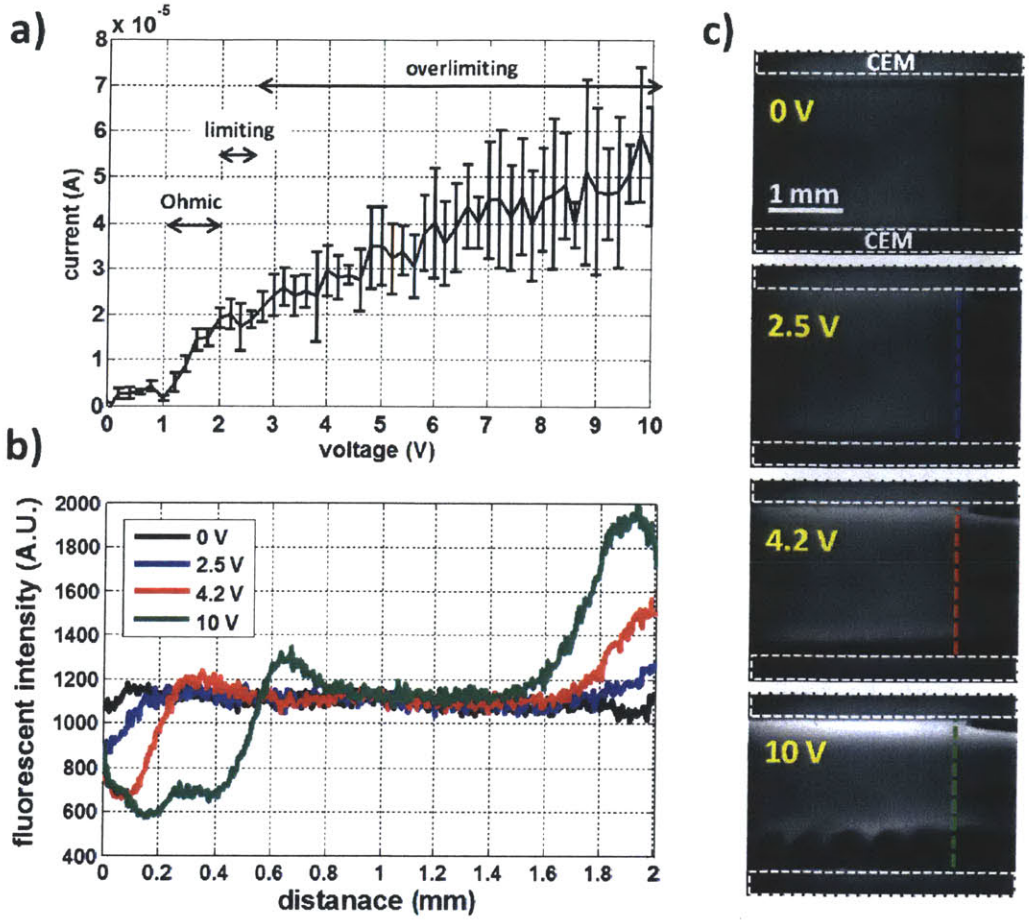

Figure 4.4 a) Current-voltage curve of the new desalination/purification platform with two CEMs. Current-voltage response is measured three times by ramping up the voltage by discrete voltage jumps of 0.2 V in every 30 seconds. **b-c**) Visualized qualitative concentration profiles right before the channel bifurcation (dotted lines in Fig. 4.4c) with 0.78μM Alexa Fluor 488. 10mM NaCl solution flows with 10μL/min flow rate. Electrodes are rinsed by 10mM dibasic buffer solution with 30μL/min flow rate. The channel width and length are 2.38 mm and 5 mm, respectively.

4.2.3. Demonstration of Brackish Water Desalination and Purification

Fig. 4.4a shows the current-voltage curves and visualized ICP with fluorescent dyes between two CEMs. Current-voltage response can be categorized as Ohmic (1-2 V), limiting (2-2.5 V) and overlimiting (>2.5 V) regimes. Higher reaction overpotential (0-1 V) is observed probably due to the use of carbon paper electrodes, as well as dibasic buffer solution as electrode rinsing solution, to suppress metal corrosion and pH changes. While the limiting regime (current

plateau) is not clearly shown in the current-voltage curve, the transition from Ohmic to overlimiting regime is clear in the curve (Fig. 4.4a) and in the visualized flow and concentration profiles (Fig. 4.4b-c), from the slope change in the I-V plot, strong fluctuation of current response, and the dark circular depletion zone by EC. As described by conventional convection-diffusion model[2], linear concentration gradients near the membranes are observed in the Ohmic regime (2.5 V in Fig. 4.4b-c). With such linear concentration changes, only small amount of ions can be rejected/relocated from the depletion region to the enrichment region. In the overlimiting regime, however, electroconvective vortices and the flat depletion zone are observed (10 V in Fig. 4.4b-c); a majority of ions are shifted from the depletion zone (dark region on the bottom CEM in Fig. 4.4c, 10V) to the enrichment zone (bright region on the top CEM in Fig. 4.4c, 10 V).

To quantify the desalting performance, we trace the conductivity of desalted and brine flows directly by connecting a flow-through conductivity probe (Microelectrode, Inc, Bedford, NH) (Fig. 4.5a). Here, we apply the constant current instead of the constant voltage to fix the amount of ion flux through the CEMs. Then, if all current comes from ion transport through IEMs ideally, the concentration drop in desalted flow should be matched with the value predicted by the applied current (*i.e.* current efficiency should be 1). In addition, the constant current operation also stabilize the amount of salt removal (*i.e.* the conductivity drop of desalted flow) of the system, because the ion flux is constant even the resistance of the system is subject to instability by vortex fluctuation or bubble generation at the electrodes. As in Fig. 4.5, the conductivity of desalted flow decreases and the brine flow conductivity increases by the same amount, as ions (both anions and cations) relocate by ICP. The desalting performance (salt rejection) improves as higher applied voltage or current; when 200μA (or 38.6 ± 5.6 V) is applied, 97% of salt ions are removed from 10mM NaCl solution. It is noted that all parameters

including current, voltage, desalt / brine conductivities, and visualized local concentration (Fig. 4.5c) reach the stable values and profiles. This indicates that the device operation is steady and stable.

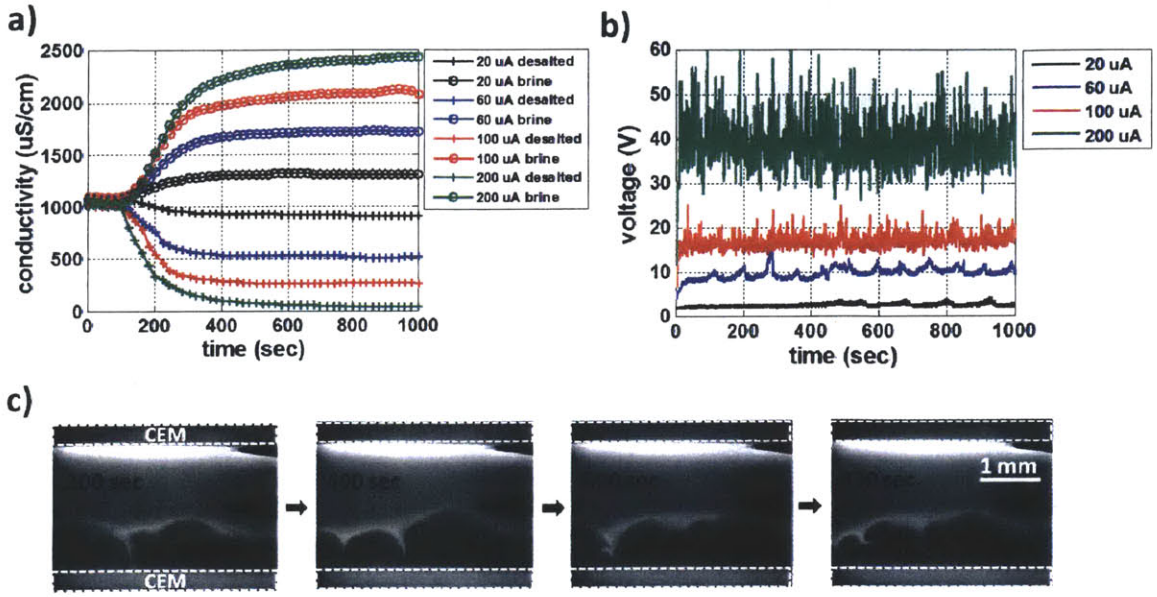

Figure 4.5 a) Conductivities of desalted and brine flows. Conductivity starts to respond after 100 sec when the desalted/brine flow reaches the conductivity probe. Although the ICP and desalting happens without time lag, the saturation of conductivities takes long (400 sec) because of relatively large volume of the conductivity probe (17 μL). **b**) Voltage-time curves at 20, 60, 100, and 200 μA. Voltage responses show 2.5±0.4, 10.1±1.0, 16.9±1.6, and 38.6±5.6 V at 20, 60, 100, and 200 μA, respectively. **c)** Local concentration profiles and strong EC on the anodic side of the lower CEM at 100 μA visualized with 0.78μM Alexa Fluor 488. The thickness of depletion zone (dark region on the lower CEM) and that of enrichment zone (bright region on the upper CEM) are nearly constant during the 1000 sec operation, even vortices show quite chaotic behavior under high applied current. 10mM NaCl solution flows with 10μL/min flow rate, and electrodes are rinsed by 10mM dibasic buffer solution with 30μL/min flow rate. The channel width and length are 2.38 mm and 5 mm, respectively.

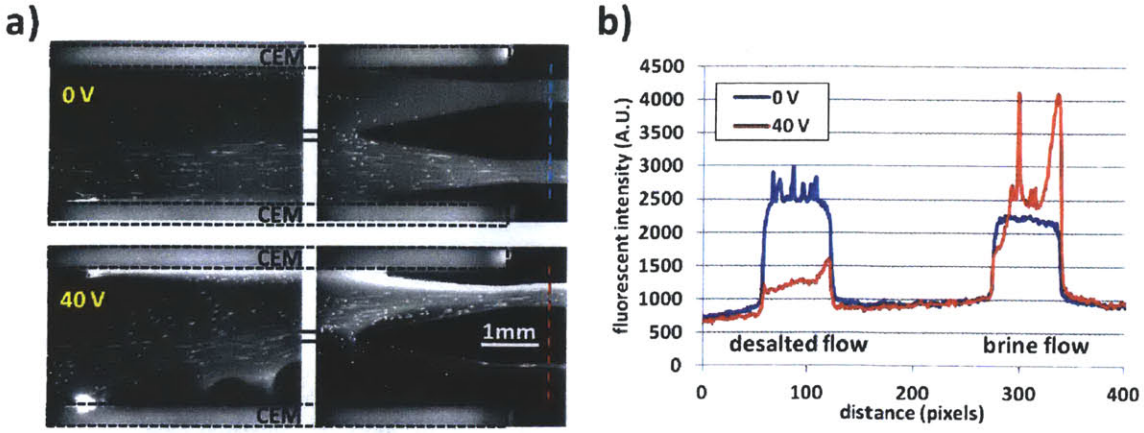

Figure 4.6 a) Fluorescent images and **b**) Fluorescent intensity curves after flow bifurcation when voltage is applied or not. Microparticles are loaded only on the lower part of the flow to visualize its movement clearly. At 40 V, the negative-charged particles move upwards, and the negatively-charged dyes also shifted upwards. As a result, dark region (low fluorescent intensity) of the desalted flow and bright region (high fluorescent intensity) of the brine flow are observed. The spikes on the fluorescent intensity curves indicate the existence of the particles. Several particles visible on the desalted channel side are the ones adsorbed to the wall of the channel, from the previous experimental runs.

The rejection of charged particles in the depletion zone of ICP has been observed continuously in previous works [1, 2, 7, 8]. To validate this rejection on the new ICP platform, we use negatively charged fluorescent dye and particle: Alexa Fluor 488 and 6 μm carboxylate microspheres (Polyscience, Inc, Warrington, PA). It is noted that bio-agents in nature are generally negatively charged (*e.g.* Escherichia coli, Salmonella, and Pseudomonas)[6]. Under sufficiently high current or voltage, the depletion zone grows enough to cover the desalted channel outlet at the bifurcated point(Fig. 4.6a). Then, most dyes and particles in the desalted flow (lower channel in Fig. 4.6a) moves toward the brine flow (upper channel in Fig. 4.6a). This shift occurs immediately after voltage or current is applied, rendering the desalted channel ion / dye / particle-free.

4.3. Characterization of Salt Removal and Energy Consumption

4.3.1. Basic Equations for Quantifying Desalination Performance

To compare ICP and ED quantitatively, we control or trace all parameters in the two systems, including current or voltage, conductivity, flow rate, device's geometry, *etc.*. We compare five performance metrics to compare the desalination performance between ED and ICP : **i)** salt removal ratio, **ii)** energy consumption, **iii)** energy per ion removal, **iv)** current efficiency, and **v)** membrane (electrode) area efficiency.

First, salt removal ratio is a parameter to indicate the desalting ability of devices. By measuring the concentration (or conductivity) of sample flows C_0 and that of the desalted flow $C_{desalted}$, we can figure out how many salt ions are removed from the desalted flow. Salt removal ratio can be given by the ratio between concentration drop and the initial ion concentration:

$$\text{Salt removal ratio} = \frac{C_0 - C_{desalted}}{C_0}. \tag{4.1}$$

The concentrations can be converted from the measured conductivity σ with given molar conductivities of electrolytes. Here, we use only dilute binary electrolytes ($z^+ = z^- = 1$), 10mM KCl, NaCl, and LiCl solutions. Then, the equation for the conversion is

$$C_i\,[mol/m^3 = mM] = \frac{\sigma}{\Lambda_{+,i} + \Lambda_{-,i}}\left[\frac{S/m}{S \cdot m^2/mol}\right], \tag{4.2}$$

where $\Lambda_{+,i}$ and $\Lambda_{-,i}$ are the molar conductivity of cation and anion. The molar conductivities of Cl^-, K^+, Na^+, Li^+ are 7.63, 7.36, 5.01, and 3.87 [10^3 Sm^2mol^{-1}], respectively, which are connected closely with their diffusivity [9].

To compare different desalination devices, energy consumption has been frequently measured. In electrochemical desalination systems, energy consumption is evaluated by the electrical power consumption (multiplication of current I and voltage V) divided by the flow rate

of desalted water Q_{desalted};

$$\text{Energy consumption} = \frac{IV}{Q_{desalted}}[Wh/L]. \tag{4.3}$$

While energy consumption is an important metric determining the economic viability of the desalination technique, it cannot represent the desalination energy efficiency of the system. We therefore consider energy consumption to remove a single ion, *i.e.* energy per ion removal, which can be obtained by dividing energy consumption by the amount of removed ions and non-dimensionalizing by thermal energy k_BT (=2.479 kJ/mol) [10]:

$$\text{Energy per ion removal} = \frac{IV/Q_{desalted}}{k_BT(C_0 - C_{desalted})}. \tag{4.4}$$

Energy per ion removal is a parameter representing how efficiently energy is consumed to reject ions by combining the concept of energy consumption and salt removal ratio. However, it is noted that salt removal ratio or the value of conductivity drop should be checked together, because better energy per ion removal does not necessarily represent better desalting performance (this issue will be discussed in Chapter 4.3.3).

As described on Eq. 2.3 in Chapter 2.4, current efficiency describes the ratio of rejected ions in desalted flow and ions transferred at the electrodes. The following equation Eq. 4.5 is a modified one to obtain current efficiency from the concentration differences of initial sample flow and desalted flow;

$$\text{current efficiency} = \frac{zFQ_{desalted}(C_0 - C_{\text{desalted}})}{NI}. \tag{4.5}$$

Last, area efficiency represents the amount of desalted ions per unit area of the working membranes or electrodes;

$$\text{Area efficiency} = \frac{C_0 - C_{desalted}}{A}[mM/m^2], \tag{4.6}$$

where A is the working area of IEMs here. The most significant cost of an electrochemical desalination system is the membrane cost, therefore higher area efficiency would be economically favorable. However, there is usually a trade-off between area efficiency and energy consumption; if one increases area efficiency to enhance salt removal ratio with a limited size device by applying higher electric potential, energy consumption will increase. If one uses a larger system for better salt rejection at a fixed voltage or current, area efficiency becomes lower.

4.3.2. Current-Voltage Responses

The three platforms described in Fig. 4.1, ICP with two CEMs (termed as '2CEM') or AEMs (termed as '2AEM') and ED, are fabricated to compare all three techniques quantitatively. The height h, width w, and length L of the working channel is 0.2, 2, and 10 mm, respectively. The area of working IEMs is therefore 2×10^{-6} m^2. Three different electrolytes (10mM KCl, NaCl, and LiCl) are used to observe the effect of asymmetric molar conductivity (or electrical mobility) of cation and anion. The flow rate between IEMs is 20μL/min, so the desalted flow rates $Q_{desalted}$ are 20μL/min; Although the desalted flow is only 10μL/min observed in ICP platforms, there is the other desalted flow on the anodic (cathodic) side of the upper CEM (lower AEM) (Fig. 4.1a-b and Fig. 4.2a). The electrodes are rinsed with the same electrolytes (KCl or NaCl or LiCl) with 30μL/min; dibasic buffer solution (previously used for more stable electrode reaction) is not used in the comparison between different salts, in order to match the ionic species across the membranes regardless of the salt used.

First of all, we measure current responses on applied voltage from 0 to 10 V to overview the ICP and ED system characteristics (Fig. 4.7). As can be seen in Fig. 4.7a, the transition from Ohmic to overlimiting regimes are clearly observed with the slope changes near 2V. Interestingly, the current-voltage curves for ED and 2CEM are almost identical (solid lines and triangles in Fig.

4.7a), but the curves for 2AEM are showing higher current than the other two. This result reveals two major characteristics of the ICP and ED platforms; the current responses are governed by either **i)** the (only) conducting ions (cations in 2CEM and anions in 2AEM), or **ii)** the slower ions (cations in ED) of the multiple conducting ions. The movement of Cl^- always governs ICP platform with two AEMs with KCl, NaCl, and LiCl solutions, since the system has only anion conductivity. This is corroborated by the observation that three curves for 2AEM are overlapping with each other, regardless of the cation species used in each experiment. The movement of cation governs 2CEM and ED (chorine ion has a higher molar conductivity than potassium, sodium, and lithium ions), and therefore showing difference in current characteristics depending on the cations used. If we place ions in the order of higher molar conductivity (proportional to electrophoretic mobility or diffusivity), it is $Cl^- > K^+ > Na^+ > Li^+$. Accordingly, in 2CEM and ED, the current values with K^+ are measured to higher than that with Na^+ and Li^+ under the same bias conditions.

The firmly confirmed phenomenon by previous linear ICP analysis is that a limiting current density is linearly proportional to the diffusivity (or molar conductivity) of conducting ions [9, 11-13]. This phenomenon is well reproduced in our experiment (Fig. 4.7b). Here, the limiting current can be selected at the location where the current-voltage curve is departing from the Ohmic characteristics [12, 14, 15].

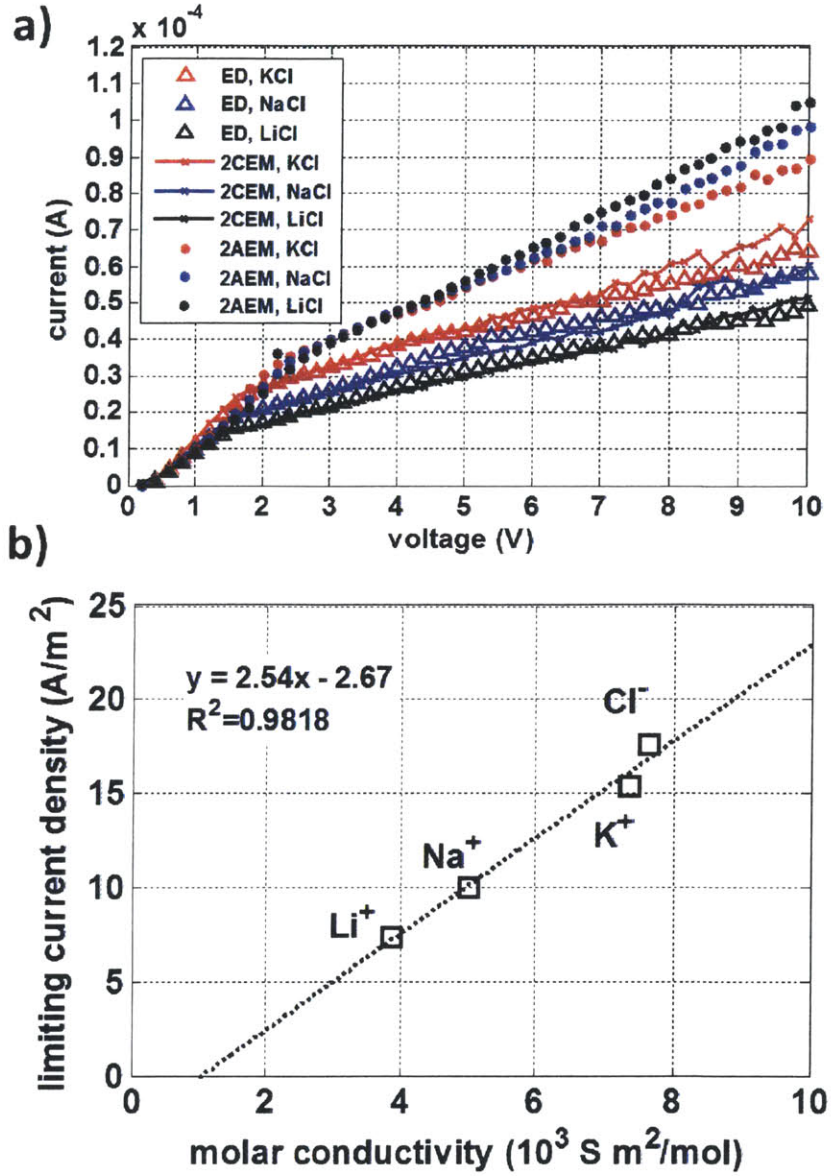

Figure 4.7 a)current-voltage curves of 2CEM, 2AEM and ED with various salts, 10mM KCl, NaCl, and LiCl. The current response are measured by ramping the voltage up with 0.2 V steps from 0 to 10 V, with 30 sec delay. **b**)limiting current density according to governing ions.

4.3.3. Desalting Performances

For the comparison of desalting performance of two types of ICP platform (2CEM, 2AEM) and ED, we record voltage responses (Fig. 4.8a-c and Fig. 4.9a-c), conductivity drop of desalted flows, and visualized ion concentration / flow profiles with fluorescent dyes during the first 300sec under a constant applied current (Ohmic regime: 5, 10 μA and overlimiting regime: 20, 30, 50, 75, 100, 150, 200 μA) and a given flow rates (20 μL/min) of various aqueous solutions with 10 mM KCl, NaCl, and LiCl. Based on the given, controlled, and measured parameters, we also obtain salt removal ratio (Fig. 4.8d-f and Fig. 4.9d-f), energy consumption (Fig. 4.10a-c and Fig. 4.11a-c), energy per ion removal (Fig. 4.10d-f and Fig. 4.11d-f), current efficiency (Fig. 4.12a-c and Fig. 4.13a-c), and area efficiency (Fig. 4.12a-c and Fig. 4.13a-c) for all data points. Most parameters have similar values in Ohmic regime (5 and 10 μA) with lower current and voltage (< 2 V), but there are clear differences in overlimiting regime among 2AEM, 2CEM and ED. This extensive dataset of three different systems with three different electrolytes reveals many interesting trends, and elucidates the differences between ICP and ED platforms under the overlimiting operating currents.

First, the voltage-current responses show the similar tendencies which described in Fig. 4.7 (Fig. 4.8a-c and Fig. 4.9a-c). Correspondingly, the energy consumptions of ED and 2CEM are matched when the same electrolyte is used (Fig. 4.10a-c). In the case of 2AEM, chlorine ions can move faster with higher molar conductivity, resulting in lower cell resistance, lower voltage responses at a given current (Fig. 4.8a-c), and lower energy consumptions (Fig. 4.10a-c) than the other two systems.

However, salt removal ratio of 2AEM are worse than both 2CEM and ED (Fig. 4.8d-f), under the same operating current; 2CEM shows larger salt removal ratio than ED (Fig. 4.8d-f), meaning that 2CEM can move more ions from the desalted flow output under the same amount

of driving current. It is noted that, with faster cation ($K^+ > Na^+ > Li^+$), the salt removal ratio for increases for 2CEM (Fig. 4.9e), and decreases for 2AEM (Fig. 4.9f). In contrast, the salt removal ratio for ED (Fig. 4.9d) is independent of the cation used. This tendency of the salt removal ratio at a constant applied current is also shown in the current efficiency (Fig. 4.12a-c and Fig. 4.13a-c). The current efficiency of 2CEM (2AEM) is always better (worse) than ED, and the trend is magnified the cation molar conductivity is lower (this phenomenon will be discussed in detail in the section 4.3.4). Current efficiency in low current regime might be not accurate, for the measurement error in conductivity can be probably magnified by the small denominator in Eq. 4.5(*i.e.* current)(grey regimes in Fig. 4.12a-c and Fig. 4.13a-c).

Energy per ion removal represents the combined efficiency of both energy consumption and salt removal (Fig. 4.10d-f and Fig. 4.11d-f). Energy per ion removal of 2AEM have lowest values (Fig. 4.10d-f), as well as in energy consumption (Fig. 4.10a-c). However, energy per ion removal of 2CEM becomes better than that of ED (Fig. 4.10d-f). It is because of higher salt removal ratio of 2CEM and that of ED (Fig. 4.8d-f), even the energy consumption are the same for 2CEM and ED (Fig 4.10a-c). In all three systems, conducting slower ions (Li^+) require more energy than faster ions (K^+ and Na^+) (Fig. 4.11d-f). Energy per ion removal in overlimiting regime is typically around $\sim 10^3 k_B T$, but it becomes $\sim 10 k_B T$ in Ohmic regime, which is comparable with state-of-the-art CDI systems[10]. While the operation in Ohmic regime (applied current < 20μA) shows better energy efficiency (*i.e.* energy per ion removal) (Fig. 4.10d-f and Fig. 4.11d-f), the area efficiency is significantly lower (Fig. 4.12d-f and Fig. 4.13d-f). This enlightens us about the trade-off in optimization of desalting processes; better energy per ion removal and worse area efficiency (*e.g.* CDI or Ohmic ED), or higher salt removal ratio and area efficiency but worse energy per ion removal (*e.g.* nonlinear ED or ICP). The former is ideal for

achieving the maximum energy efficiency, but challenging to deal with large amount of salts (high salinity feed water). The latter can handle high salinity feed water (due to high salt removal ratio) and the system size can be minimized, at the cost of higher energy expense per ions removed.

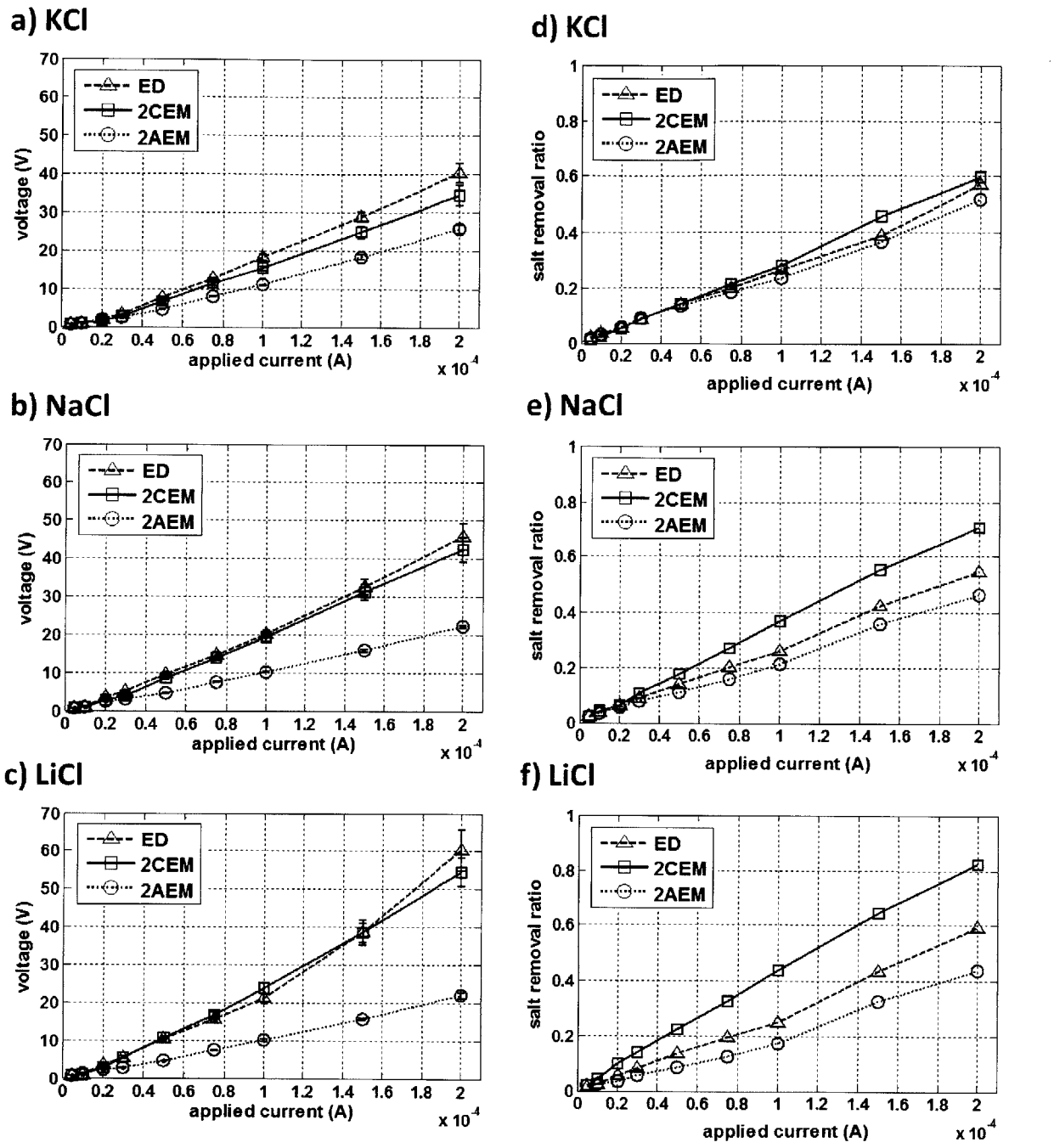

Figure 4.8 a-c) Voltage responses when the constant current is applied, and **d-f)** Salt removal ratio of 2CEM, 2AEM and ED, according to the electrolytes, KCl, NaCl, and LiCl. Voltage responses are measured during 300 sec operation at a constant applied current, and conductivity drops of desalted flows are measured at the end of 300 sec operation after the conductivity value is saturated. Salt removal ratio is calculated with Eq. 4.1-4.2. 2CEM and 2AEM indicate ICP platforms with two CEMs and AEMs, respectively.

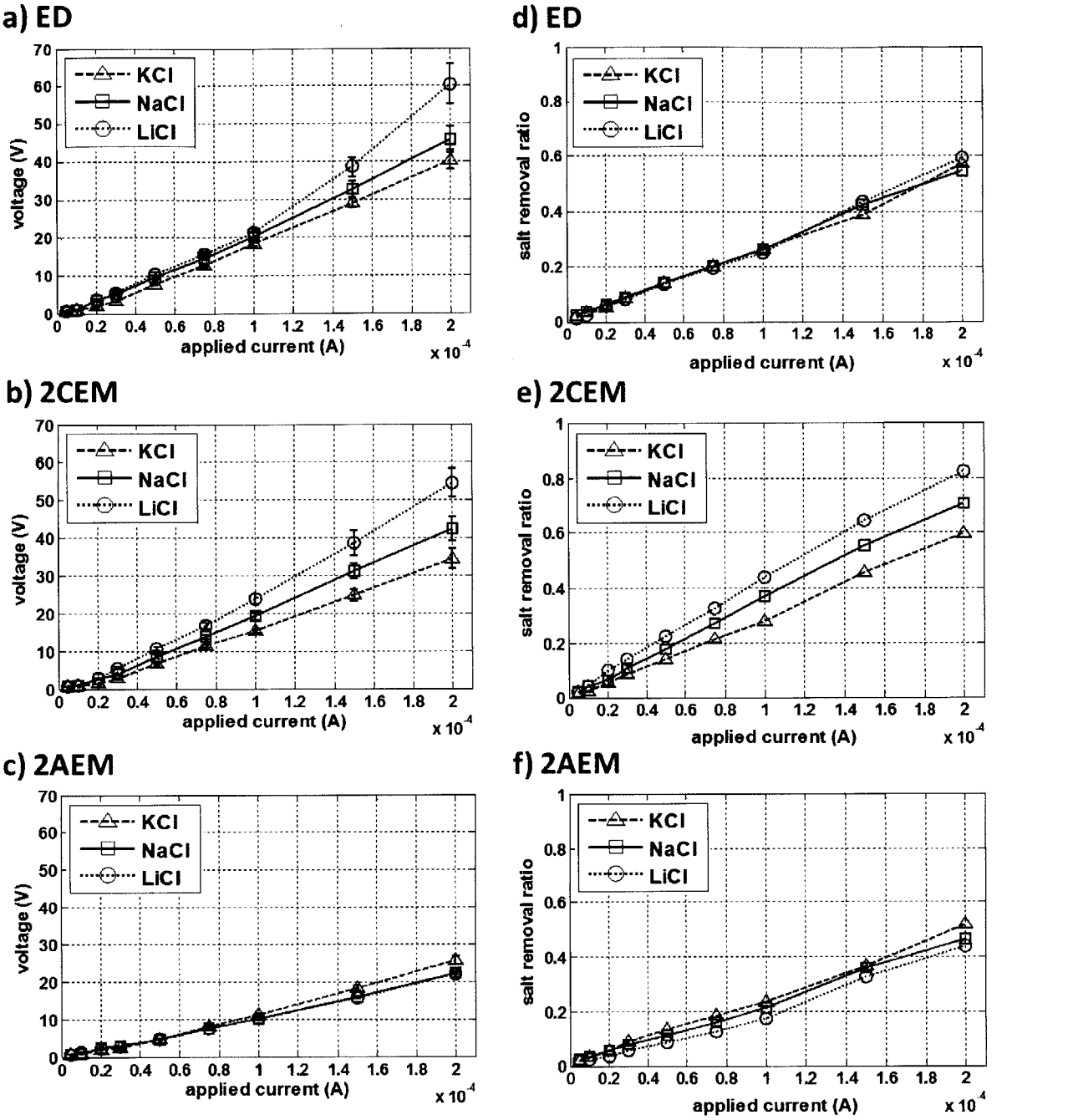

Figure 4.9 a-c) Voltage responses when the constant current is applied, and **d-f)** Salt removal ratio of two types of ICP platform (2CEM, 2AEM) and ED, according to the systems, ED, 2CEM and 2AEM. Voltage responses are measured during 300 sec operation at a constant applied current, and conductivity drops of desalted flows are measured at the end of 300 sec operation after the conductivity value is saturated. Salt removal ratio is calculated with Eq. 4.1-4.2.

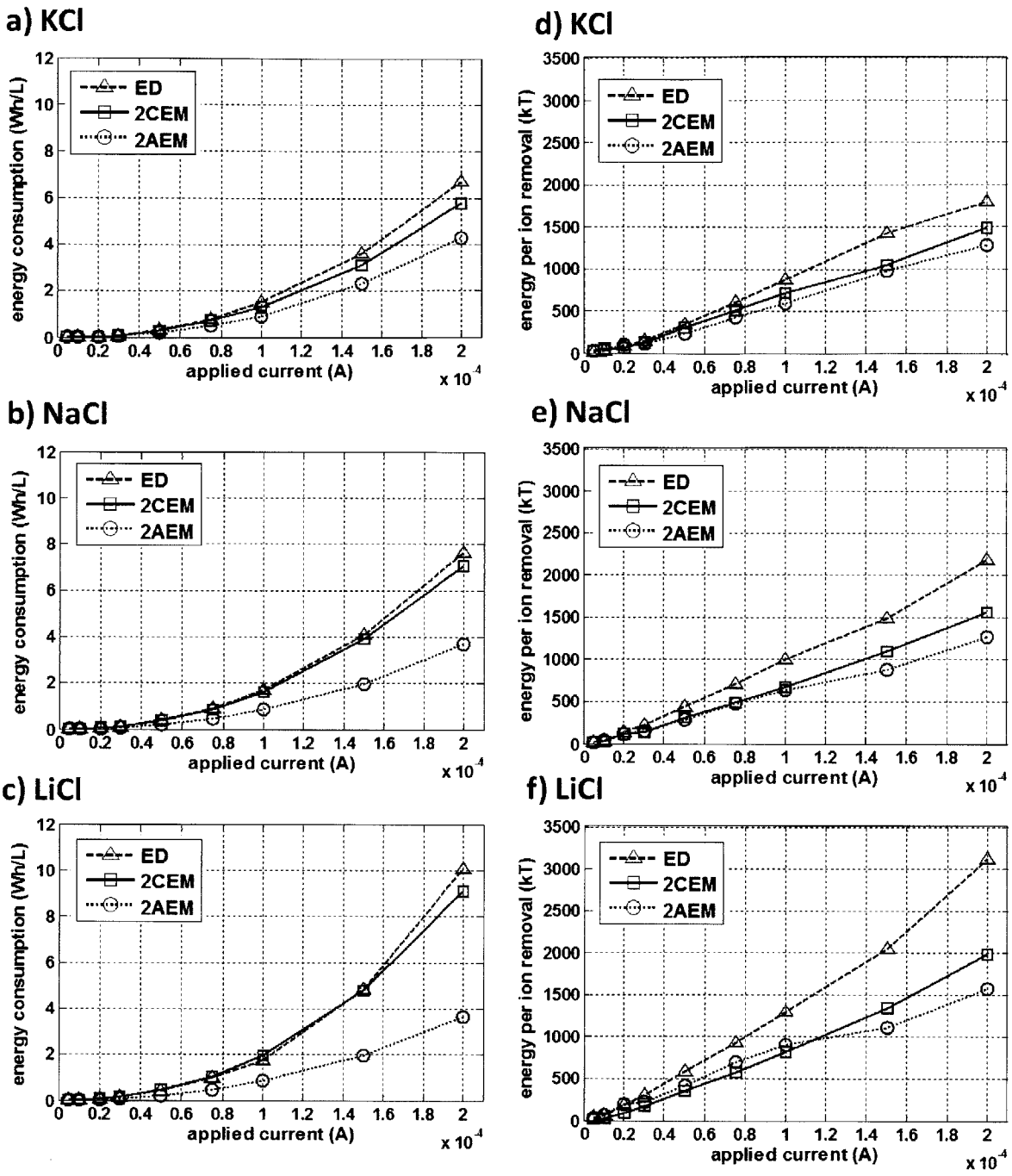

Figure 4.10 a-c) Energy consumption and **d-f)** energy per ion removal of 2CEM, 2AEM, and ED, according to the electrolytes, KCl, NaCl, and LiCl. Two metrics are calculated with Eq. 4.3-4.4.

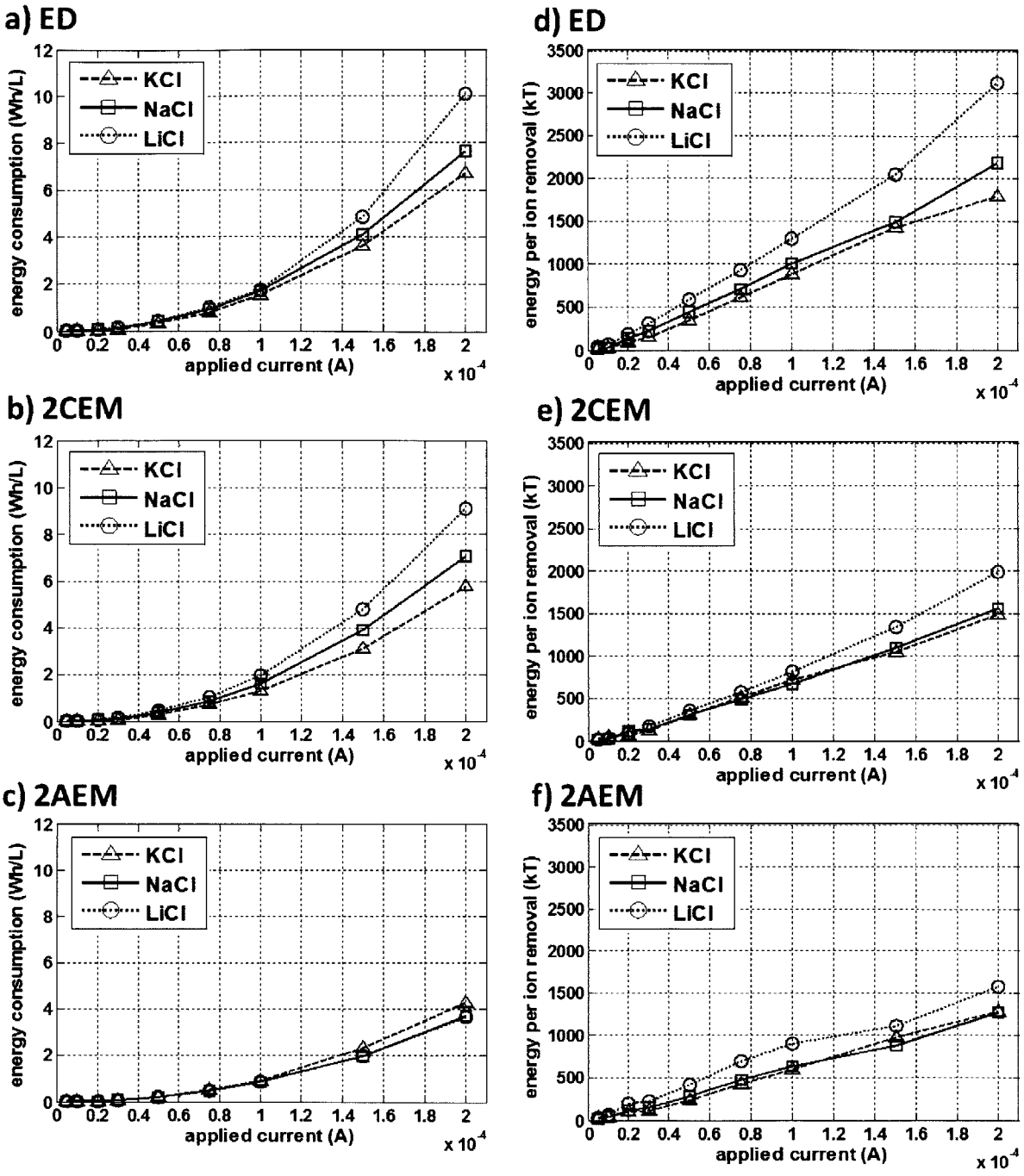

Figure 4.11 a-c) Energy consumption and **d-f)** energy per ion removal of 2CEM, 2AEM and ED, according to the systems, ED, 2CEM, and 2AEM. Two metrics are calculated with Eq. 4.3-4.4.

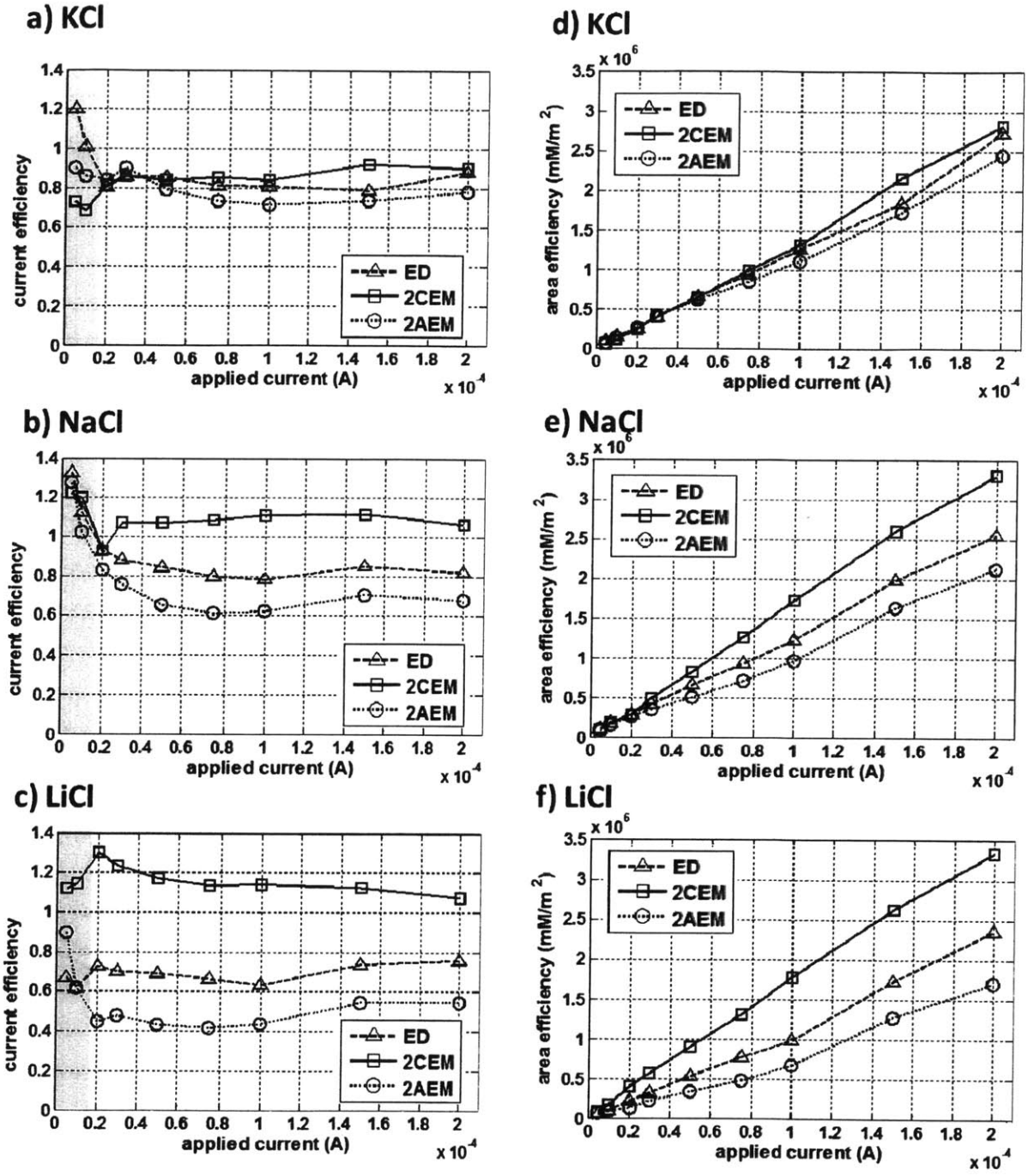

Figure 4.12 a-c) Current efficiency and **d-f)** area efficiency of 2CEM, 2AEM and ED, according to the electrolytes, KCl, NaCl, and LiCl. Two metrics are calculated with Eq. 4.5-4.6.

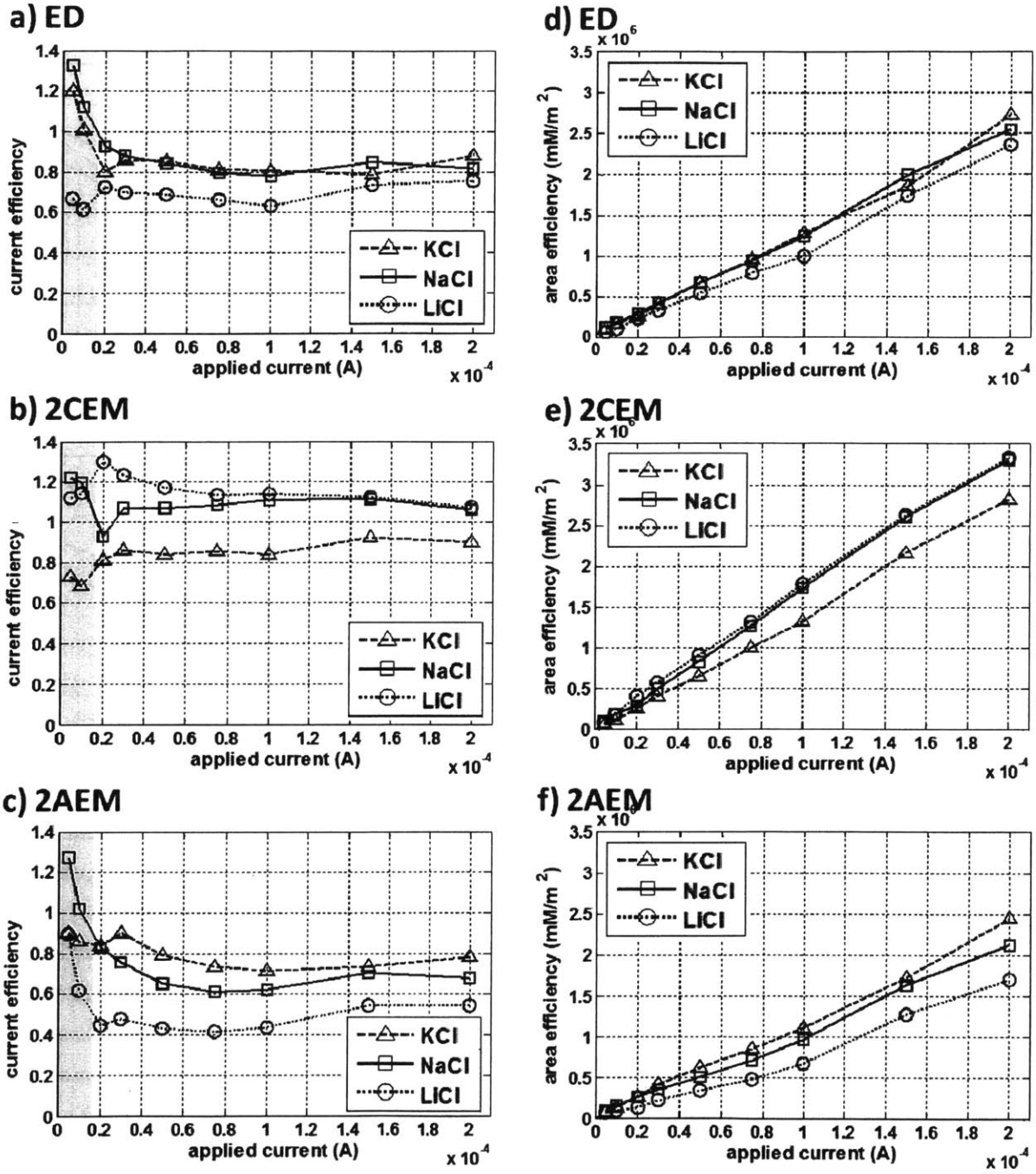

Figure 4.13 a-c) Current efficiency and **d-f)** area efficiency of two types of ICP platforms (2CEM, 2AEM) and ED, according to the systems, ED, 2CEM, and 2AEM. Two metrics are calculated with Eq. 4.5-4.6.

4.3.4. Shift in Salt Removal Ratio and Current Efficiency

As discussed in the previous section, current - voltage responses in ICP and ED platforms with various salts can be largely expected from the linear and nonlinear ICP model from the previous chapters (Chapter 3). However, the trend of the salt removal ratio (Fig. 4.8d-f and Fig. 4.9d-f) is exponible for deeper understanding of ion transport in ICP desalination process, along with energy per ion removal and current efficiency.

Fig. 4.14a shows the discrepancy of salt removal ratio between ICP platforms and ED. While there is no discrepancy in the Ohmic regime (< 20μA), the salt removal ratio shifts up (down) for 2CEM (2AEM), as the molar conductivity of cation is lowered. In fact, current efficiency can be larger than 1 for 2CEM (as mentioned in previous section, the current efficiency values in the Ohmic regime is not reliable and should not given too much consideration, due to inherent measurement errors). One possible explanation for this rather surprising result is cation-anion interaction (co-location) enabled by strong electric field and EC generated in the system, which returns the system back to electroneutrality. When an electric field is applied, conducting ions (cation on CEMs and anion on AEMs) and relocating (non-conducting) ions (anion on CEMs and cation on AEMs) move towards the opposite directions, with non-conducting ions eventually blocked by the membrane and forming the enrichment zone there. At the close vicinity of anodic (cathodic) side of CEMs (AEMs), an extended space charge layer (ESC) can be developed as a result of carrier mismatch. In the bulk solution, however, electroneutrality condition will be maintained, and the faster ion drags the slower ion toward the direction of the faster ion movement (Fig. 4.15). Then, the amount of rejected ions in desalted flow (or ion depletion zone) increases if the relocating (non-conducting) ion is faster (higher electrophoretic mobility / molar conductivity) as in 2CEM (Fig. 4.15a). If the conducting ion is faster, it drags the relocating ions to suppress depletion zone and decreases salt removal ratio as

in 2AEM (Fig. 4.15b). While this phenomenon could also occur in the ED systems (on each sides of the membrane), the enhancement and suppression occurs on the different IEMs at the same time, canceling each other. To check this hypothesis, we draw the discrepancy of current efficiency between ICP platforms and ED according to the molar conductivity ratio, which is given by

$$\text{Molar conductivity ratio} = \frac{\Lambda_i \text{ of relocating ion}}{\Lambda_i \text{ of conducting ion}} \quad . \tag{4.7}$$

The current efficiency shift of ICP platform from ED shows strong dependency on molar conductivity ratio, which supports our hypothesis (Fig. 4.14b).

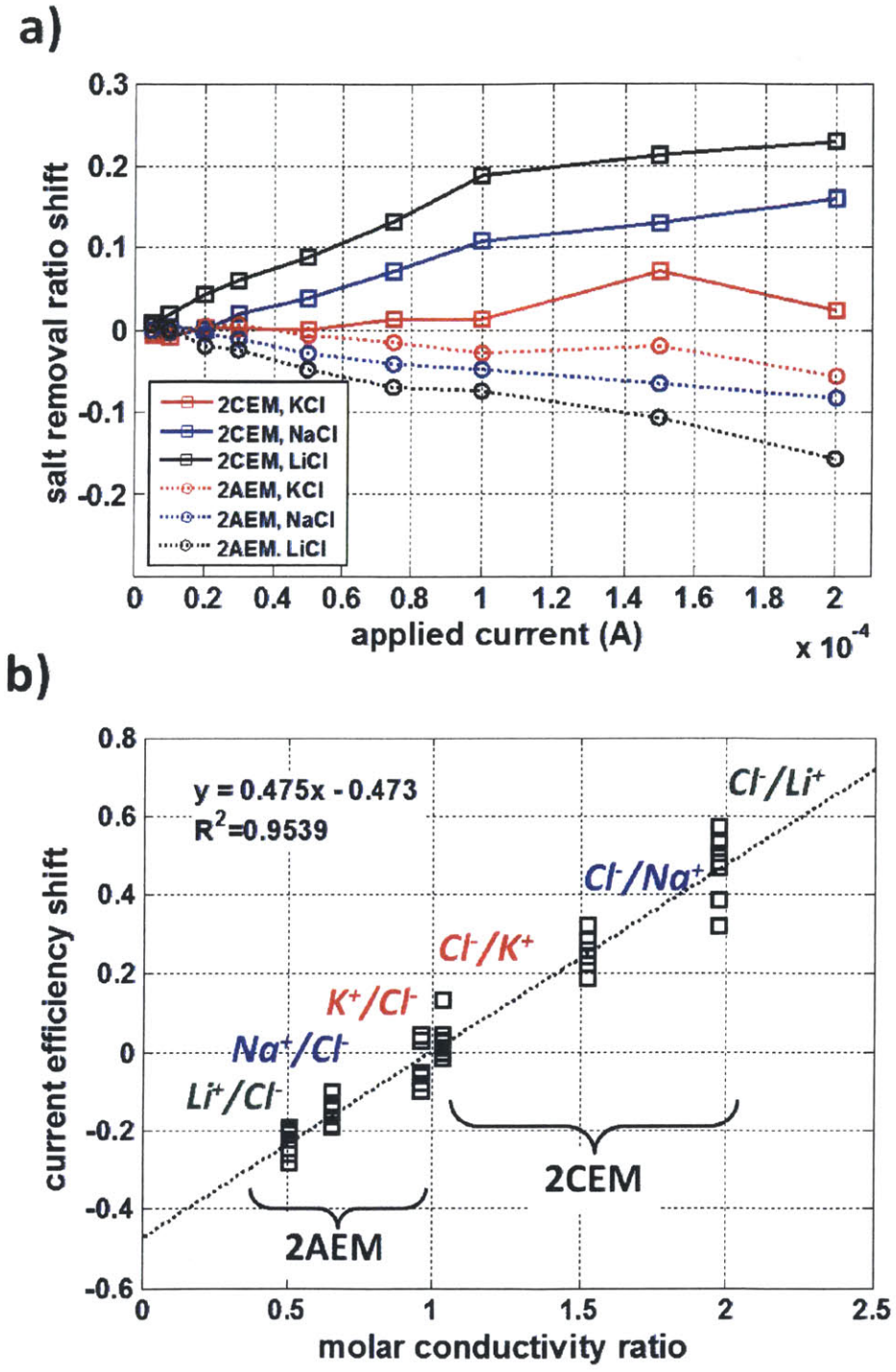

Figure 4.14 a) Shift of the salt removal ratios and **b)** shift of current efficiency of two ICP platforms (2CEM, 2AEM) from that of ED. 2CEM and 2AEM indicate ICP platforms with two CEMs and AEMs, respectively.

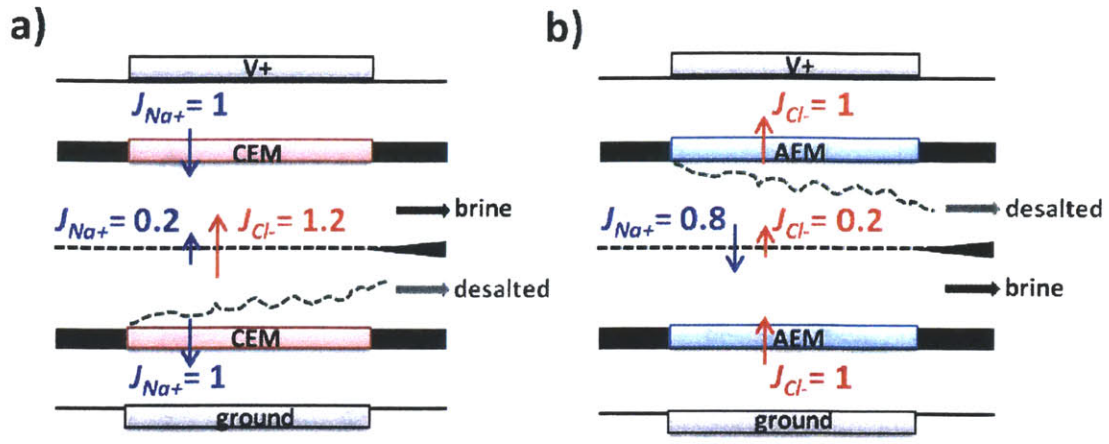

Figure 4.15 Mechanism of current efficiency shift. When molar conductivity ratio>1, *e. g.* NaCl in 2CEM in Fig. 4.15a, chlorine ions drag '0.2' sodium ions from desalted flow, resulting 20% enhancement of current efficiency (current is '1'). When molar conductivity ratio <1, *e. g.* NaCl in 2AEM in Fig. 4.15b, chlorine ion holds '0.2' sodium ions in desalted flow, resulting 20% decrease of current efficiency(current is '1').

4.3.5. Scaling Law for Salt Removal Ratio

With the scaling law for the height of sheared EC (Eq. 3.1 in Chapter 3.2.2), we easily can predict the salt removal ratio in overlimiting regime. Because the most ions are rejected or relocated from the depletion zone (or EC zone) resulting in flat, low ion concentration therein, the height of EC roughly represents the degree of salt removal occurring in the system. Fig. 4.16 compares the measured salt removal ratio of 2CEM, 2AEM, and ED systems with theoretical values of electroconvection zone height (d_{ec}), based on the scaling from Chapter 3. As one can see, all data points, obtained with three different platforms (2CEM, 2AEM, and ED) and three different kinds of electrolytes (NaCl, KCl, and LiCl), collapse into two separate lines (one for ICP, another for ED). The scaling constant C, which is determined by structural parameters only, for all cases is 3.93×10^{-3}. There are two notable points : **i)** trend is consistent regardless of the electrolyte species or molar conductivity ratio and **ii)** steeper slope of ICP platforms than that of ED. The former can be expected from Eq. 3.1 (Chapter 3.2.2), where the scaling relation is

independent of the ion molar conductivity (or mobility). About the latter, the resulting salt removal ratio of ED is well fitted to the slope of 1. Interestingly, however, the slope becomes higher about 1.4 times for ICP techniques (both for 2AEM and 2CEM cases). This indicates that the more ions can be removed, at a given set of channel geometry, operating voltage, and flow velocity values, by ICP platform (either 2AEM or 2CEM) compared with ED. This advantage of ICP platform from ED is presumably coming from controlling the conducting ions by using only one type of IEMs. Yet, further theoretical modeling and study would be required to fully understand and optimize this methodologies.

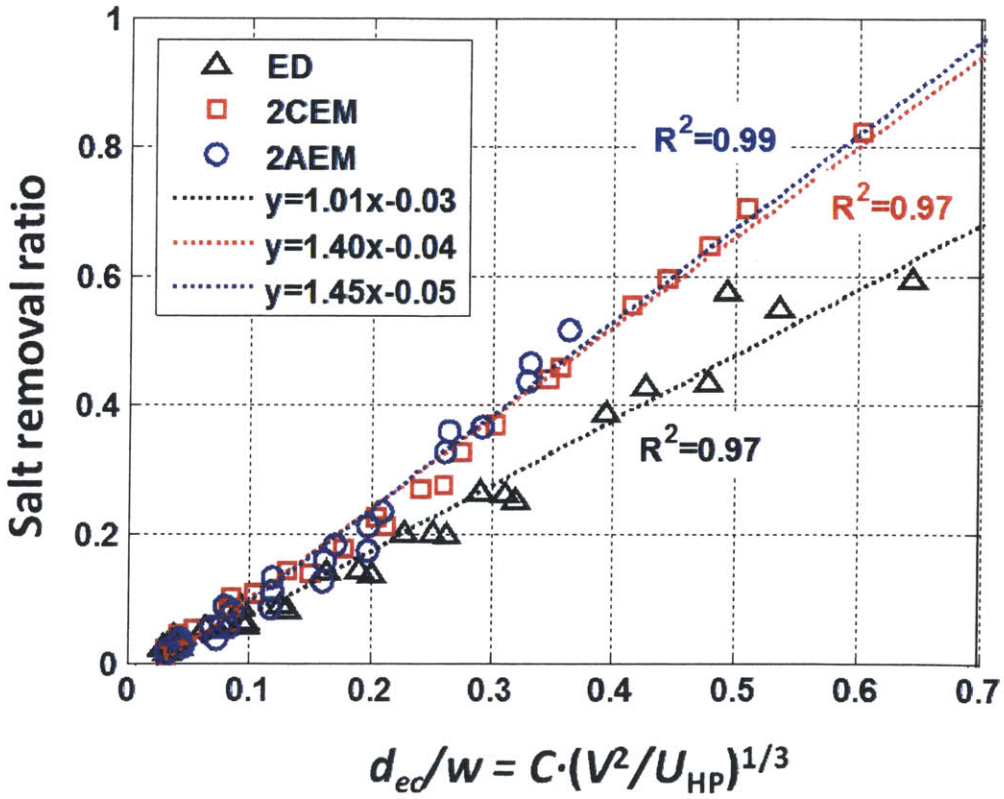

Figure 4.16. Salt removal ratio according to the height of sheared EC. The height is calculated with the scaling law, Eq. 3.1 described in Chapter 3.2.2.

4.4 Scale-up Strategy

Although the volume scale-up is one of the biggest huddles of the various microfluidic platform for commercialization, the demonstrated technology here can be scaled-up in a straightforward manner. We can stack the unit system to achieve high flow rates (Fig. 4.17). It is possible because the new ICP desalination platform here has a symmetrical and reciprocal design, like ED system. In fact, one can potentially use the existing ED platform and modify it into ICP desalination system (using CEMs), by simply removing all the AEMs yet keeping all the fluid routing. Therefore, this will make the technology quite attractive to companies already manufacturing ED systems at various scales. We expect that the power efficiency of the system will be slightly better (20~30%) than that of comparable ED, as demonstrated in the previous section. We also note that the prototype device used in this work has a shallow channel depth of 0.2mm, which can treat up to 20 μL/min (at 10mM salt concentration). Therefore, for example, if we modify a commercial handheld ED system (25 cell pairs, active membrane area: 64 cm^2, intermembrane discance: 1 mm, and the total device dimensions 165x150x190mm^3, weight: 3 kg, ED64004, PCCell GmbH, Germany), we can potentially deal with sample waters up to 192 L per 1 hour.

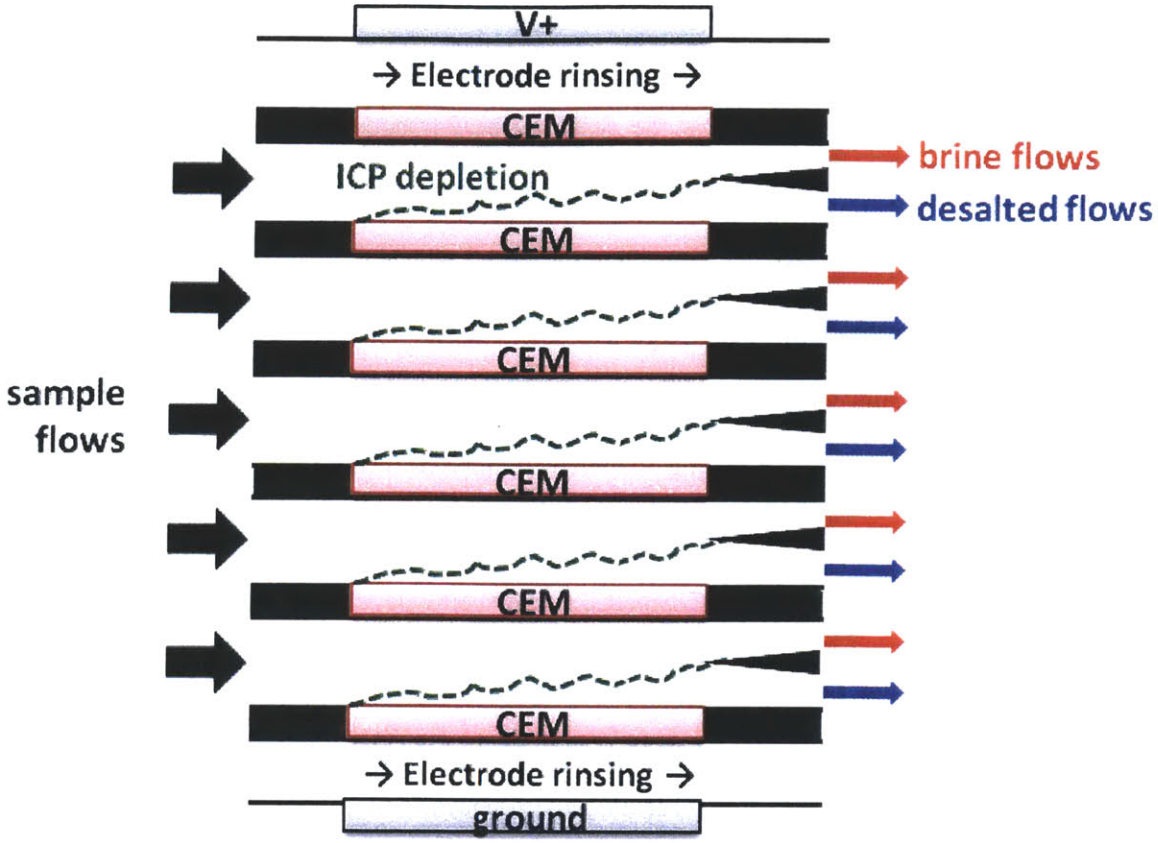

Figure 4.17 Schematic diagram of the stacked platform (5 cells) to achieve high flow rates. Green dotted lines indicate the ion depletion zones to reject ions and bio-agents. Sample flows (black thick arrows) are separated into fresh desalted/filtered flows (blue arrows) and preconcentrated/brine flows (red arrows) by ICP. Electrode rinsing solution is circulated between the CEM and electrodes.

4.5. Outlook and Future Works

In this chapter, we not only develop the robust desalination platform utilizing ICP between two identical IEMs, but also show that the desalting performance can be better than ED. ICP desalination with 2CEMs will be better than ED in terms of energy per ion removal, current efficiency and salt removal ratio. ICP desalination with 2AEMs will be better than ED in terms of overall energy consumption and energy per ion removal. We also suggest the co-location mechanism of anion and cation, as the reason for these advantages of ICP system. Although current efficiency shift is a convincing evidence of this co-location, we need to clarify this further from future theoretical and numerical studies. Multiscale, multiphysics numerical simulation model, which was used in Chapter 3, is now being developed to analyze the new ICP platforms.

Next, the remaining work to be done is expanding practical usages of this technique; for potential **i)** desalination of ultra-pure, brackish, and produced water. Essentially one can target **ii)** an *en bloc*, scalable water purifier, that can treat various types of contaminations, ranging from high concentration brine, heavy metal contaminants, and biomolecules and cells. Although several purification devices (*e.g.* LifeStraw by Vestergaard-Frandsen and HTI's (Hydration Technology Innovations) device using forward osmosis) show prominent performances, there are still some problems such as desalination performances (inability to handle high concentration brine), water capacity, and number of use (one time only or few ten days). ICP platform will be able to overcome these issues, because it can eliminate the majority of desalination targets in a continuous-flow manner, potentially without prefiltration phase. In addition, ICP platform can be combined with electrocoagulation or other purification methods to reject non-charged targets such as hydrocarbons.

Lastly, the co-location mechanism and the different transport speed for ions through

IEMs[16] may allow us to realize selective ion separation / preconcentration. Moving forward from just salt rejection or accumulation, we will be able to remove specific toxic ions (*e.g.* radioactive ions, heavy metal ions) or to squeeze useful ions (*e.g.* rare-earth metal ions).

In addition to various practical application of this new technique, further theoretical study is needed on this method, such as the consideration of overall thermodynamic efficiency (*i.e.* the comparison of ideal work (separation energy to generate brine /desalted flows) and actual work input (electric energy + pumping energy))[17]. If we can quantify the "ideality" of ion transport by current efficiency, the thermodynamic (second law) efficiency allow us to check undesirable loss of work input in overall system (*i.e.* entropy generation). Because there is no phase change process in electrochemical desalination methods, possible major sources would be undesirable ion diffusion from brine to desalted flows, Faradic reaction and Joule heating, bubble generation and corresponding additional electric resistances on electrodes.

References

[1] S. J. Kim, S. H. Ko, K. H. Kang, and J. Han, Nat Nanotechnol **5**, 297 (2010).
[2] A. Mani, and M. Bazant, Phys Rev E **84**, (2011).
[3] Kyle N. Knust, Dzmitry Hlushkou, Robbyn K. Anand, Ulrich Tallarek, and R. M. Crooks, Angew Chem-Ger Edit (DOI: 10.1002/anie.201302577).
[4] V. L. Snoeyink, and D. Jenkins, *Water Chemistry* (John Wiley & Sons, New York, 1980).
[5] J. H. Lee, W. S. Bae, and J. H. Choi, Desalination **258**, 159 (2010).
[6] R. D. Chambers, and J. G. Santiago, Analytical Chemistry **81**, 3022 (2009).
[7] R. Kwak, S. J. Kim, and J. Han, Analytical Chemistry **83**, 7348 (2011).
[8] S. J. Kim, Y. A. Song, and J. Han, Chem Soc Rev **39**, 912 (2010).
[9] R. F. Probstein, *Physicochemical Hydrodynamics: An Introduction* (Wiley-Interscience, New York, 2003), 2 edn.
[10] R. Zhao, P. M. Biesheuvel, and A. van der Wal, Energ Environ Sci **5**, 9520 (2012).
[11] J. Newman, and K. E. Thomas-Alyea, *Electrochemical Systems* (John Wiley and Sons, Inc., 2004), third Edition edn.
[12] J. H. Choi, H. J. Lee, and S. H. Moon, J Colloid Interf Sci **238**, 188 (2001).
[13] A. J. Bard, and L. R. Faulkner, *Electrochemical Methods: Fundamentals and Applications* (John Wiley and Sons, Inc., 2001), second edition edn.
[14] H. Strathmann, Desalination **264**, 268 (2010).
[15] H. J. Lee, H. Strathmann, and S. H. Moon, Desalination **190**, 43 (2006).
[16] H. L. Yeager, and A. Steck, Analytical Chemistry **51**, 862 (1979).
[17] K. H. Mistry, R. K. McGovern, G. P. Thiel, E. K. Summers, S. M. Zubair, and J. H. Lienhard, Entropy-Switz **13**, 1829 (2011).

Chapter 5

Application of ICP: Bio-agent Preconcentration[3]

5.1. Introduction to Microfluidic Bio-agent Preconcentration

Microfluidic devices for molecular detection have been extensively pursued, due to many well-documented advantages of such systems; rapid analyses, less consumption of samples and reagents, and potential for massive parallelization and automation[1, 2]. However, efficient world-to-chip interfacing, sample preparation and concentration of low-abundance analytes remain as challenges, especially for non-nucleotide targets. To achieve more sensitive detection for any given sensor platform, various sample preconcentration approaches have been developed, including isotachophoresis[3-5], electrokinetic trapping[6, 7], membrane filtration[8, 9], and ion concentration polarization[10-13]. These methods could potentially enhance the sensitivity of biological assays such as immunoassays[14] and enzyme activity assays[15]. So far, most existing biomolecule concentration devices operate by collecting or trapping low-abundance biomolecules within a small volume sample plug. While this mode of concentration is efficient in increasing the local concentration[11], it is often limited in maximum flow rate / sample volume one can process, and the integration with downstream detection steps is commonly challenging. One could avoid these problems by carrying out the detection within the plug during the ongoing concentration process[14-18], but different electric / fluidic / pH / other conditions[19] within (or near) the concentrated plug could render such *in situ* detection less desirable. Otherwise, cells could be concentrated by inertia force-based microfluidic device[20, 21], but they are not suitable for biomolecule concentrator because the size of molecules is too small to expect inertial

[3] The published journal paper (R. Kwak, S. J. Kim, and J. Han, Analytical Chemistry **83**, 7348 (2011)) was used in its entirety for Chapter 5, with minor updates and modifications. Among the authors, R. K., S. J. Kim and J. H. conceived the idea, designed the experiments, and wrote the manuscript. R. K. carried out the experiments and analyzed the data. J. H. supervised the study.

effect.

Microfluidic systems with continuous-flow operation are much better suited for such 'generic' sample preparation interface, to overcome many difficulties in microfluidic integration. For this reason, various continuous-flow biomolecule separators[22-26] have been developed for sample preparation, which requires seamless integration with downstream biosensors. However, continuous-flow concentrator for sample preconcentration has not yet been reported. Previously, the concept of continuous-flow microfluidic demixer was published, by utilizing induced charge electrokinetics in structured electrode arrays, but the concentration factor was limited (up to 2 fold)[27].

In this chapter, we have developed a continuous-flow concentrator for both biomolecules / cells, based on the nonlinear ICP initiated within a microfluidic channel coupled with a CEM. Any charged molecules can be accumulated at ion depletion boundary with appropriate tangential force field, either by an electric field or hydrodynamic pressure[28]. This system has been previously employed for enhancing immunoassays[14, 29, 30] and enzyme activity assays[15, 31]. Recently, we demonstrated that the ion depletion boundary could be controlled by changing applied electric field and hydrodynamic pressure field along the microchannel so that any charged species could flow along a specific portion of microchannel in longitudinal direction[19], which was later used to desalinate / disinfect seawater in a microfluidic device[32]. Here, we demonstrate a continuous concentration of sample analyte by controlling the position of the concentrated plug and depletion zone within a microchannel. The concentration factors up to 100 fold are achievable with biomolecules (fluorescein sodium salt, FITC-lectin (positively and negatively charged), rGFP) and cells (RBCs, and *E. coli*). The sample flow rate is reasonably high (~few μL/min) without significant limitation in downstream integration.

5.2. Microfluidic Continuous-flow Preconcentrator by ICP

5.2.1. Device Concept and Design

The ion selective material we used is Nafion, which has strong cation selectivity due to many sulfonate groups decorating hydrophobic, teflon-like polymer backbone, forming a nanometer size ion selective current pathway within the material[33]. Once voltage is applied across this cation selective membrane, ICP is triggered near the membrane. Under a static DC voltage / current bias across the membrane, ion depletion zone typically expands continuously in the microfluidic channels, eventually leading to non-steady concentration / flow profile in the system[34, 35]. However, it was shown that, by combining additional forced flow (either caused by tangential electric field or pressure gradient) with ion depletion zone formed by ICP, one can limit and control the boundary of the ion depletion zone[19, 32]. At lower flow rates, one can achieve a situation where the depletion zone is 'blocking' the entire microchannel, leading to accumulation of charged species at the boundary (stationary batch-type biomolecule concentrator). At higher flow rates, however, one can reach a condition where this boundary is partially 'burst', leading to a steady state establishment of depletion zone and flow-dominated zone co-existing[19]. This process will essentially create two parallel stream (desalted and concentrated streams) within the microfluidic channel, which was later utilized for continuous seawater desalination[32]. It came to our attention that, in the same system, the concentrated stream can also be viewed as a continuous-flow concentration system, which is the subject of this new application.

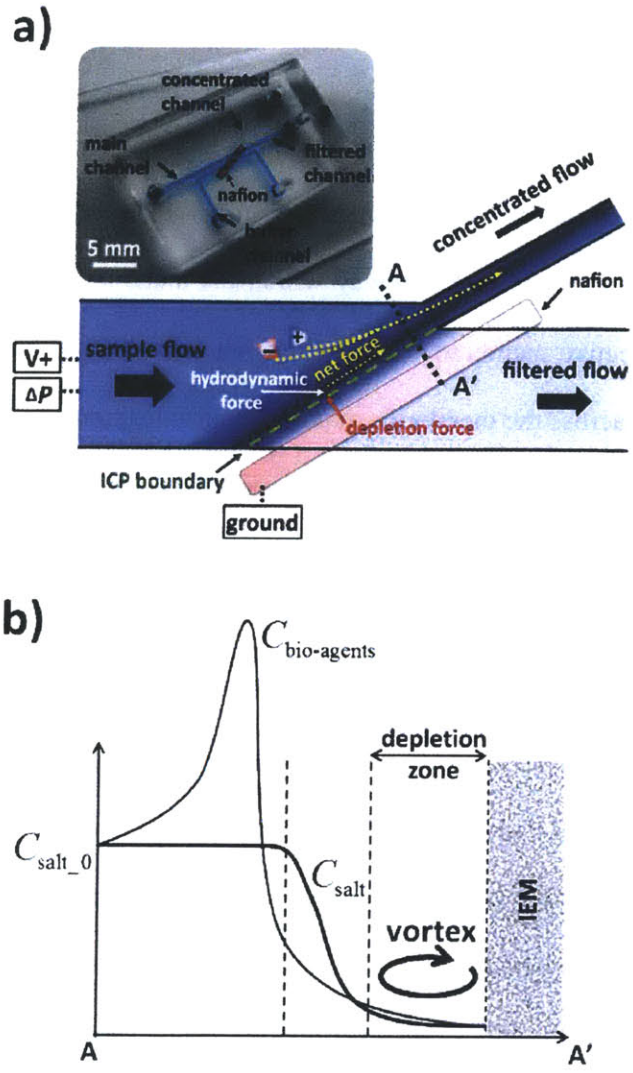

Figure 5.1 a) Schematic diagram of continuous-flow concentrator (lower) and optical image of the device (upper). On application of electric field (V+) and pressure field (ΔP), ICP zone was developed based on force balance between depletion force and hydrodynamic force. In the schematic figure, each arrow indicate the direction of hydrodynamic force (white), depletion force (red), and net force (yellow) acting on charged ions or particles. Depletion force indicates force acting on charged species as a result of ICP (ion depletion), which is electrostatic in nature. In the concentrator, ICP boundary was generated along Nafion with a specific distance, and charged species were accumulated on this boundary. Voltage (0~150V) was applied from inlet of the main channel to the buffer channel across Nafion junction. Flow rate (0~5 μL/min) was set by syringe pump. L_1 and w_1 indicate a length and a width of concentrated flow channel, and L_2 and w_2 indicate a length and a width of filtered flow channel. R_1 and R_2 indicate hydrodynamic resistances of concentrated flow and filtered flow, respectively. For experiments, the devices were fabricated with various width ratios $w' = (w_1 + w_2)/w_1$ ($w' = 10, 20, 50, 100$), and length ratios $l' = L_1/L_2$ ($l' = 0.3, 0.7, 2$). **b)** Qualitative concentration profiles of salt ions C_{salt} and bio-agents $C_{bio\text{-}agents}$ across A to A' in Fig 5.1a with the location of the depletion zone and electroconvective vortex, initiated by nonlinear ICP.

To realize continuous-flow preconcentrator, Nafion (cation exchange material) line was patterned with an angle to the main channel, as shown in Fig. 5.1a. Application of an electric field (V+) with Poiseuille flow (ΔP) would generate a controlled depletion zone near the Nafion pattern, which was used to block the stream of charged biomolecules and cells, and create concentrated plug in the sample fluid. These concentrated charged species were guided (by the external flow) into a narrower concentrated channel continuously, achieving a continuous flow of the same sample solution but with higher concentration. It is important to control the position of the concentrated plug and ion depletion zone stably in this system. The schematics of the device is similar to the desalination microfluidic system reported previously[32], with two modifications. Firstly, outlets of concentrated channel and filtered channel were electrically floated. Although an electrical voltage has been applied to one inlet and two outlets previously[32], current flows through outlets were unnecessary in this work. Secondly, Nafion was patterned in a straight line parallel to concentrated channel. Then, we were able to obtain straight ICP boundary along the Nafion pattern was generated instead of curved ICP boundary. This facilitated us to predict the shape and the position of ICP boundary and concentrated plug.

With the ideal case assumption that no charged molecules can overcome the energy barrier of depletion zone boundary, the concentration of charged molecules in the lower filtered channel would be zero. Actual electrolyte (*i.e.* majority carrier) concentration inside the depletion zone was non-zero, but minority carrier (biomolecules and cells in this study) was completely rejected by ICP so that zero concentration assumption inside depletion zone is valid[32]. Then, the concentration factor of the concentrated flow can be expressed by evaluating the ratio of flow rates of two (concentrated flow and sample flow) channels. In the case of rectangular channel with length L, width w, and height h, hydrodynamic resistant R_h and flow rate Q are as the

following[36].

$$R_{h,i} = \frac{12\mu L_i}{w_i h^3}\left[1 - \frac{h}{w_i}\left(\frac{192}{\pi^5}\sum_{n=1,3,5}^{\infty}\frac{1}{n^5}\tanh\left(\frac{n\pi w_i}{2h}\right)\right)\right]^{-1}, \tag{5.1}$$

$$Q_i = \frac{\Delta P}{R_{h,i}}. \tag{5.2}$$

Here, μ is viscosity of the solution. Flow rate Q in a channel is proportional to the applied pressure drop ΔP, and for the index i represents different channels, i =1 for concentrated channel and 2 for filtered channel. Eq. 5.1 could be linearized when a channel aspect ratio is much larger than 1 as $R_{h,i}=12\mu L_i/w_i h^3$. However, the additional viscous drag causes fluid retardation near the edges become considerable with the aspect ratio around 1, yielding the nonlinear equation Eq. 5.1[37]. By using Eq. 5.1 and 5.2, concentration factor r of the concentrated flow can be expressed as

$$r = \left(\frac{Q_1}{Q_1 + Q_2}\right)^{-1} = 1 + \frac{R_1}{R_2}. \tag{5.3}$$

We assume there is no other factor to generate additional resistance such as surface roughness, diffusion potentials, turbulences, *etc.*. In Eq. 5.1 and 5.2, ΔP, μ, and h are of constant value. Therefore, the concentration factor can be adjusted by modifying the two channel's length L and width w. In a uniform height of the system, flow rate is approximately proportional to the width of the channel, and inversely proportional to the length of the channel.

5.2.2. Device Fabrication, Operation, and Materials

The systems under the study were composed of two parallel microchannels connected by Nafion, which has high ion selectivity due to cluster network of sulfonate groups (Fig. 5.1a). We fabricated PDMS microfluidic chips with this ion selective material using previously published methods[38]. Nafion was patterned with PDMS line mold (width: 100 μm, height: 50 μm) on a clean glass substrate. Nafion® perfluorinated ion exchange resin (Sigma-Aldrich, St. Louis, MO) with 20 wt% solution was used. The Nafion-patterned glass substrate was then bonded with PDMS microchannel by means of plasma treatment. For most of test specimens (for preconcentration test of fluorescein sodium salt, rGFP, RBCs and *E. coli*), the main channel and buffer channel had dimensions of 200, 400, 1000, 2000 μm for width, 15 μm for height, and 1cm for inlet length (from inlet to bifurcated point). The width of concentrated channel has been fixed at 20 μm, so that the width ratios of concentrated channel to filtered channel are 1:10, 1:20, 1:50 and 1:100. For FITC-lectin test, in addition, the devices which had dimensions of 10 μm for width of concentrated channel, 15 μm for height also used to control the velocity of concentrated flow. The main channel had dimensions of 200 and 500 μm for width. The length of the concentrated channel and filtered channel were controlled by the location of the outlet reservoirs, ranging from 5 mm to 10 mm. PDMS molds for Nafion nanojunction patterning and the concentration microchannels were fabricated by standard photolithography[39].

The hydrodynamic pressure was generated by a syringe pump (Harvard apparatus, PHD 2200). All the experiments were imaged using an inverted epifluorescence microscope (Olympus, IX-71) with a thermoelectrically cooled CCD camera (Hamamatsu Co., Japan). Sequences of images were analyzed by Image Pro Plus 5.0 (Media Cybernetics). The DC voltage across ion selective membrane was applied with Keithley 236 current-voltage source measurement unit

(Keithley Instruments, Inc.) and high voltage DC power supplier (Stanford Research Systems, Inc., model P350) with Ag/AgCl wires (A-M Systems, Inc.). Operational voltage and pressure values were chosen between 0~150 V and 0~5 μL/min, respectively, which were adjusted to balance the depletion force (by applied voltage) and hydrodynamic force (by flow rate). The channel and interface of Nafion and PDMS would break down if the applied voltage (or electric field) is too high. In addition, we observed stronger instability under higher voltage bias. Therefore, we set the maximum voltage as 150V (150V/cm) which is ~1000 times less than the junction gap breakdown voltage of PDMS substrate (~25V/μm) [40]. With this applied voltage level between 0~150V, we optimized the experimental parameters that could provide the maximum flow rate (up to ~5 μL/min flow) and the maximum concentration factor with various width ratios $w'=(w_1+w_2)/w_1$ (= 10, 20, 50, 100), and length ratios $l'=L_1/L_2$ (= 0.3, 0.7, 2).

To demonstrate the continuous-flow concentrator, 3 pM fluorescein sodium salt (Sigma-Aldrich, St. Louis, MO) and 3 pM Green fluorescence protein (GFP) (rGFP, BD bioscience, Palo Alto, CA) were prepared in the main buffer solution, 1mM phosphate (dibasic sodium phosphate) at pH=8.7. We also prepared three different concentrations of phosphate, 1mM, 10mM, and 100mM to measure the concentration factors with various ionic strength conditions. 5 μg/mL fluorescein isothiocyanate (FITC) conjugated lectin from Lens culinaris (lentil) (FITC-lectin) (Sigma-Aldrich, St. Louis, MO) was used to show the effect of different surface charge polarities of target sample. Under 1mM phosphate (dibasic sodium phosphate) at pH=8.7 and 1mM phosphate at pH=7.4, FITC-lectin (MW ~49 kDa, isoelectric point (pI (characteristic pH value at which proteins exhibit zero net charge) ~8.0–8.8) has different surface charge polarities. Average zeta potentials (electric motilities) of FITC-lectin were −18.8 mV (-1.464×10^{-8} $m^2/V \cdot s$) at pH 8.7 and 3.35 mV (0.263×10^{-8} $m^2/V \cdot s$) at pH 7.4 respectively (measured by Zetasizer nano ZS,

Malvern). In experiments, 0.1 % Bovine serum albumin (BSA) (Sigma-Aldrich, St. Louis, MO) was added into 1mM phosphate at pH 7.4 for preventing non-specific binding. Human whole blood with red blood cells (RBCs) (Hoechst, 2000x dilution, Innovative Research) and *E. coli* ER2738 (New England BioLabs Inc.) were used to show the potential of the application for various biosamples. Human whole blood was diluted 200~500 times again using 1x phosphate buffered saline (PBS, ~150mM) solution. 0.2% Pluronic® F108 (BASF, Cumberland, RI) was added to reduce osmosis hemolysis, non-specific binding and aggregation. White blood cells (WBCs) and other blood cells were not removed from the whole blood, because the density of WBCs is much lower than the density of RBCs, and their presence did not affect the concentration behavior. 3μM Cell Tracker Orange CMRA (Molecular Probes, Eugene, OR) was added for tracking RBCs. A single colony of *E. coli* ER2738 was cultured in LB-Tet medium (LB medium 50mL + tetracycline (Tet) 50 μL) at 37°C in 24 hours. LB-Tet medium contains 10g/L NaCl (~171mM). Mixture of RBCs and *E. coli* ER2738 was prepared by mixing RBCs in 1xPBS and *E. coli* ER2738 in LB-Tet medium with 1:10 volume ratio (~168mM). Average zeta potentials of red blood cells and *E. coli* were −13.3 mV and −15.5 mV under the experimental conditions (measured by Zetasizer nano ZS, Malvern). Since PDMS and both microorganisms have the same polarity, they are electrostatically not favorable to bind together. Non-specific binding of *E. coli* cells to PDMS surfaces was not severe to interfere with the experiment, even after preconcentration step in this device.

A highly concentrated plug of fluorescent molecules often saturated the CCD array, which will lead to errors in quantification. The exposure time and contrast was controlled to map concentrated peak intensities between 10 nM and 100 nM fluorescein sodium salt and rGFP. Then, we measured the fluorescence intensities of the samples with known concentrations (0.03

pM, 0.3 pM 3 pM, 30 pM, 0.3 nM, 3 nM, 30 nM) and used them as internal references for calculating the concentration of fluorescein sodium salt and rGFP. Similarly, the fluorescence intensities of FITC-lectin with 0.5, 5, 50, 100, 500 μg/mL were measured and used as internal references. For evaluating the concentration of RBCs and *E. coli*, we used two methods. Firstly, the density of the cells of sample flow and filtered flow were measured by using disposable hemocytometer (SKC Inc, Covington, GA). The hemocytometer is a device designed for counting cells or particles. However, we could not use this device to measure the cell density of concentrated flow due to low output flow rate (In the case of Fig. 5.7, flow rate of concentrated flow was about 0.05 μL/min). Then, we were not able to obtain enough volume (~10 μL) to use the hemocytometer in short time period. Therefore, secondly, image analysis was done to measure the density of cells in the concentrated flow. With phase contrast images (Fig. 5.7 and Fig. 5.8), cells were distinguished from background by the difference of their brightness so that one can count the number of cells within defined volume by ImageJ program.

5.3. Continuous Preconcentration Demonstration

5.3.1. Negatively Charged Analyte

Fig. 5.2 shows representative result of the continuous-flow preconcentrator. The device has the width ratio w'= 50 and the length ratio l'= 0.7 (w_1= 20 μm, w_2= 980 μm, L_1= 6 mm, L_2= 9 mm). With this geometry, the concentration along the concentrated flow (blue line) would be enhanced by 50 fold in non-leaking operation (theoretical concentration factor given by Eq. 5.1-5.3 was 62). With the application of 80 V applied voltage and 5 μL/min flow rate, concentrated plug was generated on the front of slanted line-patterned Nafion, and concentrated sample flew along the concentrated channel successfully. Although fluorescence intensity of flow in the concentrated channel was the same with the sample flow (~300 A.U.) with no applied voltage, the intensity increased by 50 fold compared to the sample flow with 80 V applied voltage. In contrast, fluorescence intensity of the filtered flow in the main channel was dropped (~260 A.U.) right after Nafion (Fig. 5.2a-b). This fluorescence intensity level is below the noise level compared to background signal, which means the concentration of fluorescein sodium salt was very low, if any. As shown in the Fig. 5.2c, concentrated flow, filtered flow, and concentrated plug and the boundary of ion depletion zone were stably maintained across a 1mm wide channel. The device was operated for more than 30 min without compromising the ICP boundary.

We could observe the concentrated plug and measure its peak in the fluorescence intensity (Fig. 5.2b, from 50 to 150 pixels), indicating 200 fold concentration enhancement. While this value is lower than the concentration factor of previously reported batch-type preconcentrator[11], steady state concentrated flow of target molecules achieved in this system would be much more amenable to downstream sensor integration. Even though batch-type concentrator can achieve very high local concentration within the plug during the

preconcentration process, it is difficult to maintain such highly concentrated sample plug as soon as the preconcentration process is stopped or to deliver toward downstream integration, due to diffusive dispersion. This system does not suffer from this issue, and the concentration factor achieved could be maintained in the downstream channel or reservoir.

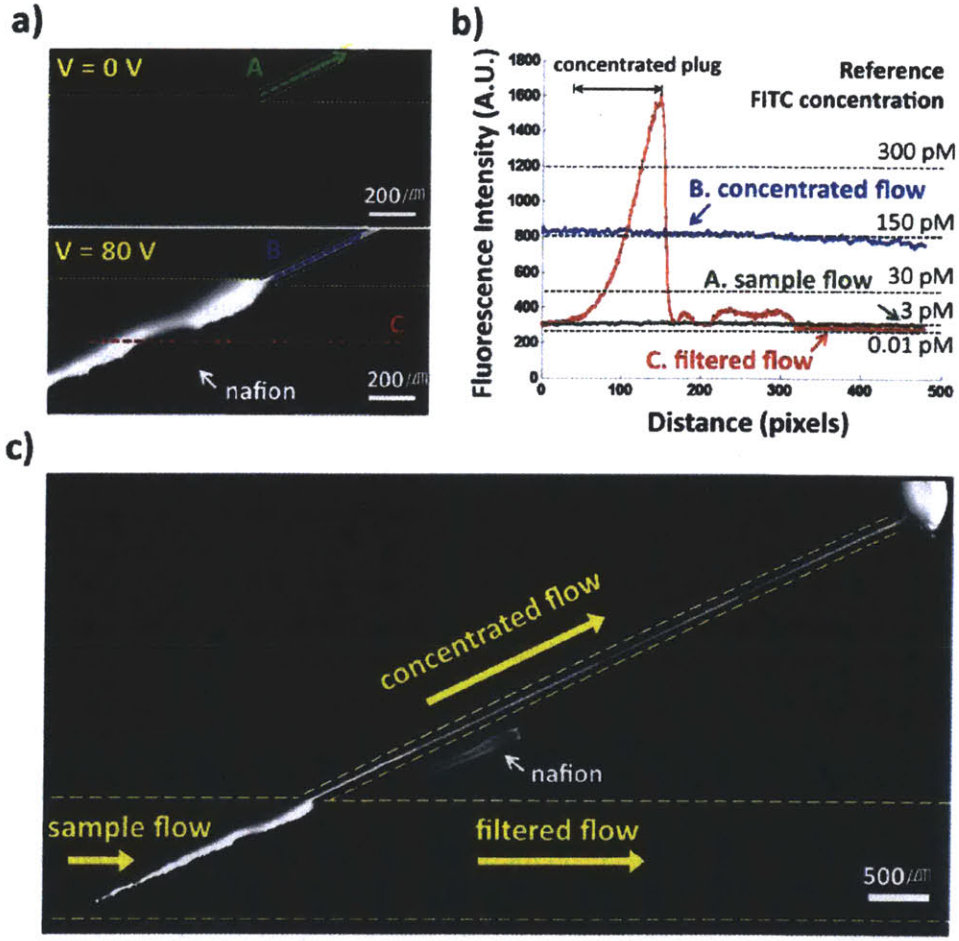

Figure 5.2 62 fold continuous-flow concentrator (w_1= 20 μm, w_2= 980 μm, L_1= 0.6 mm, L_2= 0.9 mm, and $r_{theoretical}$= 62) with the 30 degree inclined angle of Nafion junction. Flow rate and applied voltage were 5 μL/min and 80V, respectively. **a)** The comparison images of the concentrator when voltage was applied (lower) and when it was released (upper) and **b)** fluorescence intensity curve. Generation of concentrated flow (blue line (B)), concentrated plug (the peak of the red line (C)), filtered flow (decreased florescence intensity of red line (C) than inlet sample flow), and sample flow (green line (A)) are well defined. Fluorescence intensity of concentrated flow was jumped from 300 to 800 (corresponding 3 pM and 150 pM, respectively), which indicate 50 fold jumping of the concentration of fluorescein sodium salt. Wide peak from 200 to 300 pixels was due to the auto-fluorescence of the patterned Nafion. **c)** Integrated image of the concentrator from bifurcated point to the outlet of the channel. Yellow dotted lines indicate the geometry of the channel. 1mM dibasic phosphate buffer solution (pH 8.7) and 3 pM fluorescein sodium salt for tracking ions were used.

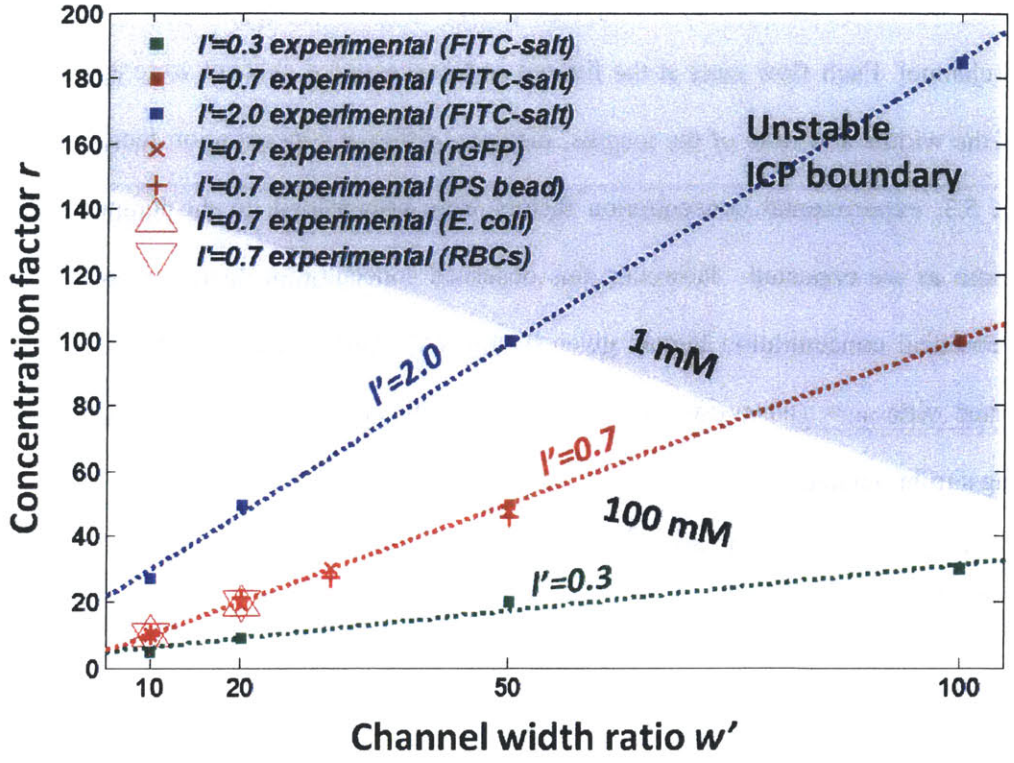

Figure 5.3 Fluorescein sodium salt, rGFP, RBCs, and *E. coli* test results with various width ratios $w' = (w_1 + w_2)/w_1$ ($w' = 10, 20, 50, 100$), and length ratios $l' = L_1/L_2$ ($l' = 0.3, 0.7, 2$) with the 30 degree inclined angle of concentrated channel and Nafion. Theoretical concentration factor was calculated by Eq. 5.3, and real concentration factor was measured by comparing fluorescence intensity of target samples. Flow rate was fixed as 2 μL/min and applied voltage was adjusted to generate the stable continuous concentrated flow between 0~150 V. The change of instability condition was also tested with 1mM, 10mM, 100mM dibasic phosphate buffer solutions for fluorescein sodium salt.

To characterize device performance and limitation, various continuous-flow concentrator (with different concentration factors) were fabricated and tested under different buffer ionic strength (1, 10, 100mM dibasic phosphate buffer solution) in comparison with theoretical concentration factors from Eq. 5.3 (Fig. 5.3). The basic conditions for experiments was 3 pM fluorescein sodium salt, the width of the concentrated channel $w_1 = 20$ μm, the height of the device $h = 15$ μm, and the sample flow rate 2 μL/min. Under these experimental parameters, the concentration factors for the device were designed with various width ratios $w' = (w_1+w_2)/w_1$ ($w' = 10, 20, 50, 100$), and length ratios $l' = L_1/L_2$ ($l' = 0.3, 0.7, 2$). At the main channel, overall

input flow rate was regulated by the syringe pump, which was divided into concentrated and filtered channel. Each flow rates at the filtered and concentrated channel were adjusted by their ratio of the widths and ratio of the lengths, inducing different concentration factor. As shown in the Fig. 5.3, experimental concentration factors were proportional to the length ratio and the width ratio as we expected. However, this observed concentration factors were always lower than theoretical concentration factors given by Eq. 5.3. rGFP, *E. coli* and RBCs concentration also tested with $w' = (w_1+w_2)/w_1$ ($w' = 10, 20, 30, 50$) and length ratios $l' = L_1/L_2$ ($l' = 0.7$), resulting similar tendency.

These differences could presumably be caused by two following reasons; **i)** the loss of charged species, which either leak thorough the ion depletion zone or non-specifically bind to the wall, **ii)** the change of flow rate ratio of filtered/concentrated channel by ICP. The former should be a minor factor, since the measured leakage rate of molecules and cells under microscopic observation were negligible in our experiment. Also, no significant non-specific binding on the wall and Nafion were observed (Fig. 5.2). Therefore, leakage and non-specific binding alone could not explain large discrepancies in the experiments using high width and length ratios (*e.g.* $l'=2$ and $w'=50$). Instead, additional hydrodynamic resistance by ICP may explain the large discrepancies. According to the experimental observation of polystyrene (PS) bead test and the previous experiment[19], the fluid velocity of concentrated flow was boosted adjacent to the ion depletion zone (Fig. 5.4). In addition, the fluid velocity of filtered flow was slightly reduced. This change of the fluid velocities was able to decrease flow rate ratio (from total flow rate divide by concentrated flow rate), resulting a drop in the concentration factor. The adjustment of fluid velocities of two channels is due to fast fluid vortices near IEMs[34, 41], which were routinely observed in this system. As described in Chapter 3, counter-rotating vortices pairs can

have asymmetric sizes (smaller vortex and larger vortex existed in series) with an external pressure field, while they have the same size of rotation with symmetric conditions (Fig. 3.2). In such case, the larger vortices would be dominant and can induce higher flow speed in the concentrated stream (Fig. 5.4). It is noted that the (apparent) loss of concentration factor in the experiment is not a real loss of target molecules. Rather, it is due to the underestimation of flow rate in the concentrated stream, caused by ignoring additional convection which is the essential part of electroconvection by ICP.

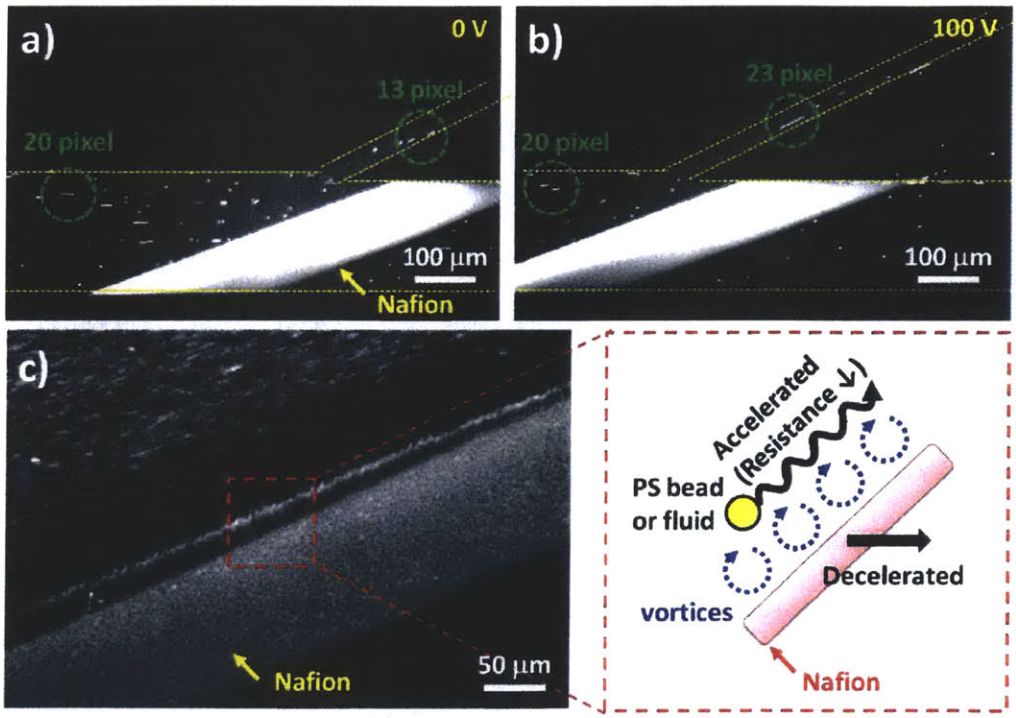

Figure 5.4 PS bead motion of 10 folds continuous concentrator with applied voltage of **a)** 0V and **b)** 100V. **c)** maginified snapshot near Nafion nanojunction with schematic PS bead and fluid motions. Fluid flow was visualized with 0.001% 1μm polystyrene (PS) bead (Invitrogen, Carlsbad, CA) (Fig. 5.4a-b) and 0.01% 0.25 μm PS bead (Duke scientific, Palo Alto, CA) (Fig. 5.4c) in 1mM dibasic phosphate buffer solution. Exposure time of fluorescence signal was 100 ms for single shot. 12 fold continuous-flow concentrator (w'=10, l'=0.7) was used. When electric field was applied for generating ICP, sample flow velocity was maintained as 200 μm/s (20 pixels/100ms, 20 pixels indicate 20 μm). However, concentrated flow velocity was jumped from 130 μm/s (Fig. 5.4a) to 230 μm/s (Fig. 5.4b). Based on this observation, the flow rate ratios of total flow to concentrated flow, *i.e.* concentration factor r, were dropped from 15 fold (20/13 × w') to 9 fold (20/23 × w'). Concentrated flow could be boosted because the thin layer of vortices group could enhance the fluid velocity on Nafion. With applied voltage (100 V) across Nafion, lots of small vortices were generated as shown in Fig. 5.4c, inducing wavy motion of PS bead and fluid as well near Nafion.

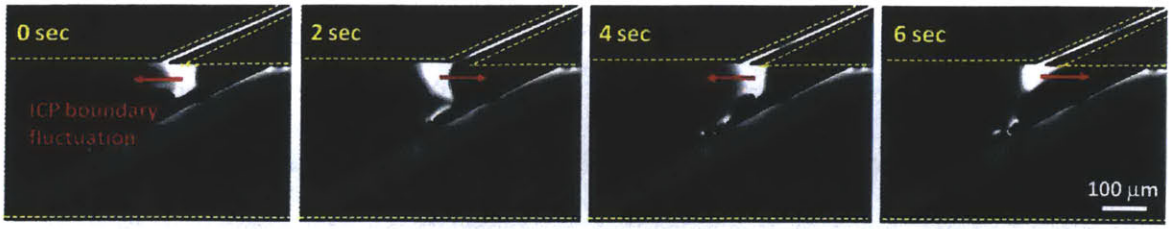

Figure 5.5 Destabilization of ICP boundary of the 125 fold continuous-flow concentrator (w'=100, l'=0.7). Total width of the main channel was 2 mm, flow rate was 2 μL/min. 1mM dibasic phosphate buffer was used. When we applied voltage 110 V, strong fluctuation of concentrated plug was occurred, mainly due to high concentration gradient at the interface between ICP zone and buffer fluid. In this case, the frequency of concentrated plug fluctuation is 0.25 Hz.

Critical limitation to achieve higher concentration factor in this system was the destabilization of the ICP boundary (Gray regime in Fig. 5.3). The magnitude of fluctuation increased with an electric field and a concentration gradient across the concentrated plug (Fig. 5.5). Small and steady fluctuation of ICP boundary was acceptable to the operation of this system because it did not disrupt the continuous concentration process. However, for higher concentration factor, the ICP boundary fluctuation worsened and the system could not maintain continuous concentrated flow anymore. The fluctuations tend to occur more frequently when ionic strength of buffer solution become higher. It is because higher electric field is needed for generating ICP boundary with high molar concentrations. As a result, instability regime expanded in higher ionic strength conditions, designated as the light gray regime in the Fig. 5.3.

5.3.2. Positively Charged Analyte

Next, continuous-flow concentrations of target samples with different polarities were tested. Fluorescein isothiocyanate (FITC) conjugated lectin from Lens culinaris (lentil) (FITC-lectin) was used. FITC-lectin (pI~8.0–8.8) has negatively charged surface under pH 8.5 and positively charged surface under pH 7.4. Fig. 5.6 shows FITC-lectin concentration test results with 3 different concentration factors; 12 fold (w'= 10, l'= 0.7, w_1=20 μm), 46 fold (w'= 20, l'= 0.7,

w_1=10 μm) and 130 fold (w'= 50, l'= 0.7, w_1=10 μm). Other conditions were fixed as 15 μm height, 1 μL/min sample flow rate and 1mM phosphate buffer. Applied voltage was adjusted from 0 to 150 V. Concentrated flow velocity v_c was newly defined as the theoretically expected fluid velocity of concentrated flow under the intention for showing the effect of non-specific binding (slow velocity gives higher chance to occur non-specific binding). It was calculated by following equations.

$$v_c = \frac{Q_1}{w_1 \cdot h_1} = \frac{Q_1 + Q_2}{r_{\text{theoretical}} \cdot w_1 \cdot h_1}. \tag{5.4}$$

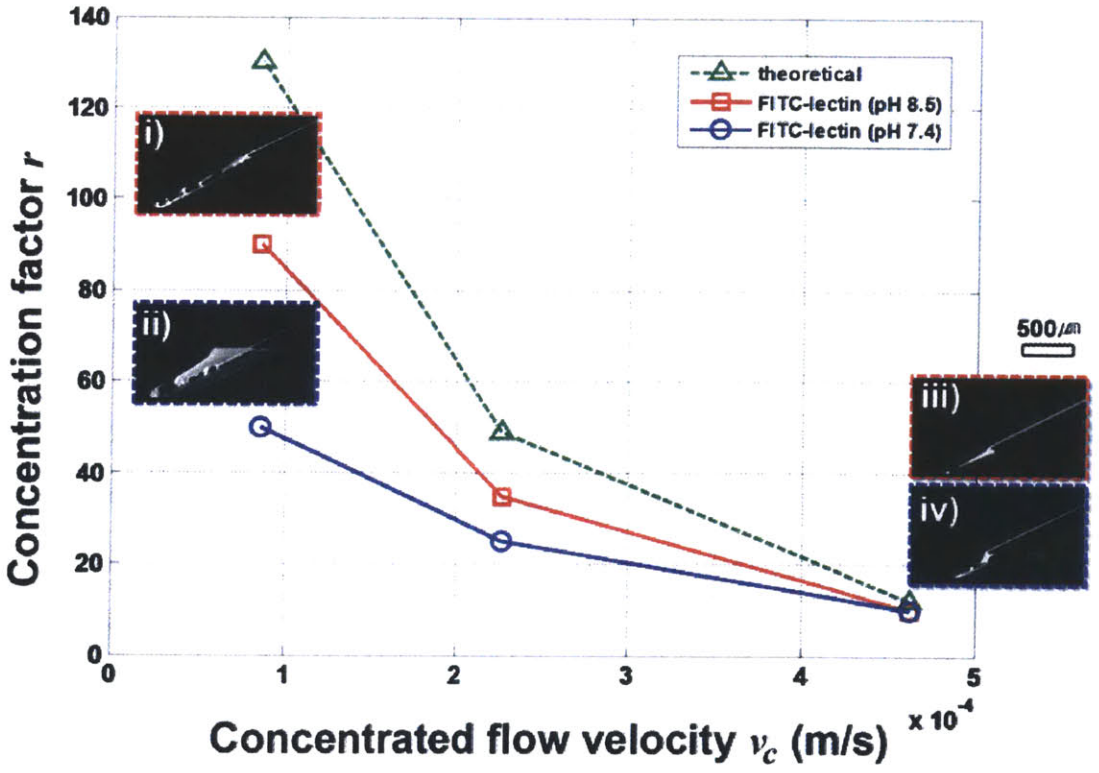

Figure 5.6 FITC-lectin concentration test results with 3 different theoretical concentration factors/concentrated flow velocities; 12 fold (w'= 10, l'= 0.7, w_1=20 μm), 46 fold (w'= 20, l'= 0.7, w_1=10 μm), 130 fold (w'= 50, l'= 0.7, w_1=10 μm). Inset images show fluorescence image of the operation of the concentrator with **i)** 130 fold at pH 8.5, **ii)** 130 fold at pH 7.4, **iii)** 12 fold at pH 8.5, **iv)** 12 fold at pH 7.4. Scale bar indicate 500 μm for all inset images. Loss of the concentration factor was larger when designed concentration factor became higher due to the underestimation of concentrated flow rate by electroconvection. In addition, additional loss of concentration factor in positively charged FITC-lectin (pH 7.4) compared to negatively charged FITC-lectin (pH 8.5) also became larger when reduced concentrated flow velocity due to non-specific, electrostatic binding.

As shown in the Fig. 5.6, experimental concentration factors for FITC-lectin were also always lower than theoretical concentration factor due to additional fluidic resistance by ICP. In addition, the measured concentration factors of positively charged FITC-lectin (pH 7.4) were lower than that of negatively charged FITC-lectin (pH 8.5). This additional drop of the concentration factor was due to non-specific electrostatic binding to the wall and Nafion. While 0.1 % BSA was added to prevent non-specific binding, the electrostatic binding would be significant at low flow rate because positively charge FITC-lectin had more chance to detect, and stuck to negatively charged wall and Nafion. Consequently, there was obvious no significant drop with relatively fast flow (12 fold case), but large discrepancies were presented at slow flow (130 fold case) (Fig. 5.6).

5.3.3. Cells

For the demonstration of cell concentration, human red blood cells (RBCs) was tested with 20 fold concentrator (w'=10, l'= 1.2) with high flow rate (5 μL/min) and 1x PBS (~150 mM) solution with 0.2% Pluronic® F108 (Fig. 5.7). Comparison images of two outlets show the contrast of the densities of RBCs between the outlet of the concentrated flow (Fig. 5.7b) and the outlet of the filtered flow (Fig. 5.7c) obviously. The density of RBCs was jumped from 1.9×10^6 cells/ml in the sample flow to 3.7×10^7 cells/ml in the concentrated flow, indicating 19 fold increments. This value was almost the same with theoretical concentration factor, 20 fold. Representing motions of blood cells were blocked and collected in the concentrated plug near Nafion, climbed Nafion to the bifurcated point, and flew through the concentrated channel.

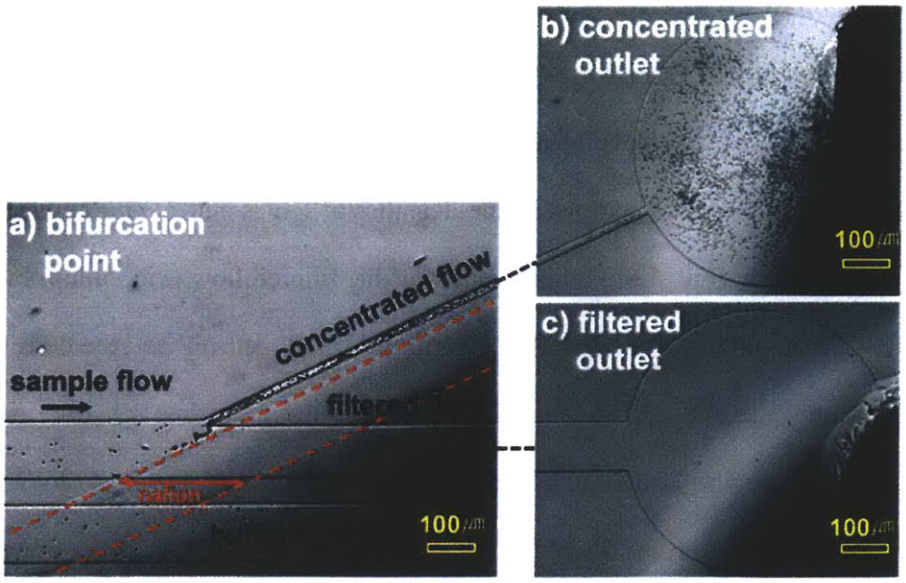

Figure 5.7 20 fold continuous-flow concentrator for RBCs (w'=10, l'= 1.2). **a)** The operating images of the concentrator with voltage (90 V) and flow rate (5 μL/min). Comparison images of **b)** the outlet of concentrated flow and **c)** the outlet of filtered flow. The density of RBCs increased from 1.9×10^6 cells/ml to 3.7×10^7 cells/ml, indicating 19 fold. Red dotted line indicated the patterned Nafion.

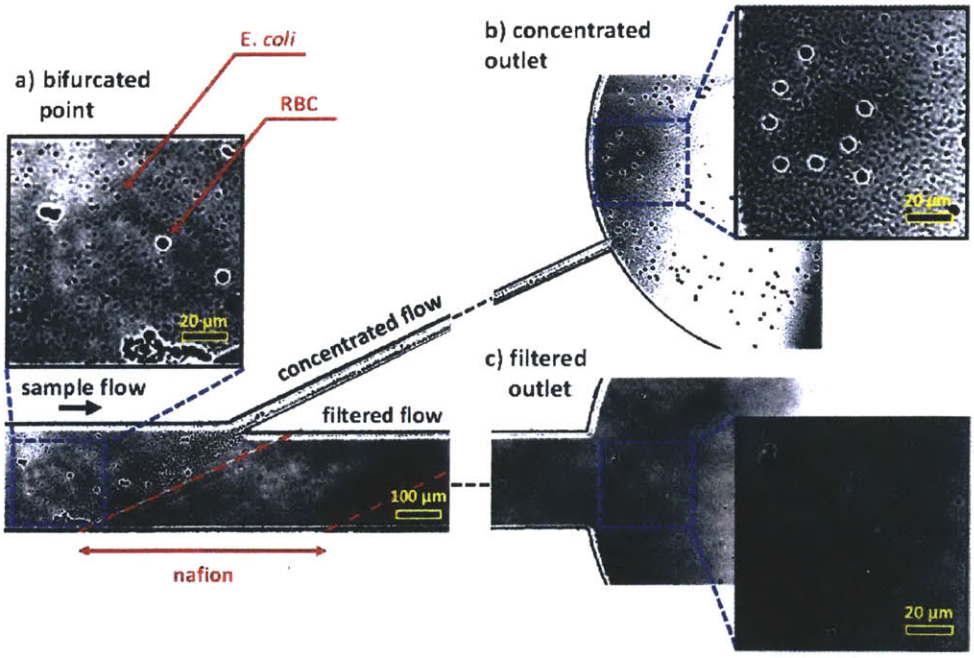

Figure 5.8: 20 fold continuous-flow concentrator for RBCs and *E. coli* (w'=10, l'= 1.2). **a)** The operating images of the concentrator with voltage (14 V) and flow rate (0.1μL/min) and magnified image of the sample flow. Comparison images and magnified images of **b)** the outlet of concentrated flow and **c)** the outlet of filtered flow. The density of RBCs increased from 7.3×10^5 cells/ml to 1.4×10^7 cells/ml and the density of *E. coli* jumped from 3.2×10^7 cells/ml to 6.5×10^8 cells/ml, indicating 19 fold and 20 fold, respectively. Red dotted line indicates the patterned Nafion.

Concentration of the mixture of various biomolecules (RBCs and *E. coli*) also tested with the mixed buffer solution of 1x PBS and LB-Tet medium (171mM). The continuous concentrated flow of RBCs and *E. coli* was developed successfully as shown in Fig. 5.8. In the Comparison images of two outlets show the contrast of the densities of RBCs and *E. coli* between the outlet of the concentrated flow (Fig. 5.8b) and the outlet of the filtered flow (Fig. 5.8c) obviously. The density of RBCs was jumped from 7.3×10^5 cells/ml to 1.4×10^7 cells/ml and the density of *E. coli* was jumped from 3.2×10^7 cells/ml to 6.5×10^8 cells/ml, indicating 19 fold and 20 fold respectively. This value was also almost the same with concentration factor, 20 fold. With above two tests, leakage rate to the filtered flow was also calculated by live imaging of the concentration operation, resulting 0 % during 120 sec operation.

In addition, RBCs / *E. coli* concentration tests were performed with 12 and 24 fold concentrator (w'=10, 20 and l'= 0.7) (Fig. 5.3). The concentration factors for RBCs and *E. coli* were almost the same as the factors for fluorescein sodium salt and rGFP. That is, when the geometry of the device is fixed, we can obtain the same concentration factor for any targets. It is because the concentration factor is only governed by flow rate ratio of concentrated channel and filtered channel. Such a uniform concentration over many different targets would be a useful feature as a generic preconcentration interface.

5.4. Outlook and Future Works

Our next target is developing ultra-high-throughput preconcentrator, especially for water monitoring application. While preconcentration/enrichment process is valuable in analytical chemistry to detect low abundance targets, detection of detrimental toxins and bacteria in recreational and drinkable waters is still challenging and without satisfactory solutions. The preconcentration requirement for waterborne bacterial sensing is quite daunting , *i.e.* less than 1 cells in 1 mL of sample water [42]. There are various methods to concentrate targets, ranging from centrifugation(in laboratory scale) to electrokinetic trapping (in microscale), but these methods have critical limitations. In the case of current, laboratory scale preconcentrators (*e.g.* centrifugation and evaporation), they need relatively long operation time (few hours to days), and samples are often lost. In contrast, preconcentration process built in microfluidic systems (*e.g.* electrokinetic trapping and isotachophoresis) are faster, yet has impractically low sample volume throughput (pL~μL per 1 hour). The preconcentration technology described here can potentially process large volume of original sample volume (1mL~1L), preconcentrating targets in a reasonable timeframe (~1 hour) into a small volume for high-sensitivity biochemical and molecular assays.

References

[1] T. E. Bradley, W. W. Arthur, W. S. Robert, and G. Farshid, J. Cell. Physiol. **209**, 987 (2006).

[2] A. J. Engler, S. Sen, H. L. Sweeney, and D. E. Discher, Cell **126**, 677 (2006).

[3] B. Jung, R. Bharadwaj, and J. G. Santiago, Anal. Chem. **78**, 2319 (2006).

[4] D. Janasek, M. Schilling, J. Franzke, and A. Manz, Anal. Chem. **78**, 3815 (2006).

[5] P. Gebauer, and P. Bocek, Electrophoresis **23**, 3858 (2002).

[6] A. K. Singh, D. J. Throckmorton, B. J. Kirby, and A. P. Thompson, in *Micro Total Analysis Systems* (Kluwer Academic, Nara, Japan, 2002), pp. 347.

[7] R. S. Foote, J. Khandurina, S. C. Jacobson, and J. M. Ramsey, Anal. Chem. **77**, 57 (2005).

[8] S. Song, A. K. Singh, and B. J. Kirby, Anal. Chem. **76**, 4589 (2004).

[9] J. Khandurina, S. C. Jacobson, L. C. Waters, R. S. Foote, and J. M. Ramsey, Anal. Chem. **71**, 1815 (1999).

[10] K. Sueyoshi, F. Kitagawa, and K. Otsuka, J Sep Sci **31**, 2650 (2008).

[11] Y. C. Wang, A. L. Stevens, and J. Y. Han, Anal. Chem. **77**, 4293 (2005).

[12] A. M. Skelley, O. Kirak, H. Suh, R. Jaenisch, and J. Voldman, Nat Meth **6**, 147 (2009).

[13] S. J. Kim, Y. A. Song, and J. Han, Chem Soc Rev **39**, 912 (2010).

[14] Y. C. Wang, and J. Y. Han, Lab Chip **8**, 392 (2008).

[15] J. H. Lee, B. D. Cosgrove, D. A. Lauffenburger, and J. Han, J Am Chem Soc **131**, 10340 (2009).

[16] L. F. Cheow, S. H. Ko, S. J. Kim, K. H. Kang, and J. Han, Anal. Chem. **82**, 3383 (2010).

[17] C.-H. Chen, A. Sarkar, Y.-A. Song, M. A. Miller, S. J. Kim, L. G. Griffith, D. A. Lauffenburger, and J. Han, J Am Chem Soc **133**, 10368 (2011).

[18] S. H. Ko, S. J. Kim, L. F. Cheow, L. D. Li, K. H. Kang, and J. Han, Lab Chip **11**, 1351 (2011).

[19] S. J. Kim, L. D. Li, and J. Han, Langmuir **25**, 7759 (2009).

[20] H. W. Hou, A. A. S. Bhagat, A. G. L. Chong, P. Mao, K. S. W. Tan, J. Y. Han, and C. T. Lim, Lab Chip **10**, 2605 (2010).

[21] A. A. S. Bhagat, H. W. Hou, L. D. Li, C. T. Lim, and J. Y. Han, Lab Chip **11**, 1870 (2011).

[22] C.-F. Chou, R. H. Austin, O. Bakajin, J. O. Tegenfeldt, J. A. Castelino, S. S. Chan, E. C. Cox, H. G. Craighead, N. Darnton, T. A. J. Duke, J. Han, and S. Turner, Electrophoresis **21**, 81 (2000).

[23] J. Han, J. Fu, and R. B. Schoch, Lab Chip **8**, 23 (2008).

[24] Y. Zeng, and D. J. Harrison, Anal. Chem. **79**, 2289 (2007).

[25] J. Fu, R. R. Schoch, A. L. Stevens, S. R. Tannenbaum, and J. Han, Nat. Nanotech. **2** 121 (2006).

[26] E. K. Dimitriadis, F. Horkay, J. Maresca, B. Kachar, and R. S. Chadwick, Biophys. J. **82**, 2798 (2002).

[27] F. C. Leinweber, J. C. T. Eijkel, J. G. Bower, and A. van den Berg, Anal Chem **78**, 1425 (2006).

[28] Y. Xiao, X.-D. Yu, J.-J. Xu, and H.-Y. Chen, Electrophoresis **28**, 3302 (2007).

[29] V. Liu, Y. A. Song, and J. Han, Lab Chip **10**, 1485 (2010).

[30] J. H. Lee, and J. Han, Microfluidics and Nanofluidics **9**, 973 (2010).

[31] J. H. Lee, Y.-A. Song, S. R. Tannenbaum, and J. Han, Anal. Chem. **80** 3198 (2008).
[32] S. J. Kim, S. H. Ko, K. H. Kang, and J. Han, Nature Nanotechnology **5**, 297 (2010).
[33] L. T. Gao, and C. J. Seliskar, Chem Mater **10**, 2481 (1998).
[34] S. J. Kim, Y.-C. Wang, J. H. Lee, H. Jang, and J. Han, Phys. Rev. Lett. **99**, 044501 (2007).
[35] T. A. Zangle, A. Mani, and J. G. Santiago, Anal Chem **82**, 3114 (2010).
[36] B. DJ, M. GA, and W. GM, Annual Review of Biomedical Engineering **4**, 261 (2002).
[37] J. C. Giddings, and M. R. Schure, Chem Eng Sci **42**, 1471 (1987).
[38] J. H. Lee, Y. A. Song, and J. Y. Han, Lab Chip **8**, 596 (2008).
[39] D. C. Duffy, J. C. McDonald, O. J. A. Schueller, and G. M. Whitesides, Anal. Chem. **70**, 4974 (1998).
[40] J. H. Lee, S. Chung, S. J. Kim, and J. Y. Han, Anal. Chem. **79**, 6868 (2007).
[41] S. M. Rubinstein, G. Manukyan, A. Staicu, I. Rubinstein, B. Zaltzman, R. G. Lammertink, F. Mugele, and M. Wessling, Phys. Rev. Lett. **101**, 236101 (2008).
[42] R. T. Noble, and S. B. Weisberg, Journal of Water and Health **03**, 381 (2005).

Chapter 6

Conclusion

Ion concentration polarization (ICP) is a ubiquitous phenomenon in electrochemistry and membrane science. Conventionally, research interests were focused at analyzing the effects of concentration overpotential induced by ICP and reducing this undesirable additional resistance in electrochemical devices. Recent studies on ICP, however, have been expanded into diverse topics such as its nonlinearity (*i.e.* overlimiting conductance(OLC)), as well as ICP in nanofluidic systems. While nonlinear ICP and its application becomes one of the most intriguing issues in the field of physicochemical hydrodynamics, the lack of quantitative understanding on nonlinear ICP restricts the ongoing and future engineering of new and existing electrochemical systems that are affected by this intriguing and complicated phenomenon. To overcome this barrier, we explore the fundamentals of ICP by microscopic visualization, and investigate the potential use of new ICP-driven devices for electrochemical desalination, and microfluidic preconcentrator.

In Chapter 2, we demonstrate the microscale electrodialysis (ED) system and visualize fluid flows and salt concentration profiles directly by utilizing microfludic experimental materials and methods. PDMS's transparency, its microscale channel, and R6G fluorescence dyes allow us to observe what happens inside an ED system in real-time. Depending on the operating current regimes, Ohmic, limiting, and overlimiting, dynamics of ED (fluid dynamics, ion transport, and salt concentration profiles) are significantly affected. In the Ohmic regime, linear diffusion induces the linear diffusion boundary layer and stable fluid flows. In the limiting and overlimiting regime, stable and unstable vortices and depletion zone appear from ion exchange membranes (IEM) by electroconvection. The size of the vortices and the thickness of the boundary layer and depletion zone increase at high voltage (or current), whereas the linear-

concentration diffusion layer (outside of the depletion zone) shrinks. It is noticed that the vortex structure under non-zero fluid flow is visualized in this paper for the first time. Lastly, we observe that the optimized operating condition is located above the Ohmic regime.

In Chapter 3, our experiments in the micro ED platform and modeling results reveal significant insights regarding the physics of ICP. Contrary to recent hypothesis [1], it firmly establishes that electroconvective vortices do occur in realistic systems, largely determining the boundary layer and ion transport efficiency. The flow and concentration patterns observed in this work are not compatible with any other proposed mechanisms of OLC [1-3] except electroconvection [4]. We validate this by re-producing the observed experimental behaviors with *ab initio*, multiscale numerical modeling of the system. In addition, we reveal the new scaling law that governs the thickness of electroconvective vortex under shear flow. This new relation is a clear departure from the previous characterization [5-8], and therefore has significant implications in optimizing many electrochemical systems.

In Chapter 4, we demonstrate a robust, scalable desalination / purification platform utilizing ICP. In a different device architecture from our earlier work[9], ICP is initiated between two juxtaposed identical IEMs by relocation of non-conducting co-ions (cation between two AEMs or anions between two CEMs). There are two critical advances from the previous microfluidic ICP desalination devices[9-11]. First, the two IEMs are shielding the possible byproducts of Faradic electrode reactions, which could be toxic. As a result, we can remove most salt ion (>97%) and particles in model brackish water (10mM NaCl) steadily and stably. Secondly, the ED-like parallel and reciprocal platform allows us to stack the unit device, realizing scaled-up system with realistic water processing rates. It is noted that we can treat 20 μL/min sample waters with very small channel area (0.4 mm^2), so the scale-up ICP platform will

have a smaller size than other desalination platforms.

In addition, we show that ICP platform is more efficient than ED by quantifying desalting performances of both ICP and ED platforms, especially in overlimiting regime (>2V). We evaluate the performance of this new ICP desalination method from various quantitative metrics, such as salt removal ratio, energy consumption, energy per ion removal, current efficiency, and area efficiency over a wide range of applied current (5-200μA). ICP system with two CEMs (2CEM) shows better salt removal ratio, energy per ion removal, current efficiency, and area efficiency than that of ED. Although the ICP system with two AEMs (2AEM) has worse salt removal ratio and current efficiency, it shows much better energy consumption and energy per ion removal than ED system. By testing various electrolytes(10mM KCl, NaCl, and LiCl), we found that these tendencies become more significant as we use slower cation, probably because of the co-location of cation and anion enabled by strong electric field in overlimiting regime; the faster ion drags the slower ion toward the direction of the faster ion movement.

In Chapter 5, we have demonstrated the continuous-flow concentrator based on the ion concentration polarization (ICP) phenomenon, allowing one to process bio-samples at reasonable sample flow rate (~a few μL/min) successfully. Various geometries of the device, the width ratio w' and the length ratio l', were tested to control the concentration factor from 1 to 200 with diverse samples under different molar concentrations and pH (opposite surface charge polarities) of the buffer solutions. As the first continuous-flow concentration system, applied to both biomolecules and cells manner, this work is a meaningful contribution even if the maximum concentration factor is lower than that of previously reported preconcentrator (~10^6 fold) [12-16]. This system's concentration factor was uniform for various targets, including dye, protein (positively and negatively charged species), deformable cells (RBCs), and bacteria. This is

because of the use of the new ICP scheme, which can 'filter out' any charged species regardless of their sizes. Previously reported systems suffered from batch-type process (low throughput), and thus the system parameters (concentration and electric field, *etc.*) kept changing as a function of time and the concentrated sample volume was limited to pL~nL scale. In contrast, the continuous-flow preconcentrator can inherently eliminate above unfavorable characteristics by isolating concentrated streams. Therefore, continuous-flow preconcentration device described here would be much more flexible for integration with various types of downstream devices, such as a continuous-flow separator, mass spectrometry of target samples. The quantity of the concentrated sample volume is also controllable from few pL to μL. Instead of specific demonstration of the preconcentration of rare samples (*e.g.* circulating tumor cells), we showed general applicability of our system by testing the preconcentration of samples with different polarities (positively/negatively charged species) and various sizes from dyes and proteins to cells. Combination of this wide range of working conditions, high sample throughput, and integration flexibility into other microfluidic devices would make this system useful as a front-end concentration interface for many biosensors and detection systems.

References

[1] M. B. Andersen, M. van Soestbergen, A. Mani, H. Bruus, P. M. Biesheuvel, and M. Z. Bazant, Phys Rev Lett **109**, 108301 (2012).

[2] V. V. Nikonenko, N. D. Pismenskaya, E. I. Belova, P. Sistat, P. Huguet, G. Pourcelly, and C. Larchet, Adv Colloid Interfac **160**, 101 (2010).

[3] E. V. Dydek, B. Zaltzman, I. Rubinstein, D. S. Deng, A. Mani, and M. Z. Bazant, Phys Rev Lett **107**, 118301 (2011).

[4] I. Rubinstein, and B. Zaltzman, Phys Rev E **62**, 2238 (2000).

[5] R. F. Probstein, *Physicochemical Hydrodynamics: An Introduction* (Wiley-Interscience, New York, 2003), 2 edn.

[6] S. J. Kim, Y. C. Wang, J. H. Lee, H. Jang, and J. Han, Phys Rev Lett **99**, 044501 (2007).

[7] S. M. Rubinstein, G. Manukyan, A. Staicu, I. Rubinstein, B. Zaltzman, R. G. H. Lammertink, F. Mugele, and M. Wessling, Phys Rev Lett **101**, 236101 (2008).

[8] G. Yossifon, and H. C. Chang, Phys Rev Lett **101**, 254501 (2008).

[9] S. J. Kim, S. H. Ko, K. H. Kang, and J. Han, Nat Nanotechnol **5**, 297 (2010).

[10] Kyle N. Knust, Dzmitry Hlushkou, Robbyn K. Anand, Ulrich Tallarek, and R. M. Crooks, Angew Chem-Ger Edit (DOI: 10.1002/anie.201302577).

[11] A. Mani, and M. Bazant, Phys Rev E **84**, (2011).

[12] Y. C. Wang, A. L. Stevens, and J. Y. Han, Anal. Chem. **77**, 4293 (2005).

[13] J. H. Lee, B. D. Cosgrove, D. A. Lauffenburger, and J. Han, J Am Chem Soc **131**, 10340 (2009).

[14] L. F. Cheow, S. H. Ko, S. J. Kim, K. H. Kang, and J. Han, Anal. Chem. **82**, 3383 (2010).

[15] S. J. Kim, Y. A. Song, and J. Han, Chem Soc Rev **39**, 912 (2010).

[16] S. H. Ko, S. J. Kim, L. F. Cheow, L. D. Li, K. H. Kang, and J. Han, Lab Chip **11**, 1351 (2011).